UNIVERSITY OF THESSALY

DEPARTMENT OF MECHANICAL ENGINEERING

LABORATORY OF MECHANICS AND STRENGTH OF MATERIALS

Post-Graduate Diploma

Application of the Armstrong - Frederick Cyclic Plasticity Model for Simulating Structural Steel Member Behavior

George E. Varelis

Diploma in Civil Engineering, University of Thessaly, 2007

Advisor: Spyros A. Karamanos

Submitted to the Department of Mechanical Engineering

in Partial Fulfillment of the Requirements

for the Degree of Post-Graduate Diploma

University of Thessaly, March 2010

Η έγκριση της μεταπτυχιακής εργασίας από το Τμήμα Μηχανολόγων Μηχανικών Βιομηχανίας της Πολυτεχνικής Σχολής του Πανεπιστημίου Θεσσαλίας δεν υποδηλώνει αποδοχή των απόψεων του συγγραφέα (Ν. 5343/32 αρ. 202 παρ. 2).

Εγκρίθηκε από τα Μέλη της Τριμελούς Εξεταστικής Επιτροπής:

Πρώτος Εξεταστής (Επιβλέπων) — Δρ. Σπύρος Α. Καραμάνος
Αναπληρωτής Καθηγητής, Τμήμα Μηχανολόγων Μηχανικών, Πανεπιστήμιο Θεσσαλίας

Δεύτερος Εξεταστής — Δρ. Αντώνιος Γιαννακόπουλος
Καθηγητής, Τμήμα Πολιτικών Μηχανικών, Πανεπιστήμιο Θεσσαλίας

Τρίτος Εξεταστής — Δρ. Αλέξιος Κερμανίδης
Λέκτορας, Τμήμα Μηχανολόγων Μηχανικών, Πανεπιστήμιο Θεσσαλίας

Ευχαριστίες

Θα ήθελα καταρχήν να ευχαριστήσω τον επιβλέποντα καθηγητή μου κύριο Σπύρο Καραμάνο για τη συνεργασία που είχαμε κατά τη διάρκεια των τελευταίων ετών. Η βοήθεια και η καθοδήγηση του ήταν καταλυτική για την ολοκλήρωση της παρούσας εργασίας. Αισθάνομαι επίσης την υποχρέωση να ευχαριστήσω τους συνεπιβλέποντες καθηγητές κύριο Αντώνη Γιαννακόπουλο και κύριο Αλέξη Κερμανίδη για τα εύστοχα σχόλια και παρατηρήσεις τους που με βοήθησαν να βελτιώσω τη σύνθεση και τη δομή της εργασίας μου.

Θέλω επίσης να ευχαριστήσω τους συμφοιτητές και φίλους Δανιήλ, Πατρικία, Σωτηρία και Αγλαΐα για την συνεργασία που είχαμε και για όλες τις φορές που με βοήθησαν να ξεπεράσω τα όποια προβλήματα προέκυπταν. Στη Χριστίνα οφείλω ένα μεγάλο ευχαριστώ για την υποστήριξη και τη βοήθεια που μου παρείχε καθόλη τη διάρκεια της εκπόνησης της εργασίας.

Τέλος, θα ήθελα να ευχαριστήσω όλα τα μέλη της οικογένειας μου που με στηρίζουν και μοιράζονται τα όνειρα μου. Η εργασία μου είναι αφιερωμένη σε αυτούς.

Βαρέλης Ε. Γιώργος

Application of the Armstrong - Frederick Cyclic Plasticity Model for Simulating Structural Steel Member Behavior

George E. Varelis

University of Thessaly, Department of Mechanical Engineering, 2010

Advisor: Spyros A. Karamanos

Abstract

The current study examines the Armstrong – Frederick cyclic plasticity model and evaluates its performance on simulating structural steel member behavior. The formulation of the constitutive equations and their numerical implementation in an in-house finite element code are discussed in detail. The performance of the model on the prediction of the cyclic plasticity related phenomena such as the Bauschinger effect and the accumulation of plastic strain is evaluated through appropriately selected examples. The behavior of a pipe subjected to cyclic bending and cyclic bending in the presence of constant internal/external pressure is examined with the use of finite element models adopting the Armstrong – Frederick model. Finally, the UOE manufacturing process and the effect it has on the maximum collapse pressure of the produced pipe is simulated accurately. The predictions of the isotropic hardening model, the linear kinematic hardening model and the Armstrong – Frederick model are compared with the corresponding predictions of more elaborate model developed and implemented elsewhere adopting the “Bounding Surface” concept.

Εφαρμογή του Μοντέλου Κυκλικής Πλαστικότητας Armstrong – Frederick για την Προσομοίωση της Συμπεριφοράς Μεταλλικών Δομικών Στοιχείων

Γιώργος Ε. Βαρέλης

Πανεπιστήμιο Θεσσαλίας, Τμήμα Μηχανολόγων Μηχανικών, 2010

Επιβλέπων: Σπύρος Α. Καραμάνος

Περίληψη

Η παρούσα εργασία πραγματεύεται το μοντέλο κυκλικής πλαστικότητας Armstrong – Frederick και εξετάζει τη δυνατότητα του να προσομοιώνει τη συμπεριφορά δομικών στοιχείων από χάλυβα. Η διατύπωση των καταστατικών εξισώσεων του μοντέλου και η αριθμητική τους εισαγωγή σε κώδικα πεπερασμένων στοιχείων παρουσιάζεται λεπτομερώς. Η απόδοση του μοντέλου στην προσομοίωση φαινομένων που σχετίζονται με θέματα κυκλικής πλαστικότητας όπως το φαινόμενο Bauschinger και η συσσώρευση πλαστικών παραμορφώσεων εξετάζεται μέσα από κατάλληλα επιλεγμένα παραδείγματα. Η συμπεριφορά σωληνωτών στοιχείων που υπόκεινται σε κυκλική κάμψη και κυκλική κάμψη με την παρουσία εσωτερικής/εξωτερικής πίεσης εξετάζεται με τη χρήση μοντέλων πεπερασμένων στοιχείων που υιοθετούν το μοντέλο Armstrong – Frederick. Τέλος, η διαδικασία μορφοποίησης αγωγών UOE και η επίδραση που έχει στην μέγιστη πίεση που οδηγεί σε κατάρρευση του αγωγού προσομοιώνονται με ακρίβεια. Οι προβλέψεις του μοντέλου ισοτροπικής κράτυνσης, του μοντέλου γραμμικής κινηματικής κράτυνσης και του μοντέλου Armstrong – Frederick συγκρίνονται με τις αντίστοιχες προβλέψεις μίας πρόσφατης εργασίας που χρησιμοποιεί ένα πιο εξελιγμένο μοντέλο που βασισμένο στην ιδέα της «Οριακής Επιφάνειας».

Contents

1. Introduction to cyclic plasticity

Metal cyclic plasticity is a particular area in the general field of constitutive equations which studies metal material behavior in the plastic range under cyclic (repeated) loading conditions. Several interesting phenomena related to plasticity take place under alternating loading in the plastic regime and their understanding is of crucial importance for the safe and economic design of metal structures. Before the presentation of the cyclic plasticity effects in engineering problems, it is necessary to discuss briefly metal material behavior under cyclic loading.

The behavior of metals when subjected to loading cycles exceeding the elastic range can vary significantly depending on the micro structural characteristics of the material. Experimental studies have shown that yield surfaces, defining the limit of the elastic regime, translate, change size and possibly change shape during plastic loading. Each stress state is history dependent; this implies that the stress path followed until the current state is needed for the accurate prediction of any subsequent change in the stress state. Several phenomena are strictly related to the plastic behavior of the material under cyclic loading. The most important ones are briefly discussed below:

1) The most well-known cyclic loading related phenomenon is the Bauschinger effect [Bauschinger (1881), Armstrong & Frederick (1966), Kyriakides and Corona (2007)]. This effect occurs when a metal is loaded past its elastic limit followed by loading in the opposite direction. During reverse loading, plastic deformation will begin at a significantly lower stress level. Furthermore, the hardening modulus changes gradually as the amount of plastic strain increases.
2) Cyclic hardening/softening may also take place under symmetric strain loading. In general, initially soft or annealed metals tend to harden toward a stable limit, and initially hard metals tend to soften [Hassan & Kyriakides 91992)].
3) When a metal is subjected to unsymmetrical stress-controlled cycles, this causes progressive “creep” in the direction of the mean stress, a phenomenon often reported as “ratcheting” [Bari & Hassan (2000)]. As loading is repeated, each consecutive hysteresis loop translates in this direction in a varying rate due to the fact that the cycles do not have complete closure of each loop. This phenomenon will be extensively discussed in Chapter 3 of the present study.

1.1 Engineering problems with cyclic plasticity

Many engineering applications from the structural and mechanical engineering field involve cyclic loading well beyond the elastic regime. Even structures that are designed to perform elastically, cyclic plastic actions often occur due to discontinuities or cracks. This necessitates the prediction of metal cyclic

behavior in the inelastic range through simple and robust cyclic plasticity models. Some well known engineering problems where cyclic plasticity is involved will be briefly discussed in the following paragraphs.

Fatigue is the most well known engineering problem related to engineering failures. Many famous failures have been attributed to this phenomenon over the years. Depending on the number of cycles, fatigue is categorized into High or Low cycle fatigue. For loading cycles up to about 10^4, the problem is in the range of Low cycle fatigue, while for loading cycles exceeding this nominal limit, the problem is referred to as High cycle fatigue problem. Both problems involve plastic loading of the material even if the applied load cycles are in the elastic range. High cycle fatigue is usually connected with varying loads significantly lower from the elastic limit. Nevertheless, due to material defects, discontinuities or cracks the material is plasticized locally. The local cyclic loading induces material deterioration which causes crack propagation until failure. On the contrary, Low cycle fatigue is associated with a small number of cycles of intense loading and repeated excursions in the inelastic range. The maximum number of cycles that a structure can sustain is related directly to the ability of the material to sustain its mechanical characteristics under this strong cyclic loading.

In the mechanical engineering field, simulation of metal forming is an aspect that gained a lot of attention in the last years with significant application in the aerospace and automobile industry. Furthermore, industrial pressure vessels and other metal components, widely used in the chemical, petrochemical and power plant facilities, as well as pipes that are used to transmit or distribute hydrocarbon or other energy/water resources are the outcome of similar forming processes. In Chapter 4 of the present study a popular manufacturing process, the UOE process, will be presented. In general, the cyclic loading of some parts of the final product due to the forming process causes geometric imperfections as well as fields of residual stresses and strains. As a consequence, the structural behavior of the final product is highly influenced by the production procedure adopted.

Elbows are also important component of industrial piping components. They are initially curved tubular elements that are used as flexible connections in the piping system. Their performance under cyclic loading due to operational and seismic actions has attracted the scientific interest for a long time. Their initial curvature, the material nonlinearities resulting from the forming process and the potential presence of internal or external pressure highly affect their structural behavior. The combination of all the above is often responsible for the element failure. The failure can occur in many different forms with local or global buckling being the most catastrophic one [Slagis (1997)]. In every case, the material undergoes cyclic plastic deformations which have to be precisely predicted for the safe design of these elements.

Cyclic plasticity is also present in several structural engineering applications. Steel structural elements that undergo cyclic loading due to strong earthquake or wind generated intense actions are candidates for failure due to cyclic plasticity related phenomena. The requirement of precise prediction of the materials performance in the critical parts of a steel structure has motivated significant research in the area of constitutive modeling during the last three decades. Many advanced cyclic plasticity models are today employed by the engineering community in order to capture the total structure behavior starting from the material level. A brief overview for some of them follows.

1.2 Brief overview of the Cyclic Plasticity models

Significant research effort has been devoted in the formulation of phenomenological plasticity models to predict the behavior of materials subjected to cyclic loading. The models developed perform in a different manner and their efficiency in predicting the cyclic loading related effects has been extensively analyzed [Corona et al. (1996), Bari and Hassan (2000)]. Nevertheless, all the models are based on the same basic principles which stem from the classical theory of plasticity.

These characteristics are:

i) the additive decomposition of total strain in an elastic and a plastic part

ii) the yield criterion

iii) the flow rule

iv) the hardening rule.

<u>i) The total strain decomposition</u>

When loading takes place elastically, then the total strain is elastic and fully recoverable. When the elastic limit is excided, then the loading is elastoplastic. In this case we assume that the total strain is the sum of an elastic and a plastic part:

$$\boldsymbol{\varepsilon} = \boldsymbol{\varepsilon}^e + \boldsymbol{\varepsilon}^p \tag{1.1}$$

The elastic part is recoverable when the loading is removed, while the plastic part is permanent. The above equation is also used in its rate form.

<u>ii) The yield criterion</u>

The yield criterion defines whether at every stress increment the material behavior is elastic or inelastic and for classical metal plasticity it has the following general form $F\left(\boldsymbol{\sigma}, \boldsymbol{\alpha}, \varepsilon_q\right) = 0$, where $\boldsymbol{\sigma}$ is the stress tensor, $\boldsymbol{\alpha}$ is the tensor that describes the position of the center of the yield surface sometimes referred to as "backstress" and ε_q is the equivalent plastic strain.

For metal materials, it has been proven that the plastic deformation is not affected by the hydrostatic part of the stress tensor. Therefore, the initial yield criterion function depends only on the second and third deviatoric stress tensor invariants. $F\left(J_2, J_3\right)=0$.

The two most popular initial yield criteria for metal plasticity are the following:

a) The von Mises yield criterion:

$$F = 3J_2 - k^2 = 0 \tag{1.2}$$

also written as

$$F = \frac{1}{2}\mathbf{s}\cdot\mathbf{s} - \frac{k^2}{3} = 0 \tag{1.3}$$

b) The Tresca yield criterion:

$$F = 4\left(J_2\right)^3 - 27\left(J_3\right)^2 - 36k^2\left(J_2\right)^2 - 96k^4 J_2 - 64k^6 = 0 \tag{1.4}$$

In both criteria k is the size of the yield surface. In metal plasticity, the so called "J_2 – von Mises" yield criterion is widely used giving better results compared to the Tresca criterion.

iii) The flow rule

The flow rule governs the plastic strain rate increment through the use of a plastic multiplier $\dot{\lambda}$. In general:

$$\dot{\boldsymbol{\varepsilon}}^p = \dot{\lambda}\frac{\partial Q}{\partial \boldsymbol{\sigma}} \tag{1.5}$$

where Q is the so-called plastic potential function that depends on $(\boldsymbol{\sigma}, \boldsymbol{\alpha}, \varepsilon_q)$. In the case of associated plasticity for metals $Q \equiv F$, therefore:

$$\dot{\boldsymbol{\varepsilon}}^p = \dot{\lambda}\frac{\partial F}{\partial \boldsymbol{\sigma}} \tag{1.6}$$

iv) The hardening rule

The hardening rule describes the change of shape and location of the yield surface. Among other features it describes the evolution of the "backstress" tensor $\boldsymbol{\alpha}$ in the stress space and it can take several forms. In the following paragraphs the cases of Linear, Multilinear and Nonlinear hardening rules are briefly discussed.

1.2.1 Models using kinematic hardening rules

The simplest way to describe plasticity is the Perfect Plasticity model (sometimes refer to as Prandt- Reuss model). According to this model, the center of the yield surface is assumed fixed in the origin of the stress space and its size is

assumed constant. An advancement of the above model is the plasticity model that uses the isotropic hardening rule. In that case, the yield surface is assumed to remain fixed in the stress space and change size according to the magnitude of the equivalent plastic strain ε_q, which means that k is a function of ε_q.

An alternative class of plasticity models includes those that use the kinematic hardening rule in a Linear, Multilinear or Nonlinear form. According to this concept, the yield surface size can be assumed constant while the position of the yield surface center is described by the "backstress" tensor $\boldsymbol{\alpha}$. Moreover, some changes of size of the yield surface can be also taken into consideration combined with the kinematic hardening rule in any of the aforementioned forms. In the following paragraph the general features of the von Mises Plasticity model combined with the Kinematic hardening rule are discussed.

Von Mises Plasticity with Kinematic hardening

The von Mises (J_2) plasticity models employing the kinematic hardening rule examined in the present study have the following common characteristics:

a) The von Mises yield criterion:

$$F(\boldsymbol{\sigma}-\boldsymbol{\alpha}) = \frac{1}{2}(\mathbf{s}-\mathbf{a})\cdot(\mathbf{s}-\mathbf{a}) - \frac{k^2}{3} = 0 \tag{1.7}$$

b) The flow rule, written here in a more general form:

$$\dot{\varepsilon}^p = \frac{1}{H}\left\langle \frac{\partial F}{\partial \boldsymbol{\sigma}}\cdot\dot{\boldsymbol{\sigma}} \right\rangle \frac{\partial F}{\partial \boldsymbol{\sigma}} \tag{1.8}$$

c) The kinematic hardening rule:

$$\dot{\mathbf{a}} = g(\boldsymbol{\sigma}, \boldsymbol{\varepsilon}^p, \mathbf{a}, \dot{\boldsymbol{\sigma}}, \dot{\boldsymbol{\varepsilon}}^p, etc) \tag{1.9}$$

where $\boldsymbol{\sigma}$ is the stress tensor, $\boldsymbol{\varepsilon}^{\mathbf{p}}$ is the plastic strain tensor, $\mathbf{s}$ is the deviatoric stress tensor defined as $\mathbf{s} = \boldsymbol{\sigma} + p\mathbf{I}$ (p is the equivalent pressure stress and $\mathbf{I}$ is the identity tensor), $\boldsymbol{\alpha}$ is the current center of the yield surface, $\mathbf{a}$ is the current center of the yield surface in the deviatoric space, k is the size of the yield surface (constant for a cyclically stable material), and H is the plastic modulus. Also, $\langle\ \rangle$ indicates the MacCauley bracket and the dot express the inner product of two tensors.

The models discussed in the following paragraphs are distinguished in two groups. The categorization is based on the way that the hardening modulus is defined and this affects the translation or change of shape of the yield surface in the stress space in each plastic stress increment. The plastic modulus H can be defined in two different ways. The first way is through the consistency condition $\dot{F} = 0$,

which couples the hardening modulus with the kinematic hardening rule, as described in the classical model proposed by Prager (1956). The models that belong to this category are called as “coupled models”. The second category comprises the so-called “uncoupled” models.

The uncoupled models differ from the coupled models in the definition of the plastic modulus; the plastic modulus is defined directly and it is influenced only indirectly by the kinematic hardening rule. Examples of plasticity models that belong to this class are the models proposed by Dafalias and Popov (1976), Drucker and Palgen (1981) and Tseng and Lee (1983).

1.3 Coupled models for cyclic plasticity

Several plasticity models belong to this class, in which the kinematic hardening rules adopted can vary. A short description for some characteristic coupled models is given in the following paragraphs.

1.3.1 Linear and multilinear kinematic hardening rule

The linear kinematic hardening rule is the simplest model for cyclic plasticity modeling. Prager (1956) and Ziegler (1959) were the first to introduce the linear kinematic hardening model which employs a linear form of the kinematic hardening rule:

$$\dot{\mathbf{a}} = C\dot{\boldsymbol{\varepsilon}}^{p} \tag{1.10}$$

where C is a constant. The development of such a model is rather standard and it is described in several textbooks [Kyriakides and Corona (2007)].

Improvement to the linear kinematic hardening model was proposed by Mroz (1967) as a multisurface model, where each surface represents a constant work hardening modulus in the stress space.

1.3.2 The nonlinear kinematic hardening rules

From the large number of models that fall into this category, only the most representative ones are reported in the following paragraphs starting from the Armstrong Frederic model.

i. <u>The Armstrong and Frederic model</u>

The most well-known nonlinear kinematic hardening model has been proposed by Armstrong and Frederick (Armstrong and Frederick (1966)). This is a model that many researchers were base on as it will be noticed in the following paragraphs. Armstrong and Frederick introduced a kinematic hardening rule for the “backstress” containing a “recall' term which incorporates the fading memory effect

of the strain path and essentially makes the rule nonlinear in nature. The kinematic hardening rule in this model is given in the form:

$$\dot{\mathbf{a}} = C\dot{\boldsymbol{\varepsilon}}^{p} - \gamma \mathbf{a}\dot{\varepsilon}_{q} \tag{1.11}$$

where the equivalent plastic strain is defined as:

$$\dot{\varepsilon}_{q} = \sqrt{\frac{3}{2}\dot{\boldsymbol{\varepsilon}}^{P} \cdot \dot{\boldsymbol{\varepsilon}}^{P}} \tag{1.12}$$

and C , γ are parameters calibrated from cyclic test data. More specifically, C is the initial kinematic hardening modulus, and γ determines the rate at which the kinematic hardening modulus decreases with increasing plastic deformation.

The Armstrong - Frederick nonlinear kinematic hardening model was a breakthrough at the time it was introduced. Its advantages and capabilities were well appreciated by other researchers. Several of them applied improvements on its original form in order to improve its deficiencies and introduced new advanced models based on the same nonlinear hardening rule. Some characteristic models of this category will be briefly described below.

Models that employ the nonlinear kinematic hardening rule concept have also been proposed. They have some important similarities with the Armstrong – Frederick model, which are obvious through the equations formulation. The most characteristic models of this type are briefly presented and discussed in the following.

ii. <u>The Guionnet model</u>

Guionnet (1992) proposed a model which uses some parameters, determined from biaxial ratcheting experiments. The Guionnet model basically modifies the original Armstrong - Frederick hardening rule by incorporating the effect of accumulated plastic strain in it. For cyclically stabilized material, the kinematic hardening rule in this model is reduced to the form:

$$\begin{aligned} \dot{\mathbf{a}} &= mp_{1}^{m\text{-}1}\left[\left\{\frac{2}{3}C - \gamma_{1}\left(\mathbf{a}\cdot\mathbf{n}\right)\right\}\dot{\boldsymbol{\varepsilon}}^{p} - \left(\gamma_{2}a\right)\mathbf{a}dp\right], \\ \mathbf{n} &= \frac{2}{3}\left(\frac{d\boldsymbol{\varepsilon}^{p}}{dp}\right) \end{aligned} \tag{1.13}$$

where the coefficient a takes the following form:

$$\begin{aligned} &a = p_{1}^{n} = p_{1M}^{n},\ for\ p_{1} = p_{1M}, \\ &a = p_{1M}^{n}\left(\frac{p_{1M}}{p_{1M} + p_{1}}\right)^{\beta},\ for\ p_{1} \le p_{1M}, \\ &p_{1} = \int_{I_k}^{Q} dp\ and\ p_{1M} = \int_{I_{k-1}}^{I_k} dp \end{aligned} \tag{1.14}$$

Here, p_1 is the accumulated plastic strain between the last reversal (I_k and the current loading point (Q), and p_{1M} is the accumulated plastic strain between the last two reversals ($I_{k-1}$and I_k). The parameters C and γ are similar to those in the Armstrong and Frederick model and are determined from a uniaxial stable hysteresis curve. Two ratcheting parameters, $\gamma_2$and β are determined using a biaxial ratcheting response. No clear guidelines are provided by Guionnet (1992) to determine m and n .as reported by Bari and Hassan (2000).

iii. The Chaboche model

Chaboche and his co-workers (1979, 1986) proposed a model based on the decomposition of the nonlinear kinematic hardening rule proposed by Armstrong and Frederick in the form:

$$\dot{\mathbf{a}} = \sum_{i=1}^{M} \dot{\mathbf{a}}_i, \qquad \dot{\mathbf{a}}_i = C_i \dot{\boldsymbol{\varepsilon}}^p - \gamma_i \mathbf{a}_i \dot{\varepsilon}_q \tag{1.15}$$

iv. The Ohno and Wang model

The Ohno-Wang (1993) model is also a superposition of several kinematic hardening rules. It was introduced in the form:

$$\dot{\mathbf{a}} = \sum_{i=1}^{M} \dot{\mathbf{a}}_i, \qquad \dot{\mathbf{a}}_i = C_i \dot{\boldsymbol{\varepsilon}}^p - \gamma_i \mathbf{a}_i \left\langle \dot{\boldsymbol{\varepsilon}}^p \cdot \frac{\mathbf{a}_i}{f(a_i)} \right\rangle H\left\{ \mathbf{a}_i{}^2 - \left(\frac{C_i}{\gamma_i} \right)^2 \right\} \tag{1.16}$$

and H here stands for the Heaviside step function.

1.4 Uncoupled models for cyclic plasticity

In the case of the uncoupled models, the plastic modulus is defined directly by an expression and it is only indirectly influenced by the kinematic hardening rule. Three representative models of this category will be presented.

i. The Drucker - Palgen model

According to the Drucker – Palgen (1981) model, the plastic modulus H is assumed to be strictly a function of the second invariant of the deviatoric stress tensor J_2 of the following form:

$$H = \left(A J_2^N \right)^{-1} \tag{1.17}$$

where A and N are material constants evaluated from a segment of a stable hysteresis loop.

ii. The Dafalias - Popov model

The Dafalias – Popov (1976) model constitutes one of the most effective models to describe complex loading histories including cyclic plasticity. In this model,

in addition to the yield surface the concept of a “Bounding Surface” is introduced, which obeys kinematic hardening. The yield surface is free to translate within the bounding surface describing any possible stress state. During excessive loading these two surfaces may come in contact at a unique point that describes the current stress state. If loading continuous into the plastic regime, then the two surfaces translate together, so that an intersection may not occur.

Special attention is also paid on the definition of the plastic modulus in order to achieve a smooth transition from the elastic to the fully-plastic state which is also compatible with experimental observations. The model accounts for the gradual decrease of the value of H as hardening proceeds, and this evolution is of great importance for the successful modeling of a complex loading history associated with reverse plastic loading, especially in cases where Bauschinger effects are important.

The basic idea of this model is that the current tangent modulus depends on the "distance" δ in stress space of the current stress state and of that representing the immediately previous elastic stress state from a *bounding surface*. The plastic modulus *H* is described as follows:

$$H(\delta,\delta_{in}) = E_0^p + h(\delta_{in})\left(\frac{\delta}{\delta_{in}-\delta}\right) \tag{1.18}$$

where E_0^p is the (final) constant value of the plastic modulus tends to after sufficient plastic strain, δ_{in} is the distance of the last elastic state point from the bound and $h(\delta_{in})$ is a model parameter function of δ_{in} which controls the “steepness” of the stress-strain curve and is defined as follows:

$$h(\delta_{in}) = \frac{\alpha}{1+b\left(\frac{\delta_{in}}{2\sigma_b}\right)^m} \tag{1.19}$$

In the above equation α , b and m are model constants and σ_b is the size of the Bounding Surface. Function h is calibrated through an experimental stress-strain curve.

iii. <u>The Tseng – Lee model</u>

The Tseng – Lee (1983) model is similar to the model outlined above, except that the bounding surface is replaced by the so-called “*memory surface”*. This surface is centered at the origin and hardens isotropically every time its stress level is exceeded. Thus, it represents the biggest state of stress developed in the loading history. During initial loading, since the two surfaces are in contact, the flow rule is

based on the memory surface. During the loading phase the yield surface stays attached to the memory surface at the current stress point. It detaches on the first reverse loading that includes plastic deformation. Then the plastic modulus is described as follows:

$$H(\delta,\delta_{in}) = E_m^p\left[1+h\left(\frac{\delta}{\delta_{in}-\delta}\right)\right] \tag{1.20}$$

where E_m^p is the plastic modulus of the memory surface after sufficient plastic strain. Similarly δ_{in} is the value of δ at the last elastic state

1.5 Scope of the present study

The present study aims at the detailed examination of the Armstrong – Frederick cyclic plasticity model. For all the variations of this model, the corresponding equations are extensively discussed in Chapter 2. Moreover the numerical integration of the governing equations is also presented. The effect of the model parameters on the predicted cyclic behavior of steel are examined through simple one-element tests.

The nonlinear kinematic hardening rule combined with a J2 von Mises plasticity model formulation is used to simulate two cyclic plasticity problems. The first problem refers to the bending of tubes and it is reported in Chapter 3. The moment capacity of a tube subjected to monotonic, symmetric and asymmetric cyclic bending is examined. The effect of the plasticity model used to simulate the tube bending problem on the ovalization of the cross section and moment capacity prediction is also discussed.

In Chapter 3, the combination of internal pressure and cyclic bending of a tube is also examined. The effect of the internal pressure on the ultimate capacity of the tube is examined along with cyclic plasticity related phenomena such as ratcheting. The simulation of a similar problem discussed by Rahman et al (2007) is also presented and the numerical results are compared with experimental measurements.

Finally, in Chapter 4 of the present study, the UOE pipe manufacturing process is presented for a 24-inch line pipe. The forming process induces plastisfication of the pipe cross section and as a consequence, its ultimate capacity against external pressure is significantly affected. This effect is simulated with a J2-plasticity constitutive model adopting the isotropic, kinematic and nonlinear kinematic hardening rule. The capabilities of each hardening rule to simulate the forming process accurately and predict the maximum collapse pressure of the 24-inch pipe are compared results from a more elaborate model presented by Herynk et al (2007).

2. The Armstrong - Frederick model.

Model equations and numerical implementation

In the present paragraph the features of the Armstrong – Frederick model are presented. The constitutive equations of the two model variations and their numerical implementation are discussed in detail. The Armstrong – Frederick model and the nonlinear kinematic hardening rule it adopts is advancement of the simpler linear kinematic hardening model. The aforementioned models are presented bellow.

2.1 Linear and nonlinear kinematic hardening models

The von Mises plasticity model, which uses the linear kinematic hardening rule, has been appreciated by many researchers for its simplicity and the benefits it provides in modeling cyclic plasticity effects compared to the use of simple isotropic hardening rule [Kyriakides and Corona (2007)]. In several applications it has been proven an adequate model. However, the use of linear kinematic hardening rule provides limited capabilities when it is used to simulate accurately cyclic loading histories in the plastic range.

The Armstrong – Frederick model (Armstrong and Frederick (1966)) is an enhancement of the linear kinematic hardening model. It introduces a nonlinear term on the evolution law added to the linear one and can be used to model phenomena such as the Bauschinger effect and cyclic creep. Furthermore it can be combined with an isotropic part which accounts for the change of size of the yield surface, and may model cyclic hardening/softening.

More specifically, the Armstrong – Frederick model can be expressed in two different ways depending on the assumption made for the size of the yield surface. The size of the yield surface can be assumed either to remain constant or it can be allowed to change while plastic deformation takes place. On those grounds, the adopted formulation distinguishes between the so-called “nonlinear kinematic hardening model” which does not allow for change of size of the yield surface and the “nonlinear kinematic/isotropic hardening model” which accounts for yield surface change of size. Both model variations will be discussed in detail in the following paragraphs. Before proceeding to the presentation of the two versions of the Armstrong – Frederick model, it is judged necessary to present the linear kinematic hardening model equations.

2.1.1 Review of the linear kinematic hardening model

The von Mises plasticity model which uses the linear kinematic hardening rule is the basis of all the models using the kinematic hardening rule. It is based on the concept that the yield surface has constant size and it is free to move into the stress space. The pressure independent von Mises yield surface is given by the following expression:

$$F = \frac{1}{2}(\mathbf{s}-\mathbf{a})\cdot(\mathbf{s}-\mathbf{a}) - \frac{k^2}{3} = 0 \tag{2.1}$$

where $\mathbf{s}$ is the deviatoric stress tensor defined as $\mathbf{s} = \boldsymbol{\sigma} + p\mathbf{I}$ (p is the equivalent pressure stress and $\mathbf{I}$ is the identity tensor), $\mathbf{a}$ is the back stress tensor that expresses the current center of the yield surface in the deviatoric space and k is the parameter that defines the size of the yield surface. In this model k is constant.

Furthermore, the linear kinematic hardening model assumes an associated plastic flow defined as:

$$\dot{\boldsymbol{\varepsilon}}^p = \dot{\lambda}\frac{\partial F}{\partial \boldsymbol{\sigma}} = \dot{\lambda}(\mathbf{s}-\mathbf{a}) \tag{2.2}$$

The equivalent plastic strain rate is defined as:

$$\begin{aligned} \dot{\varepsilon}_q &= \sqrt{\frac{3}{2}\dot{\boldsymbol{\varepsilon}}^P \cdot \dot{\boldsymbol{\varepsilon}}^P} \\ \dot{\varepsilon}_q &= \frac{2}{3}\dot{\lambda}k \end{aligned} \tag{2.3}$$

Combining the above equations,

$$\dot{\boldsymbol{\varepsilon}}^p = \frac{3}{2k}\dot{\varepsilon}_q(\mathbf{s}-\mathbf{a}) \tag{2.4}$$

The linear kinematic hardening rule is described by the following linear expression:

$$\dot{\mathbf{a}} = C\dot{\boldsymbol{\varepsilon}}^p \tag{2.5}$$

where C is the kinematic hardening modulus which is considered constant and $\dot{\boldsymbol{\varepsilon}}^p$ is the plastic strain rate defined in Eq. (2.2).

Enforcing the consistency condition $\dot{F}=0$, expressed as follows:

$$\frac{\partial F}{\partial \boldsymbol{\sigma}}\cdot\dot{\boldsymbol{\sigma}} + \frac{\partial F}{\partial \mathbf{a}}\cdot\dot{\mathbf{a}} = 0 \tag{2.6}$$

one results that the plastic loading parameter $\dot{\lambda}$ equals to:

$$\dot{\lambda} = \frac{3}{2k^2}\frac{1}{C}(\mathbf{s}-\mathbf{a})\cdot\dot{\mathbf{s}} \tag{2.7}$$

or equivalently, taking into account Eq.(2.3), the equivalent plastic strain rate $\dot{\varepsilon}_q$ is written as:

$$\dot{\varepsilon}_q = \frac{1}{kC}(\mathbf{s}-\mathbf{a})\cdot\dot{\mathbf{s}} \tag{2.8}$$

It is straight forward to relate C to the hardening modulus from a uniaxial tension test.

The general elasticity equation is used next,

$$\boldsymbol{\sigma} = \mathbf{D}\boldsymbol{\varepsilon}^e \tag{2.9}$$

which can also be written in its rate form

$$\dot{\boldsymbol{\sigma}} = \mathbf{D}\dot{\boldsymbol{\varepsilon}}^e \tag{2.10}$$

where $\mathbf{D}$ is the forth order elastic rigidity tensor and $\boldsymbol{\varepsilon}^e$ is the elastic strain tensor. It is further assumed that the total strain tensor is decomposed into an elastic and a plastic part:

$$\boldsymbol{\varepsilon} = \boldsymbol{\varepsilon}^e + \boldsymbol{\varepsilon}^p \tag{2.11}$$

Using the above decomposition and substituting in to the rate form of the general elasticity equation(2.10) one obtains:

$$\begin{aligned} \dot{\boldsymbol{\sigma}} &= \mathbf{D}(\dot{\boldsymbol{\varepsilon}} - \dot{\boldsymbol{\varepsilon}}^P) \\ \dot{\boldsymbol{\sigma}} &= \mathbf{D}\dot{\boldsymbol{\varepsilon}} - \mathbf{D}\dot{\lambda}(\mathbf{s} - \mathbf{a}) \end{aligned} \tag{2.12}$$

Since $(\mathbf{s}-\boldsymbol{\alpha})$ is a deviatoric tensor, one can readily show that the product $\mathbf{D}(\mathbf{s}-\boldsymbol{\alpha})$ is equal to $2G(\mathbf{s}-\boldsymbol{\alpha})$. Using this tensor property and Eq.(2.7) , Eq.(2.12) can be rewritten as:

$$\dot{\boldsymbol{\sigma}} = \mathbf{D}\dot{\boldsymbol{\varepsilon}} - \frac{3G}{k}\dot{\varepsilon}_q(\mathbf{s}-\mathbf{a}) \tag{2.13}$$

For the simplification of the product $[(\mathbf{s}-\mathbf{a})\cdot\dot{\mathbf{s}}]$ in Eq.(2.8), both parts of the rate form of the general elasticity equation are multiplied with the term $(\mathbf{s}-\mathbf{a})$. This results in:

$$\dot{\mathbf{s}}\cdot(\mathbf{s}-\mathbf{a}) = (\mathbf{D}\dot{\boldsymbol{\varepsilon}})\cdot(\mathbf{s}-\mathbf{a}) - 2Gk\dot{\varepsilon}_q \tag{2.14}$$

and using Eq. (2.8), the final expression of the equivalent plastic strain rate is

$$\begin{aligned} \dot{\varepsilon}_q &= \frac{1}{B}\left(\mathbf{D}\dot{\boldsymbol{\varepsilon}}\right)\cdot(\mathbf{s}-\mathbf{a}), \\ B &= kC + 2Gk \end{aligned} \tag{2.15}$$

Defining tensor $\boldsymbol{\xi}$ as the tensor difference $\mathbf{s}-\mathbf{a}$ and using Eq.(2.15), the incremental stress-strain relations Eq. (2.13) can be rewritten as:

$$\begin{aligned} \dot{\boldsymbol{\sigma}} &= \left(\mathbf{D} - \frac{6G^2}{kB}(\boldsymbol{\xi}\otimes\boldsymbol{\xi})\right)\dot{\boldsymbol{\varepsilon}} \\ \mathbf{D}^{ep} &= \mathbf{D} - \frac{6G^2}{kB}(\boldsymbol{\xi}\otimes\boldsymbol{\xi}) \end{aligned} \tag{2.16}$$

where $\mathbf{D}^{ep}$ is the fourth-order elastoplastic rigidity tensor and $\otimes$ denotes the tensor product of two second order tensors.

2.1.2 Nonlinear kinematic hardening model

For the description of the Armstrong - Frederick model, which adopts the nonlinear kinematic hardening rule, J_2-plasticity theory is used adopting the pressure- independent von Mises yield surface as described in Eq.(2.1). In the formulation of the model in the present section, the yield surface is free to move within the stress space, while the size of it is assumed constant.

The nonlinear kinematic hardening model assumes associated plastic flow. Therefore, the plastic strain rate is defined as in Eq.(2.2), the equivalent plastic strain rate is defined as in Eq.(2.3). Combination of these two equations results in Eq.(2.4) for the plastic strain increment.

The nonlinear kinematic hardening rule is expressed as follows:

$$\dot{\mathbf{a}} = C\dot{\boldsymbol{\varepsilon}}^p - \gamma\mathbf{a}\dot{\varepsilon}_q \tag{2.17}$$

where C is the linear kinematic hardening modulus and γ is the parameter that determines the rate at which the kinematic hardening modulus decreases with increasing plastic deformation.

Enforcing the consistency condition $\dot{F}=0$, as described in Eq.(2.6), one results in the following expression the plastic parameter $\dot{\lambda}$:

$$\dot{\lambda} = \frac{3}{2k}\frac{1}{[kC - \gamma \mathbf{a}\cdot(\mathbf{s}-\mathbf{a})]}(\mathbf{s}-\mathbf{a})\cdot\dot{\mathbf{s}} \tag{2.18}$$

or equivalently, taking into account Eq.(2.3) , the equivalent plastic strain rate $\dot{\varepsilon}_q$ is written as:

$$\dot{\varepsilon}_q = \frac{1}{[kC - \gamma \mathbf{a}\cdot(\mathbf{s}-\mathbf{a})]}(\mathbf{s}-\mathbf{a})\cdot\dot{\mathbf{s}} \tag{2.19}$$

Substitution of Eq.(2.19) into Eq.(2.4) results in the following expression for the plastic strain rate:

$$\dot{\boldsymbol{\varepsilon}}^p = \frac{3}{2k}\frac{1}{[kC - \gamma \mathbf{a}\cdot(\mathbf{s}-\mathbf{a})]}[(\mathbf{s}-\mathbf{a})\cdot\dot{\mathbf{s}}](\mathbf{s}-\mathbf{a}) \tag{2.20}$$

The general elasticity equations described in Eq.(2.9) and Eq.(2.10) are also valid and the total strain tensor is decomposed into an elastic and a plastic part as written in Eq.(2.11). Using the above decomposition also on a rate form and substituting it to the rate form of the general elasticity equation, one results in Eq.(2.12).

Following the same procedure as described in section 2.1.1, the final expression of the rate of the equivalent plastic strain rate is now written as:

$$\dot{\varepsilon}_q = \frac{1}{B}\left(\mathbf{D}\dot{\boldsymbol{\varepsilon}}\right)\cdot(\mathbf{s}-\mathbf{a}) \tag{2.21}$$

where $$\mathrm{B} = kC - \gamma \mathbf{a}\cdot(\mathbf{s}-\mathbf{a}) + 2Gk$$

Defining tensor $\boldsymbol{\xi}$ as the tensor difference $\mathbf{s}-\mathbf{a}$ and using Eq.(2.21) , Eq.(2.13) can be now rewritten as follows:

$$\begin{aligned} \dot{\boldsymbol{\sigma}} &= \mathbf{D}^{ep}\dot{\boldsymbol{\varepsilon}} \\ \mathbf{D}^{ep} &= \mathbf{D} - \frac{6G^2}{kB}(\boldsymbol{\xi}\otimes\boldsymbol{\xi}) \end{aligned} \tag{2.22}$$

where $\mathbf{D}^{ep}$ is the fourth-order elastoplastic rigidity tensor and $\otimes$ denotes the tensor product of two second order tensors.

2.1.3 Nonlinear kinematic/isotropic (combined) hardening model

The most general version of the Armstrong – Frederick model assumes that the size of the yield surface is no longer a constant, but it is allowed to change depending on the amount of the equivalent plastic strain; that is $k = k(\varepsilon_q)$. The equation describing the von Mises yield surface is now written as:

$$F = \frac{1}{2}(\mathbf{s}-\mathbf{a})\cdot(\mathbf{s}-\mathbf{a}) - \frac{k^2(\varepsilon_q)}{3} = 0 \tag{2.23}$$

where $\mathbf{s}$ is the deviatoric stress tensor defined as $\mathbf{s}=\boldsymbol{\sigma}+p\mathbf{I}$ (p is the equivalent pressure stress and $\mathbf{I}$ is the identity tensor), $\mathbf{a}$ is the current center of the yield surface in the deviatoric space and $k(\varepsilon_q)$ is now a function of the equivalent plastic strain that defines the size of the yield surface. Following the same procedure described previously for the nonlinear kinematic hardening, the modifications of the aforementioned equations due to the substitution of the yield size k by the function $k(\varepsilon q)$ will be presented.

The plastic strain rate is defined in Eq.(2.2), the equivalent plastic strain rate is defined in Eq.(2.3) and combining these two equations one results in an expression for the plastic strain increment identical to Eq.(2.4).

The nonlinear kinematic hardening rule is described by the following expression:

$$\dot{\mathbf{a}} = C\dot{\boldsymbol{\varepsilon}}^{p} - \gamma \mathbf{a}\dot{\varepsilon}_q \tag{2.24}$$

where C is the linear kinematic hardening modulus and γ is the parameter that determines the rate at which the kinematic hardening modulus decreases with increasing plastic deformation.

The consistency condition $\dot{F}$=0 now contains one more term related to the size of the yield surface and it is expressed as follows:

$$\begin{aligned} &\frac{\partial F}{\partial \boldsymbol{\sigma}}\cdot\dot{\boldsymbol{\sigma}} + \frac{\partial F}{\partial \mathbf{a}}\cdot\dot{\mathbf{a}} + \frac{\partial F}{\partial k}\cdot\dot{k} = 0 \\ &\dot{k} = \frac{dk(\varepsilon_q)}{d\varepsilon_q} \end{aligned} \tag{2.25}$$

Adopting a procedure similar to the one followed previously, one obtains that the plastic parameter $\dot{\lambda}$ equals to:

$$\dot{\lambda} = \frac{3}{2k(\varepsilon_q)} \frac{1}{\left[k(\varepsilon_q)C - \gamma\mathbf{a}\cdot(\mathbf{s}-\mathbf{a}) + \frac{2}{3}k(\varepsilon_q)\frac{dk(\varepsilon_q)}{d\varepsilon_q} \right]} (\mathbf{s}-\mathbf{a})\cdot\dot{\mathbf{s}} \tag{2.26}$$

or equivalently, taking into account Eq.(2.3), the equivalent plastic strain rate $\dot{\varepsilon}_q$ is written as:

$$\dot{\varepsilon}_q = \frac{1}{\left[kC - \gamma\mathbf{a}\cdot(\mathbf{s}-\mathbf{a}) + \frac{2}{3}k(\varepsilon_q)\frac{dk(\varepsilon_q)}{d\varepsilon_q} \right]} (\mathbf{s}-\mathbf{a})\cdot\dot{\mathbf{s}} \tag{2.27}$$

Substitution of Eq.(2.27) into Eq.(2.4) results in the following expression for the plastic strain rate:

$$\dot{\boldsymbol{\varepsilon}}^{\mathbf{p}} = \frac{3}{2k} \frac{1}{\left[kC - \gamma\mathbf{a}\cdot(\mathbf{s}-\mathbf{a}) + \frac{2}{3}k(\varepsilon_q)\frac{dk(\varepsilon_q)}{d\varepsilon_q} \right]} [(\mathbf{s}-\mathbf{a})\cdot\dot{\mathbf{s}}](\mathbf{s}-\mathbf{a}) \tag{2.28}$$

Following the same procedure as described in section 2.1.1, the final expression of the equivalent plastic strain rate is now written as:

$$\dot{\varepsilon}_q = \frac{1}{B}\left(\mathbf{D}\dot{\boldsymbol{\varepsilon}}\right)\cdot(\mathbf{s}-\mathbf{a}) \tag{2.29}$$

$$\mathrm{B} = kC - \gamma\mathbf{a}\cdot(\mathbf{s}-\mathbf{a}) + \frac{2}{3}k(\varepsilon_q)\frac{dk(\varepsilon_q)}{d\varepsilon_q} + 2Gk$$

Defining tensor $\boldsymbol{\xi}$ as the tensor difference $\mathbf{s}-\mathbf{a}$ and using Eq.(2.21) , the Eq.(2.13) can be now rewritten as follows:

$$\dot{\boldsymbol{\sigma}} = \mathbf{D}^{ep}\dot{\boldsymbol{\varepsilon}} \tag{2.30}$$

$$\mathbf{D}^{ep} = \mathbf{D} - \frac{6G^2}{kB}(\boldsymbol{\xi}\otimes\boldsymbol{\xi})$$

where $\mathbf{D}^{ep}$ is the fourth-order elastoplastic rigidity tensor and $\otimes$ denotes the tensor product of two second order tensors.

2. 2 Numerical implementation of the Armstrong – Frederick model

The numerical integration of the models described in the previous section is based on a standard "elastic predictor – plastic corrector" scheme. At the beginning of each step, elastic prediction takes place. During this step the total material behavior is assumed elastic and the stress prediction is based on the trivial integration of the elasticity equations. The validity of this assumption is verified by a check, which demands that the von Mises yield criterion is not violated by the elastically predicted stress. If this check is not passed, then it is assumed that the step is elastoplastic and therefore the elastoplastic equations are used. These two steps are described in detail in the following.

2.2.1 Numerical implementation of the linear kinematic hardening model

The problem under consideration can be expressed as follows:

At a specific integration point, for given state $(\mathbf{s}_n, \mathbf{a}_n, \varepsilon_{qn})$ and a given strain increment $\Delta\boldsymbol{\varepsilon}$, the new state parameters $(\mathbf{s}_{n+1}, \mathbf{a}_{n+1}, \varepsilon_{qn+1})$ are sought:

1. Elastic Prediction

Assume $\Delta\boldsymbol{\varepsilon} = \Delta\boldsymbol{\varepsilon}^e$.

Following a direct integration of the elasticity equations, elastic prediction of stresses $\boldsymbol{\sigma}^{(e)}$ can be written as:

$$\boldsymbol{\sigma}^{(e)} = \boldsymbol{\sigma}_n + \mathbf{D}\Delta\boldsymbol{\varepsilon} \tag{2.31}$$

The deviatoric form of the above equation is:

$$\mathbf{s}_{n+1} = \mathbf{s}_n + \mathbf{D}\Delta\boldsymbol{\varepsilon}$$
$$\mathbf{s}_{n+1} = \mathbf{s}^{(e)} \tag{2.32}$$

Since no plastic loading is assumed to take place during this step:

$$\dot{\mathbf{a}} = \mathbf{0} \tag{2.33}$$

or equivalently:

$$\mathbf{a}_{n+1} = \mathbf{a}_n \tag{2.34}$$

A check must be performed to examine whether the yield criterion is satisfied:

$$F = \frac{1}{2}(\mathbf{s}_{n+1} - \mathbf{a}_{n+1}) \cdot (\mathbf{s}_{n+1} - \mathbf{a}_{n+1}) - \frac{k^2}{3} \leq 0 \tag{2.35}$$

If yes, then the elastic stress prediction is valid and the step is elastic. If no, then go to the plastic corrector step.

2. Plastic Correction

From the rate form of the general elasticity equation it results that:

$$\dot{\boldsymbol{\sigma}} = \mathbf{D}\dot{\boldsymbol{\varepsilon}}^e$$
$$\dot{\boldsymbol{\sigma}} = \mathbf{D}(\dot{\boldsymbol{\varepsilon}} - \dot{\boldsymbol{\varepsilon}}^P) \tag{2.36}$$

Integration of the above equation provides:

$$\boldsymbol{\sigma}_{n+1} = \boldsymbol{\sigma}_n + \mathbf{D}\Delta\boldsymbol{\varepsilon} - \mathbf{D}\Delta\boldsymbol{\varepsilon}^p$$
$$\boldsymbol{\sigma}_{n+1} = \boldsymbol{\sigma}^{(e)} - 2G\Delta\boldsymbol{\varepsilon}^p \tag{2.37}$$

The flow rule is

$$\dot{\boldsymbol{\varepsilon}}^p = \frac{3}{2k}\dot{\varepsilon}_q(\mathbf{s} - \mathbf{a}) \tag{2.38}$$

is integrated as follows:

$$\Delta\boldsymbol{\varepsilon}^p = \frac{3}{2k}\Delta\varepsilon_q(\mathbf{s}_{n+1} - \mathbf{a}_{n+1}) \tag{2.39}$$

and because $(\mathbf{s} - \boldsymbol{\alpha})$ is deviatoric, using the property of tensor $\mathbf{D}$:

$$\mathbf{D}(\mathbf{s} - \boldsymbol{\alpha}) = 2G(\mathbf{s} - \boldsymbol{\alpha}) \tag{2.40}$$

the deviatoric part of the above equation is written as:

$$\mathbf{s}_{n+1} = \mathbf{s}^{(e)} - \frac{3G}{k}\Delta\varepsilon_q\boldsymbol{\xi}_{n+1} \tag{2.41}$$

Subsequently, the linear kinematic hardening rule,

$$\dot{\mathbf{a}} = C\dot{\boldsymbol{\varepsilon}}^p$$
$$\dot{\mathbf{a}} = C\frac{3}{2k}\dot{\varepsilon}_q(\mathbf{s} - \mathbf{a}) \tag{2.42}$$

is integrated to obtain

$$\mathbf{a}_{n+1} = \mathbf{a}_n + C\frac{3}{2k}\Delta\varepsilon_q\boldsymbol{\xi}_{n+1} \tag{2.43}$$

To proceed, it is necessary to write the tensor $\boldsymbol{\xi}_{n+1}$ as the difference of $\mathbf{s}_{n+1}$, $\mathbf{a}_{n+1}$. Towards this purpose (2.41) and (2.43) are combined:

$$\boldsymbol{\xi}_{n+1} = \mathbf{s}^{(e)} - \frac{3G}{k}\Delta\varepsilon_q\boldsymbol{\xi}_{n+1} - \left(\mathbf{a}_n + C\frac{3}{2k}\Delta\varepsilon_q\boldsymbol{\xi}_{n+1}\right) \tag{2.44}$$

or equivalently:

$$\boldsymbol{\xi}_{n+1} = \frac{1}{AFACT}\left(\mathbf{s}^{(e)} - \mathbf{a}_n\right)$$
$$AFACT = 1 + \frac{3}{k}\left(G + \frac{C}{2}\right)\Delta\varepsilon_q \tag{2.45}$$

and verify that $\bar{\xi} = k$, where

$$\bar{\xi} = \sqrt{\frac{3}{2}\boldsymbol{\xi}_{n+1} \cdot \boldsymbol{\xi}_{n+1}} \tag{2.46}$$

The value of the plastic parameter $\Delta\varepsilon_q$ can be given by the following closed form equation:

$$\Delta\varepsilon_q = \frac{q_{(e)} - k}{3\left(G + \frac{C}{2}\right)} \tag{2.47}$$

where $$q_{(e)}^2 = \frac{3}{2}\left(\mathbf{s}^{(e)} - \mathbf{a}_n\right) \cdot \left(\mathbf{s}^{(e)} - \mathbf{a}_n\right)$$

2.2.2 Numerical implementation of the nonlinear kinematic/isotropic (combined) hardening model

The numerical implementation of the nonlinear kinematic hardening model and the nonlinear kinematic/isotropic hardening model follows the same "elastic predictor – plastic corrector" scheme as described above. The elastic predictor step remains the same as in the case of the nonlinear kinematic hardening model. The plastic corrector step is modified accordingly since in this case the size of the yield surface is not a constant but a function of the equivalent plastic strain.

Here the numerical implementation of the nonlinear kinematic/isotropic hardening model is presented. The numerical implementation of the nonlinear kinematic hardening model (with constant size of yield surface) is a sub case. The present numerical scheme results assuming that the size of the yield surface is constant and its derivative with respect to the equivalent plastic strain equal to zero.

More specifically: for given state $(\mathbf{s}_n, \mathbf{a}_n, \varepsilon_{qn})$ and a given strain increment $\Delta\boldsymbol{\varepsilon}$, the new state parameters $(\mathbf{s}_{n+1}, \mathbf{a}_{n+1}, \varepsilon_{qn+1})$ are sought:

1. Elastic Prediction

Following a direct integration of the elasticity equations, elastic prediction can be written as:

$$\boldsymbol{\sigma}^{(e)} = \boldsymbol{\sigma}_n + \mathbf{D}\Delta\boldsymbol{\varepsilon} \tag{2.48}$$

The deviatoric form of the above equation is:

$$\mathbf{s}^{(e)} = \mathbf{s}_n + \mathbf{D}\Delta\boldsymbol{\varepsilon} \tag{2.49}$$

Since no plastic loading is assumed to take place during this step:

$$\dot{\mathbf{a}} = 0$$
$$\dot{\varepsilon}_q = 0 \tag{2.50}$$

A check must be performed to examine whether the yield criterion is satisfied:

$$F = \frac{1}{2}(\mathbf{s}^{(e)} - \mathbf{a}_n)\cdot(\mathbf{s}^{(e)} - \mathbf{a}_n) - \frac{k^2(\varepsilon_{qn})}{3} \le 0 \tag{2.51}$$

If yes, then elastic stress prediction is valid and the step is elastic. In such a case, $\mathbf{a}_{n+1} = \mathbf{a}_n$, $\varepsilon_{qn+1} = \varepsilon_{qn}$ and $\boldsymbol{\sigma}_{n+1} = \boldsymbol{\sigma}^{(e)}$, $\mathbf{s}_{n+1} = \mathbf{s}^{(e)}$. If no, then go to the Plastic Corrector.

2. Plastic Corrector Step

The nonlinear kinematic hardening rule:

$$\dot{\mathbf{a}} = C\dot{\boldsymbol{\varepsilon}}^p - \gamma\mathbf{a}\dot{\varepsilon}_q \tag{2.52}$$

can be written $$\dot{\mathbf{a}} = C\frac{3}{2k}\dot{\varepsilon}_q(\mathbf{s}-\mathbf{a}) - \gamma\mathbf{a}\dot{\varepsilon}_q$$

Substituting $\boldsymbol{\xi}$ for $(\mathbf{s}-\mathbf{a})$ and integrating over the step one results in:

$$\mathbf{a}_{n+1} = \mathbf{a}_n + C\frac{3}{2k(\varepsilon_{qn+1})}\Delta\varepsilon_q\boldsymbol{\xi}_{n+1} - \gamma\mathbf{a}_{n+1}\Delta\varepsilon_q \tag{2.53}$$

Equivalently,

$$\mathbf{a}_{n+1} = \frac{1}{1+\gamma\Delta\varepsilon_q}\left(\mathbf{a}_n + C\frac{3}{2k(\varepsilon_{qn+1})}\Delta\varepsilon_q\boldsymbol{\xi}_{n+1}\right) \tag{2.54}$$

Integrating the elasticity equations:

$$\Delta\boldsymbol{\sigma} = \mathbf{D}\Delta\boldsymbol{\varepsilon} - \mathbf{D}\Delta\boldsymbol{\varepsilon}^p \tag{2.55}$$

the above equation is written as:

$$\begin{aligned}\boldsymbol{\sigma}_{n+1} &= \boldsymbol{\sigma}_n + \mathbf{D}\Delta\boldsymbol{\varepsilon} - \mathbf{D}\Delta\boldsymbol{\varepsilon}^p \\ \boldsymbol{\sigma}_{n+1} &= \boldsymbol{\sigma}^{(e)} - 2G\Delta\boldsymbol{\varepsilon}^p\end{aligned} \tag{2.56}$$

Furthermore, the flow rule is integrated as follows:

$$\Delta\boldsymbol{\varepsilon}^p = \frac{3}{2k(\varepsilon_q)}\Delta\varepsilon_q(\mathbf{s}_{n+1} - \mathbf{a}_{n+1}) \tag{2.57}$$

and using the deviatoric tensor property of the rigidity tensor:

$$\mathbf{D}(\mathbf{s}-\boldsymbol{\alpha}) = 2G\boldsymbol{\xi} \tag{2.58}$$

the deviatoric part of the above equation is written as:

$$\mathbf{s}_{n+1} = \mathbf{s}^{(e)} - \frac{3G}{k(\varepsilon_{qn+1})}\Delta\varepsilon_q\boldsymbol{\xi}_{n+1} \tag{2.59}$$

From Eq.(2.54) and Eq.(2.59) the tensor $\boldsymbol{\xi}_{n+1}$ can be written as follows:

$$\boldsymbol{\xi}_{n+1} = \mathbf{s}^{(e)} - \frac{3G}{k(\varepsilon_{qn+1})}\Delta\varepsilon_q\boldsymbol{\xi}_{n+1} - \frac{1}{1+\gamma\Delta\varepsilon_q}\left(\mathbf{a}_n + C\frac{3}{2k(\varepsilon_{qn+1})}\Delta\varepsilon_q\boldsymbol{\xi}_{n+1}\right) \tag{2.60}$$

Equivalently:

$$\begin{aligned}\boldsymbol{\xi}_{n+1} &= \frac{1}{AFACT}\left(\mathbf{s}^{(e)} - \frac{1}{1+\gamma\Delta\varepsilon_q}\mathbf{a}_n\right) \\ AFACT &= 1 + \frac{3}{k(\varepsilon_{qn+1})}\left(G + \frac{C}{2(1+\gamma\Delta\varepsilon_q)}\right)\Delta\varepsilon_q\end{aligned} \tag{2.61}$$

Because of the consistency property of the flow rule, the new state parameters should satisfy the yield condition. This equation results to a nonlinear algebraic equation in terms of $\Delta\varepsilon_q$.

$$\frac{1}{2}\boldsymbol{\xi}_{n+1}\cdot\boldsymbol{\xi}_{n+1}-\frac{1}{2}k^2(\varepsilon_{qn+1})=0 \tag{2.62}$$

The above equation is solved in terms of the unknown $\Delta\varepsilon_q$ with the use of an iterative Newton – Raphson scheme as follows:

$$\Delta\varepsilon_{q(i+1)}=\Delta\varepsilon_{q(i)}-\frac{f\left(\Delta\varepsilon_q\right)_{(i)}}{f'\left(\Delta\varepsilon_q\right)_{(i)}} \tag{2.63}$$

where $f'\left(\Delta\varepsilon_q\right)=\dfrac{df\left(\Delta\varepsilon_q\right)}{d\Delta\varepsilon_q}$.

The nonlinear procedure is continued until the following criterion is satisfied:

$$\frac{\Delta\varepsilon_{q(i+1)}}{\Delta\varepsilon_{q(i)}}\le E \tag{2.64}$$

where E is the desired tolerance.

In general, the function $k(\varepsilon_q)$ can take several forms. The user has to define the desired form based on experimental data (hardening or softening).

2.3 Plane stress formulation and numerical integration

In this section the application of the backward Euler method to problems of plane stress is discussed. In such problems, the out-of-plane strain components are not defined kinematically (Aravas (1987) and some modifications to the method described in the previous section are needed. In the following paragraphs the cases of linear kinematic hardening and nonlinear kinematic/isotropic hardening are discussed, in terms of the plane stress formulation and numerical integration.

As far as the elastoplastic rigidity tensor $\mathbf{D}^{ep}$ is concerned, in sections 2.1.1 to 2.1.3 this tensor has been calculated for the cases of linear kinematic hardening, nonlinear kinematic hardening and nonlinear kinematic /isotropic (combined) hardening. It has been reported that the rate form of the general elastoplastic equation is written as:

$$\begin{aligned}\dot{\boldsymbol{\sigma}}&=\mathbf{D}^{ep}\dot{\boldsymbol{\varepsilon}}\\ \mathbf{D}^{ep}&=\mathbf{D}-\frac{\mathbf{6}G^2B}{k(\varepsilon_q)}(\boldsymbol{\xi}\otimes\boldsymbol{\xi})\end{aligned} \tag{2.65}$$

where $\mathbf{D}^{ep}$ is the modified rigidity tensor that takes into account the plastic correction of the original rigidity tensor $\mathbf{D}$ and the parameter B varies according to the case examined.

The plane stress formulation of the tangent elastoplastic rigidity tensor $\mathbf{D}^{ep}$ for the cases presented in sections 2.3.1 and 2.3.2 is based on the corresponding

formulation of $\mathbf{D}^{ep}$ for the cases presented in sections 2.1.1 to 2.1.3. In the plane stress formulation the restriction $\sigma_{33}=0$ has to be satisfied also in its rate form:

$$\dot{\sigma}_{33}=0 \tag{2.66}$$

This allows for the decomposition of the stress rate tensor in two parts:

$$\dot{\boldsymbol{\sigma}}=\dot{\overline{\boldsymbol{\sigma}}}+\dot{\sigma}_{33} \tag{2.67}$$

The Eq.(2.65) can be written in the following format:

$$\begin{bmatrix}\dot{\overline{\boldsymbol{\sigma}}}\\ \dot{\sigma}_{33}\end{bmatrix}=\begin{bmatrix}\mathbf{D}_{aa}^{ep} & \mathbf{D}_{a3}^{ep}\\ \mathbf{D}_{3a}^{ep} & D_{33}^{ep}\end{bmatrix}\cdot\begin{bmatrix}\dot{\overline{\boldsymbol{\varepsilon}}}\\ \dot{\varepsilon}_{33}\end{bmatrix} \tag{2.68}$$

and the "Static condensation" rule can be applied. Taking into account Eq.(2.66), it results that:

$$\mathbf{D}_{3a}^{ep}\cdot\dot{\overline{\boldsymbol{\varepsilon}}}+D_{33}^{ep}\cdot\dot{\varepsilon}_{33}=0 \tag{2.69}$$

or equivalently:

$$\dot{\varepsilon}_{33}=-\frac{\mathbf{D}_{3a}^{ep}}{D_{33}^{ep}}\cdot\dot{\overline{\boldsymbol{\varepsilon}}} \tag{2.70}$$

The second valid equation resulting from the "Static condensation" rule is:

$$\dot{\overline{\boldsymbol{\sigma}}}=\mathbf{D}_{aa}^{ep}\cdot\dot{\overline{\boldsymbol{\varepsilon}}}+\mathbf{D}_{a3}^{ep}\cdot\dot{\varepsilon}_{33} \tag{2.71}$$

and by substituting the $\dot{\varepsilon}_{33}$ term from Eq.(2.70) it results that:

$$\dot{\overline{\boldsymbol{\sigma}}}=\left(\mathbf{D}_{aa}^{ep}-\frac{\mathbf{D}_{a3}^{ep}\cdot\mathbf{D}_{3a}^{ep}}{D_{33}^{ep}}\right)\cdot\dot{\overline{\boldsymbol{\varepsilon}}} \tag{2.72}$$

The Eq.(2.72) can now be treated as the rate form of the general elastoplastic equation for the plane stress formulation that takes into account the plastic correction of the rigidity tensor $\mathbf{D}$. Therefore, Eq.(2.72) can be written as:

$$\begin{aligned}&\dot{\overline{\boldsymbol{\sigma}}}=\overline{\mathbf{D}}^{ep}\cdot\dot{\overline{\boldsymbol{\varepsilon}}}\\ &\overline{\mathbf{D}}^{ep}=\left(\mathbf{D}_{aa}^{ep}-\frac{\mathbf{D}_{a3}^{ep}\cdot\mathbf{D}_{3a}^{ep}}{D_{33}^{ep}}\right)\end{aligned} \tag{2.73}$$

Finally, the plane stress formulation of the elastoplastic problem regardless the hardening rule adopted can be summarized in the satisfaction of two main equations. The first equation that has to be satisfied is the von Mises yield criterion. As it will be presented in the following paragraphs, it results that the yield criterion is a function of $\Delta\varepsilon_q$ and $\Delta\varepsilon_{33}$ and it can be written as $F_1(\Delta\varepsilon_q,\Delta\varepsilon_{33})=0$. The second restriction that has to be also valid is that $\sigma_{33}=0$. Again, this equation is a function of $\Delta\varepsilon_q$ and $\Delta\varepsilon_{33}$ and it can be written as $F_2(\Delta\varepsilon_q,\Delta\varepsilon_{33})=0$. These two equations have to be solved simultaneously as a system of equations. The Newton method is commonly used and it is described in detail in the work of Aravas (1987). In the following paragraphs the form of the F_1 and F_2 system equations for the linear kinematic hardening rule and the nonlinear kinematic/isotropic (combined) hardening rule are presented.

2.3.1 Numerical implementation of linear kinematic hardening model in plane stress conditions

In the plane stress formulation of the linear kinematic hardening model, the equations (2.1) to (2.13) that describe the yield criterion, the plastic strain rate, the hardening law, the equivalent plastic strain rate and the rate form of the general elasticity equation are still valid. The modification introduced by the plane stress conditions is described in the following paragraphs.

In the present case, the problem is considered planar on the 1-2 plane in a rectangular coordinate system where the only non vanishing out-of-plane strain increment is $\Delta\varepsilon_{33}$. Then, the total strain increment $\Delta\boldsymbol{\varepsilon}$ can be decomposed in two parts as follows:

$$\Delta\boldsymbol{\varepsilon} = \Delta\bar{\boldsymbol{\varepsilon}} + \Delta\varepsilon_{33}\mathbf{b} \tag{2.74}$$

where $\Delta\bar{\boldsymbol{\varepsilon}}$, $\mathbf{b}$ are defined as:

$$\begin{aligned} \Delta\bar{\boldsymbol{\varepsilon}} &= \Delta\varepsilon_{11}(\mathbf{e}_1 \otimes \mathbf{e}_1) + \Delta\varepsilon_{22}(\mathbf{e}_2 \otimes \mathbf{e}_2) + \Delta\varepsilon_{12}[(\mathbf{e}_1 \otimes \mathbf{e}_2) + (\mathbf{e}_2 \otimes \mathbf{e}_1)] \\ \mathbf{b} &= (\mathbf{e}_3 \otimes \mathbf{e}_3) \end{aligned} \tag{2.75}$$

Therefore Eq.(2.13) can be now written as:

$$\boldsymbol{\sigma}_{n+1} = \boldsymbol{\sigma}_n + \mathbf{D}\Delta\bar{\boldsymbol{\varepsilon}} + \mathbf{D}\Delta\varepsilon_{33}\mathbf{b} - \frac{3G}{k}\Delta\varepsilon_q(\mathbf{s}_{n+1} - \mathbf{a}_{n+1}) \tag{2.76}$$

or equivalently $$\boldsymbol{\sigma}_{n+1} = \bar{\boldsymbol{\sigma}}^e + \mathbf{D}\Delta\varepsilon_{33}\mathbf{b} - \frac{3G}{k}\Delta\varepsilon_q(\mathbf{s}_{n+1} - \mathbf{a}_{n+1})$$

subsequently, $\mathbf{b}$ is decomposed in a hydrostatic and a deviatoric part as follows:

$$\mathbf{b} = \frac{1}{3}b_m\mathbf{I} + \mathbf{b}' \tag{2.77}$$

then the product $\mathbf{Db}$ equals to:

$$\mathbf{Db} = \mathbf{D}\left[\frac{1}{3}b_m\mathbf{I} + \mathbf{b}'\right] \tag{2.78}$$

or $$\mathbf{Db} = Kb_m\mathbf{I} + 2G\mathbf{b}'$$

and Eq.(2.76) can be written as:

$$\boldsymbol{\sigma}_{n+1} = \bar{\boldsymbol{\sigma}}^e + \Delta\varepsilon_{33}\left[Kb_m\mathbf{I} + 2G\mathbf{b}'\right] - \frac{3G}{k}\Delta\varepsilon_q(\mathbf{s}_{n+1} - \mathbf{a}_{n+1}) \tag{2.79}$$

The hydrostatic and the deviatoric parts of Eq.(2.79) are:

$$\begin{aligned} p_{n+1} &= \bar{p}^e - K\Delta\varepsilon_{33} \\ \mathbf{s}_{n+1} &= \bar{\mathbf{s}}^e + 2\Delta\varepsilon_{33}G\mathbf{b}' - \frac{3G}{k}\Delta\varepsilon_q(\mathbf{s}_{n+1} - \mathbf{a}_{n+1}) \end{aligned} \tag{2.80}$$

The linear kinematic hardening rule is described by the following linear expression:

$$\dot{\mathbf{a}} = C\dot{\boldsymbol{\varepsilon}}^p \tag{2.81}$$

where C is the linear kinematic hardening modulus and $\dot{\boldsymbol{\varepsilon}}^p$ is the plastic strain rate. The integration of the hardening rule results in:

$$\mathbf{a}_{n+1} = \mathbf{a}_n + \frac{3C}{2k}\Delta\varepsilon_q(\mathbf{s}_{n+1} - \mathbf{a}_{n+1}) \tag{2.82}$$

From Eq.(2.80) and Eq.(2.82) tensor $\boldsymbol{\xi}$ can be written as follows:

$$\boldsymbol{\xi}_{n+1} = \overline{\mathbf{s}}^{(e)} + 2\Delta\varepsilon_{33}G\mathbf{b}' - \frac{3G}{k}\Delta\varepsilon_q\boldsymbol{\xi}_{n+1} - \left(\mathbf{a}_n + C\frac{3}{2k}\Delta\varepsilon_q\boldsymbol{\xi}_{n+1}\right) \tag{2.83}$$

or equivalently:

$$\begin{aligned} \boldsymbol{\xi}_{n+1} &= \frac{1}{AFACT}\left(\mathbf{s}^{(e)} + 2\Delta\varepsilon_{33}G\mathbf{b}' - \mathbf{a}_n\right) \\ AFACT &= 1 + \frac{3}{k}\left(G + \frac{C}{2}\right)\Delta\varepsilon_q \end{aligned} \tag{2.84}$$

The von Mises yield criterion $F_{n+1} = \frac{1}{2}\boldsymbol{\xi}_{n+1}\cdot\boldsymbol{\xi}_{n+1} - \frac{k^2}{3} = 0$

can be now written at the final state (n+1) as:

$$\begin{aligned} F_{n+1} = {} & \frac{1}{2}\left(\frac{1}{AFACT}\right)^2\left[\overline{\mathbf{s}}^{(e)}\cdot\overline{\mathbf{s}}^{(e)} + 4\Delta\varepsilon_{33}^2G^2\mathbf{b}'\cdot\mathbf{b}' + \mathbf{a}_n\cdot\mathbf{a}_n\right] + \\ & + \frac{1}{2}\left(\frac{1}{AFACT}\right)^2\left[4\Delta\varepsilon_{33}G\overline{\mathbf{s}}^{(e)}\cdot\mathbf{b}' - 2\overline{\mathbf{s}}^{(e)}\cdot\mathbf{a}_n - 4G\Delta\varepsilon_{33}\mathbf{b}'\cdot\mathbf{a}_n\right] - \frac{k^2}{3} = 0 \end{aligned} \tag{2.85}$$

The products $\overline{\mathbf{s}}^{(e)}\cdot\overline{\mathbf{s}}^{(e)}$, $\mathbf{b}'\cdot\mathbf{b}'$, $\overline{\mathbf{s}}^{(e)}\cdot\mathbf{b}'$ and $\mathbf{b}'\cdot\mathbf{a}_n$ can be simplified as follows:

$$\begin{aligned} &\overline{\mathbf{s}}^{(e)}\cdot\overline{\mathbf{s}}^{(e)} = \frac{2}{3}\overline{q}_e{}^2 \\ &\mathbf{b}'\cdot\mathbf{b}' = \frac{2}{3} \\ &\overline{\mathbf{s}}^{(e)}\cdot\mathbf{b}' = \overline{s}_{33}^{(e)} \\ &\mathbf{b}'\cdot\mathbf{a}_n = \mathrm{a}_n^{33} \end{aligned} \tag{2.86}$$

And the von Mises yield criterion can be written as:

$$\begin{aligned} F_{n+1} = {} & \frac{1}{3}\left(\frac{1}{AFACT}\right)^2\left[\overline{q}_e{}^2 + 4\Delta\varepsilon_{33}^2G^2 + \frac{2}{3}\mathbf{a}_n\cdot\mathbf{a}_n\right] + \\ & + \left(\frac{1}{AFACT}\right)^2\left[2\Delta\varepsilon_{33}G\ \overline{s}_{33}^{(e)} - \overline{\mathbf{s}}^{(e)}\cdot\mathbf{a}_n - 2G\Delta\varepsilon_{33}\mathrm{a}_{33n}\right] - \frac{k^2}{3} = 0 \end{aligned} \tag{2.87}$$

The $\Delta\varepsilon_{33}$ increment of strain in the out-of-plane direction should be treated as an extra unknown. For its determination the following constraint at stage (n+1) applies:

$$\begin{aligned} &\sigma_{33,n+1} = 0 \\ &s_{33,n+1} + p_{n+1} = 0 \end{aligned} \tag{2.88}$$

The s_{33} quantity is calculated with the use of Eq.(2.80) and Eq.(2.82) by eliminating the term a_{33n+1}. It can be written as:

$$
\begin{aligned}
s_{33n+1} &= B\left(\bar{s}_{33}^{e} + 2\Delta\varepsilon_{33} G b'_{33} + \frac{3G}{k}\Gamma\Delta\varepsilon_q a_{33n} \right) \\
\Gamma &= \frac{1}{1+\dfrac{3C}{2k}\Delta\varepsilon_q} \\
B &= \frac{1}{1+\dfrac{3G}{k}\Delta\varepsilon_q\left(1+\dfrac{3C\Gamma}{2k}\right)}
\end{aligned}
\tag{2.89}
$$

By taking into consideration Eq.(2.80), the final form of Eq.(2.89) is written as:

$$
B\left(\bar{s}_{33}^{e} + \frac{4}{3}\Delta\varepsilon_{33} G b'_{33} + \frac{3G}{k}\Gamma\Delta\varepsilon_q a_{33n} \right) + \bar{p}^{e} - K\Delta\varepsilon_{33} = 0 \tag{2.90}
$$

Equations (2.87) and (2.90) are solved simultaneously as a system with the unknowns being the quantities $\Delta\varepsilon_q$ and $\Delta\varepsilon_{33}$.

2.3.2 The nonlinear kinematic/isotropic (combined) hardening model

As it has been discussed in paragraph 2.1.3, in the most general formulation of the Armstrong – Frederick model the size of the yield surface is no longer a constant, but it is allowed to change depending on the amount of the equivalent plastic strain. The equation modifications due to the plane-stress formulation are presented in this paragraph. For simplicity, only the nonlinear kinematic/isotropic (combined) hardening model equations will be presented. The nonlinear kinematic hardening model equations can be easily derived by assuming that the size of the yield surface is constant. The presented model can also reduce to the simple linear kinematic hardening formulation by using the linear form of the hardening rule and also assuming a constant size of the yield surface, as it has been presented in the previous paragraph.

The nonlinear kinematic hardening rule is described Eq. (2.17) and its integration is given by Eq.(2.54). The integrated form of the general elasticity equation can be now written as:

$$
\begin{aligned}
\boldsymbol{\sigma}_{n+1} &= \boldsymbol{\sigma}_n + \mathbf{D}\Delta\bar{\boldsymbol{\varepsilon}} + \mathbf{D}\left(\Delta\varepsilon_{33}\mathbf{b}\right) - \frac{3G}{k(\varepsilon_{qn+1})}\Delta\varepsilon_q(\mathbf{s}_{n+1} - \mathbf{a}_{n+1}) \\
\boldsymbol{\sigma}_{n+1} &= \bar{\boldsymbol{\sigma}}^{e} + \mathbf{D}\left(\Delta\varepsilon_{33}\mathbf{b}\right) - \frac{3G}{k(\varepsilon_{qn+1})}\Delta\varepsilon_q(\mathbf{s}_{n+1} - \mathbf{a}_{n+1})
\end{aligned}
\tag{2.91}
$$

and by using the decomposition of $\mathbf{b}$ described in Eq.(2.77), the hydrostatic and the deviatoric parts of Eq.(2.91) are:

$$
\begin{aligned}
p_{n+1} &= \bar{p}^{e} - K\Delta\varepsilon_{33} \\
\mathbf{s}_{n+1} &= \bar{\mathbf{s}}^{e} + 2\Delta\varepsilon_{33} G\mathbf{b}' - \frac{3G}{k(\varepsilon_{qn+1})}\Delta\varepsilon_q(\mathbf{s}_{n+1} - \mathbf{a}_{n+1})
\end{aligned}
\tag{2.92}
$$

From Eq.(2.92) and Eq.(2.54) tensor $\boldsymbol{\xi}$ can now be written as:

$$\boldsymbol{\xi}_{n+1} = \overline{\mathbf{s}}^{(e)} + 2\Delta\varepsilon_{33} G\mathbf{b}' - \frac{3G}{k(\varepsilon_{qn+1})}\Delta\varepsilon_q \boldsymbol{\xi}_{n+1} - \frac{1}{1+\gamma\Delta\varepsilon_q}\left(\mathbf{a}_n + C\frac{3}{2k(\varepsilon_{qn+1})}\Delta\varepsilon_q \boldsymbol{\xi}_{n+1}\right) \tag{2.93}$$

or equivalently:

$$\boldsymbol{\xi}_{n+1} = \frac{1}{AFACT}\left(\mathbf{s}^{(e)} + 2\Delta\varepsilon_{33} G\mathbf{b}' - \frac{1}{1+\gamma\Delta\varepsilon_q}\mathbf{a}_n\right)$$
$$AFACT = 1 + \frac{3}{k(\varepsilon_{qn+1})}\left(G + \frac{C}{2(1+\gamma\Delta\varepsilon_q)}\right)\Delta\varepsilon_q \tag{2.94}$$

The von Mises yield criterion defined in Eq.(2.1) can be now written at the final state (n+1) as:

$$F_{n+1} = \frac{1}{2}\left(\frac{1}{AFACT}\right)^2\left[\overline{\mathbf{s}}^{(e)}\cdot\overline{\mathbf{s}}^{(e)} + 4\Delta\varepsilon_{33}^2 G^2\mathbf{b}'\cdot\mathbf{b}' + \left(\frac{1}{1+\gamma\Delta\varepsilon_q}\right)^2\mathbf{a}_n\cdot\mathbf{a}_n\right] + \frac{1}{2}\left(\frac{1}{AFACT}\right)^2\left[4\Delta\varepsilon_{33}G\overline{\mathbf{s}}^{(e)}\cdot\mathbf{b}' - \frac{2}{1+\gamma\Delta\varepsilon_q}\overline{\mathbf{s}}^{(e)}\cdot\mathbf{a}_n - \frac{4G\Delta\varepsilon_{33}}{1+\gamma\Delta\varepsilon_q}\mathbf{b}'\cdot\mathbf{a}_n\right] - \frac{k^2}{3} = 0 \tag{2.95}$$

The simplification of the products described in Eq. (2.86) can be used and the von Mises yield criterion can be written as:

$$F_{n+1} = \frac{1}{3}\left(\frac{1}{AFACT}\right)^2\left[\overline{q}_e{}^2 + 4\Delta\varepsilon_{33}^2 G^2 + \frac{2}{3}\left(\frac{1}{1+\gamma\Delta\varepsilon_q}\right)^2\mathbf{a}_n\cdot\mathbf{a}_n\right] + \left(\frac{1}{AFACT}\right)^2\left[2\Delta\varepsilon_{33}G\ \overline{s}_{33}^{(e)} - \frac{\overline{\mathbf{s}}^{(e)}\cdot\mathbf{a}_n}{1+\gamma\Delta\varepsilon_q} - \frac{2G\Delta\varepsilon_{33}}{1+\gamma\Delta\varepsilon_q}\mathrm{a}_{33n}\right] - \frac{k^2}{3} = 0 \tag{2.96}$$

Using the constraints described in Eq. (2.88) for $\Delta\varepsilon_{33}$, the s_{33} quantity is calculated with the use of Eq.(2.80) and Eq.(2.82) by eliminating the term a_{33n+1}. It can be written as:

$$s_{33n+1} = B\left(\overline{s}_{33}^{e} + 2\Delta\varepsilon_{33}Gb'_{33} + \frac{3G}{k(\varepsilon_{qn+1})}\Gamma\Delta\varepsilon_q \mathrm{a}_{33n}\right)$$
$$\Gamma = \frac{1}{1+\frac{3C}{2(1+\gamma\Delta\varepsilon_q)k(\varepsilon_{qn+1})}\Delta\varepsilon_q} \tag{2.97}$$
$$B = \frac{1}{1+\frac{3G}{k(\varepsilon_{qn+1})}\Delta\varepsilon_q\left(1+\frac{3C\Gamma}{2(1+\gamma\Delta\varepsilon_q)k(\varepsilon_{qn+1})}\right)}$$

Taking into consideration Eq.(2.80), the final form of Eq.(2.89) is written as:

$$B\left(\overline{s}_{33}^{e} + \frac{4}{3}\Delta\varepsilon_{33}G + \frac{3G}{k(\varepsilon_{qn+1})}\frac{\Gamma}{1+\gamma\Delta\varepsilon_q}\Delta\varepsilon_q \mathrm{a}_{33n} \right) + \overline{p}^{e} - K\Delta\varepsilon_{33} = 0 \qquad (2.98)$$

Equations (2.96) and (2.98) are solved simultaneously as a system with the unknowns being the quantities $\Delta\varepsilon_q$ and $\Delta\varepsilon_{33}$.

2.4 Implementation of the nonlinear kinematic/isotropic (combined) hardening model and comparison with ABAQUS

The nonlinear kinematic/isotropic (combined) hardening model described in the previous paragraphs of the present chapter has been implemented and incorporated in an in-house finite element code written in FORTRAN programming language in a user subroutine. The implementation is based on two-dimensional (plane-strain) elastoplasticity formulation. The user subroutine is presented in detail at the end of this paragraph.

The same plasticity model is already included in the general-purpose commercial finite element code ABAQUS. In ABAQUS, the isotropic hardening part of the model can be defined in many different ways. If the "cyclic hardening – parameters" sub option is used for the description of the plastic part of the model, the following equation for the size of the yield surface is adopted:

$$k(\varepsilon_q) = k_o + Q_\infty(1 - e^{-b\varepsilon_q}) \qquad (2.99)$$

where k_o is the yield stress at zero plastic strain and Q_∞ and b are material parameters. Q_∞ is the maximum change in the size of the yield surface, and b defines the rate at which the size of the yield surface changes as plastic straining develops. Instead, for large valued of the equivalent plastic strain ε_q $(\varepsilon_q \to \infty)$, the size of the yield surface is stabilized at the value of $k_o + Q_\infty$. The parameter Q_∞ may also take negative values.

When the equivalent stress defining the size of the yield surface remains constant $\left(k(\varepsilon_q) = k_o\right)$, the model reduces to the more standard version of nonlinear kinematic hardening model.

2.4.1 Presentation of the developed subroutine

In the in-house finite element code "NONSA1" used for the implementation of the nonlinear kinematic/isotropic (combined) hardening model, the material model is implemented though the user-defined "Subroutine SS". In this part of the code, the stress calculation as well as the calculation of the rigidity tensor components is performed at every loading increment at each integration point. The subroutine is based on the "elastic predictor – plastic corrector" scheme as described in previous paragraphs. The necessary Newton Raphson iterations for the solution of the nonlinear algebraic equations are conducted in another subroutine named "Subroutine NR", which is called by "Subroutine SS". Finally, the equation that describes the size of the yield surface and its derivative with respect to the

equivalent plastic strain is defined through “Function ASIZE(X)” and “Function DSIZE(X)” respectively. All the above parts of the in-house code are quoted at the end of this paragraph.

The material parameters which are necessary for the implementation of the model are the Young modulus E, the Poison ratio ν, the initial size of the yield surface k_o and the cinematic hardening parameters $C,\ \gamma$. These values are inserted to the code though an input file where the geometry of the problem (nodal coordinates and connectivity) and the loading history are also specified. The description of the change of size of the yield surface function and the parameters used are described by the corresponding functions.

The nonlinear kinematic/isotropic (combined) hardening model reduces to the nonlinear kinematic hardening model excluding the isotropic hardening part. Moreover, it yields the simple linear kinematic hardening rule by setting the γ value equal to zero. Setting both parameters $C,\ \gamma$ equal to zero but allowing for change of the size of the yield surface in terms of the equivalent plastic strain, the model reduces to the classical isotropic hardening model.

2.4.2 Verification of the user-subroutine

For the verification of the developed subroutine, the same uniaxial one-element example problem is simulated in both ABAQUS and the in-house code. For this simulation the 8-noded isoparametric plane-strain quadrilateral, reduced-integration element is used in both codes (in ABAQUS it is denoted as CPE8R element). The problem is imposed as load-controlled and the cyclic loading applied has the following characteristics:

$$\sigma_{\max} = 660\ MPa \quad \sigma_m = 240\ MPa,$$
$$\sigma_{\min} = \text{-}180\ MPa \quad \Delta\sigma = 420\ MPa$$

The values of material hardening parameter are chosen as follows:

$$C = 15000,\ \gamma = 15,\ Q_\infty = 200,\ b = 10$$

The comparison of the results from the in-house code and the ABAQUS code is very good as shown in Fig.(2.1). The minor differences that appear are attributed to issues of numerical accuracy. As described in the previous paragraph, the in-house code can be also used as nonlinear kinematic hardening model, as a simple kinematic hardening model or even as an isotropic hardening model through the proper choice of the parameter values. For verification reasons, the same problem described above has been simulated using all the possible model modifications. The results are very satisfactory. In the following graph only the simulation results of the combined hardening are shown. For this case the maximum difference is at the range of 0.8% which is considered to be very satisfactory.

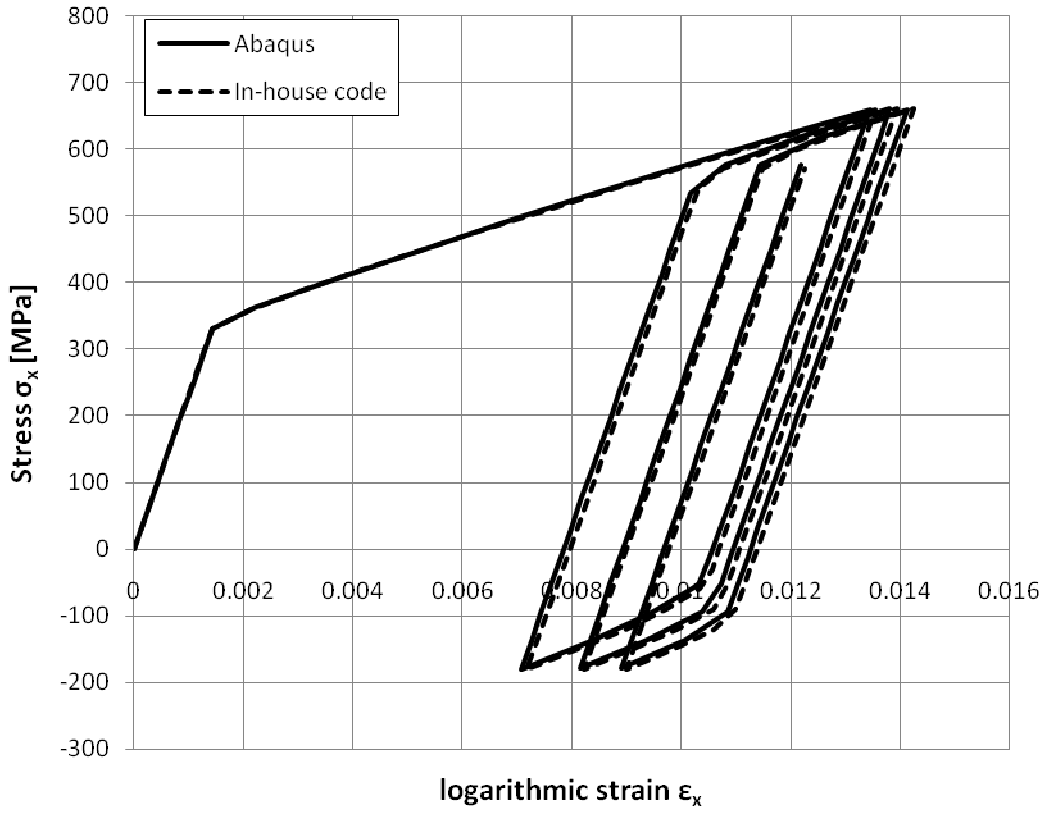

Fig. (2.1) Cyclic loading history predicted by the in-house code and ABAQUS.

2.4.3 The predicted material behavior

The nonlinear kinematic/isotropic (combined) hardening model ability to predict cyclic plasticity related phenomena is examined through one-element uniaxial numerical tests. Special focus is given in the prediction of the phenomena discussed in Chapter 1 such as the Bauschinger effect, cyclic hardening/softening and ratcheting (cyclic creep).

The Bauschinger effect is taken into consideration by the linear kinematic hardening rule in very approximate manner. In that model, due to the constant size of the yield surface assumption, when loading is followed by reverse loading, the material plastisfication begins when the distance covered in the stress space is twice the size of the yield surface $(2k_o)$ which reduces the accuracy of the simulation. Moreover, the gradual change of the plastic modulus is not captured by this model. When the nonlinear kinematic hardening model is used and nonzero values for the parameter γ are adopted, the shape of the stress-strain curve is improved. Such an example is illustrated in Fig. (2.2). The values of nonlinear kinematic hardening material parameter are chosen as follows:

$$C = 47000,\ \gamma = 500$$

The hardening modulus adopted for the kinematic hardening rule is kept the same.

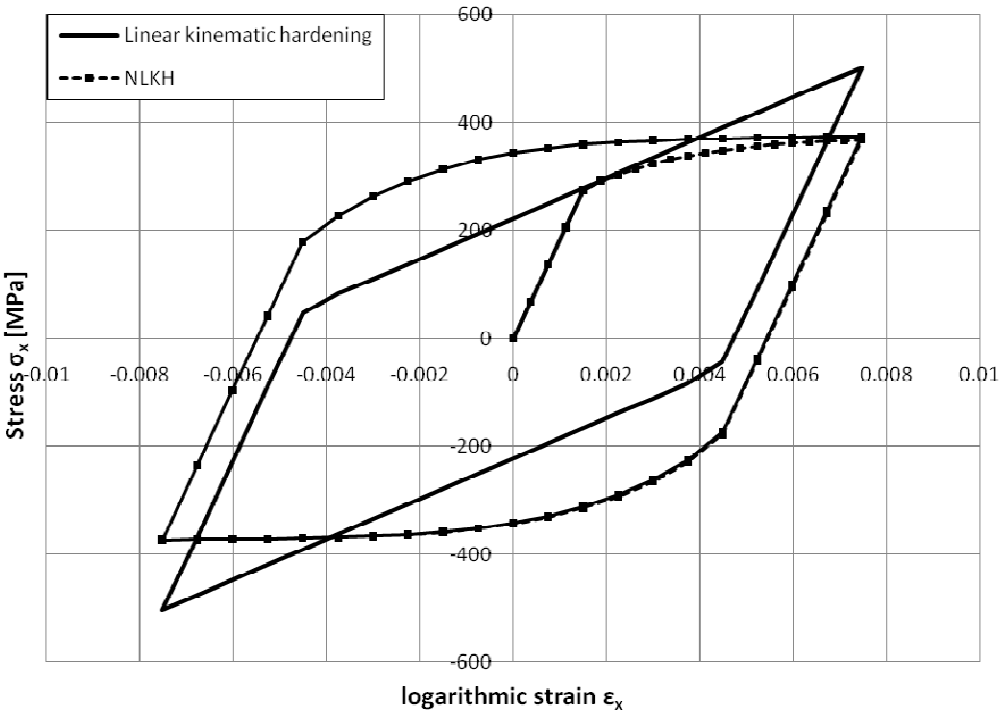

Fig. (2.2) Cyclic loading using the linear and nonlinear kinematic hardening rule.

The cyclic hardening/softening of the materials is modeled through the isotropic part of the combined hardening model. In the present formulation, Eq. (2.99) is employed for the isotropic hardening description. After a few load reversals, the hardening/softening effect extinguishes and the material reaches a stabilized hysteresis loop. Note that in Eq.(2.99) parameters Q_∞ and b have a strong influence on the material behavior. In particular, the parameter Q_∞ defines if the material hardens or softens after repeated load cycles. For positive values of Q_∞ the material exhibits strain hardening, while for negative values of Q_∞ the material exhibits strain softening. The parameter b affects the rate at which the material reaches the stable state; the higher the value of b , the faster the material behavior is stabilized.

The effect these parameters on the shape of the hysteresis loop is shown in Fig.(2.3)(a) and (b). In Fig.(2.3)(a) the effect of the isotropic part of the hardening rule is examined. The numerical predictions of the nonlinear kinematic hardening rule are compared with those of the nonlinear kinematic/isotropic hardening rule with negative and positive values of the parameter Q_∞ , which implies that cyclic softening behavior and cyclic hardening behavior is assumed respectively. In Fig.(2.3) (b) the rate at which cyclic hardening takes place is examined. In particular this rate is influenced by the value of the parameter b . The different value of the parameter b leads to different number of cycles until stabilization of the material. Both simulations adopt the same positive value of Q_∞ .

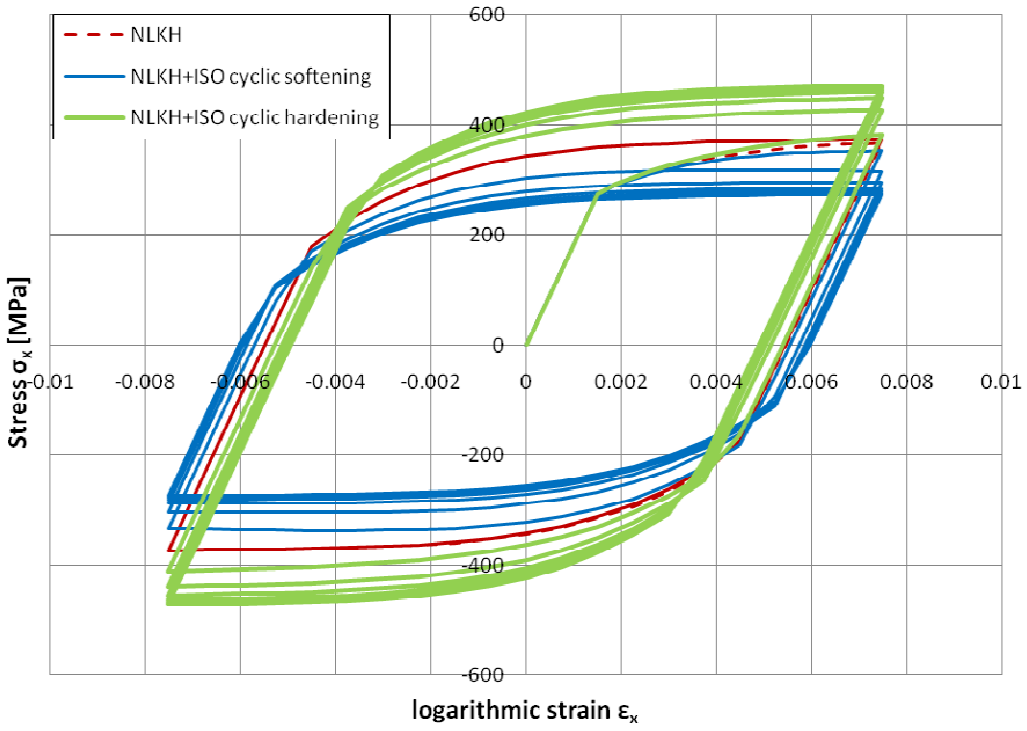

(a)

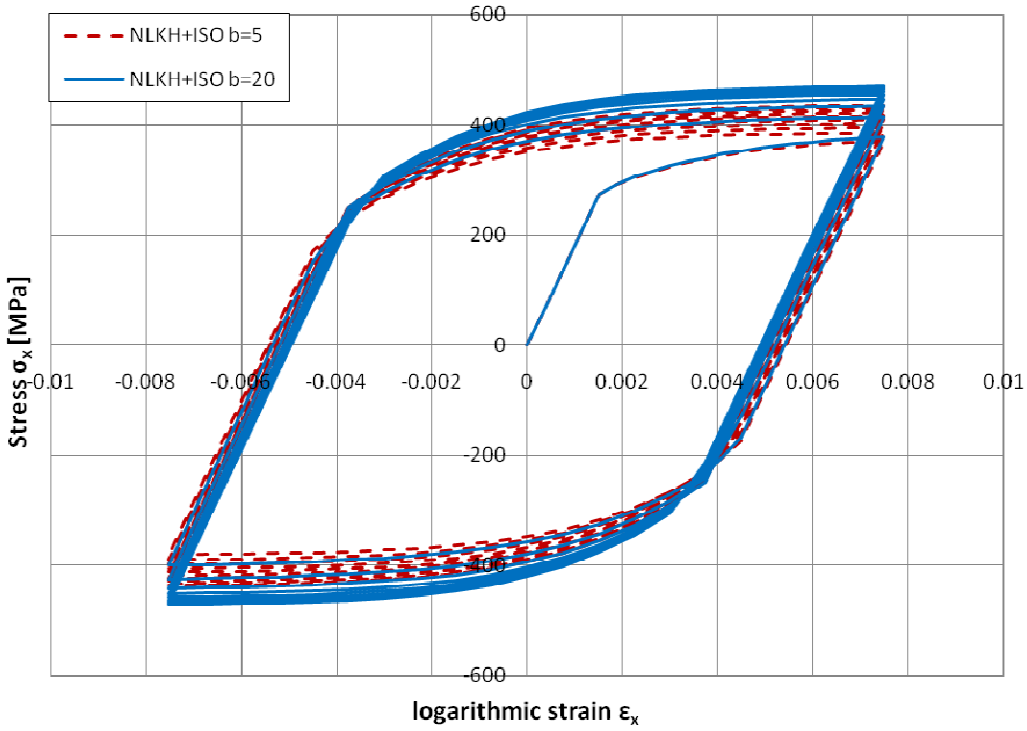

(b)

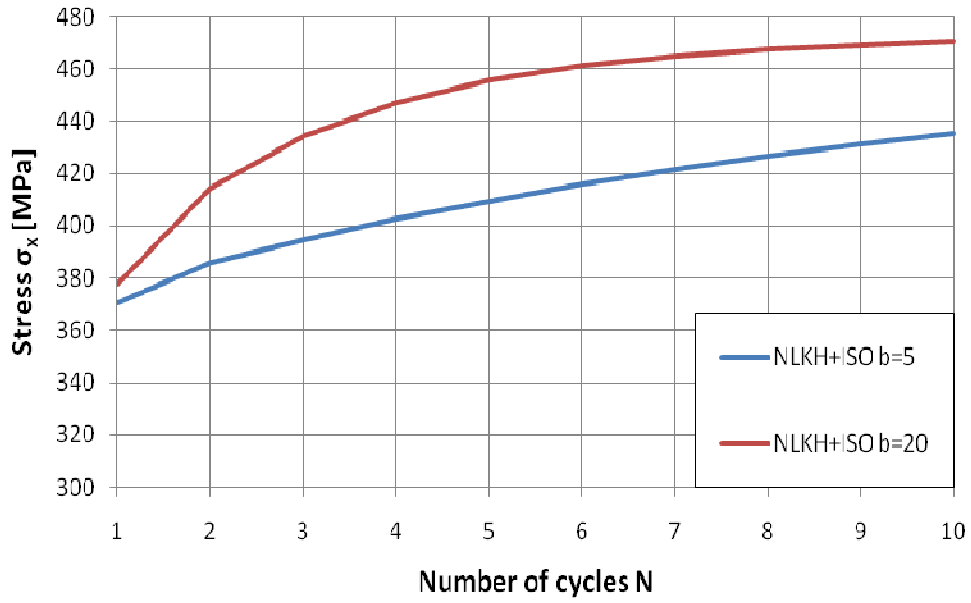

(c)

Fig. (2.3) The effect of the parameters Q_∞ and b on the hysteresis loop.
(a) Cyclic hardening/softening of the material, (b) Different rate of cyclic hardening,
(c) The effect of the parameter b on the rate of cyclic hardening.

When cyclic loading contains unsymmetrical stress-controlled cycles in the plastic regime, then ratcheting takes place in the direction of the mean stress. It is observed that the rate of ratcheting depends on the level of the mean stress. For low mean stress levels, the initial transient phase of ratcheting is followed by zero ratcheting rate indicating a stabilization of the material behavior. On the contrary, for high levels of mean stress, the ratcheting rate is kept constant as the number of cycles increases. The linear kinematic hardening predicts zero ratcheting. The resulting stress-strain curve is a closed loop. The nonlinear kinematic hardening rule (no isotropic hardening) predicts constant rate of ratcheting regardless the magnitude of the mean stress. The nonlinear combined hardening model (that contains an isotropic hardening part) predicts an initial ratchet rate which is gradually reduced until it becomes constant. At this point the change of size of the yield surface is completed and the material is stabilized. The predicted behavior of these models is depicted in Fig. (2.4).

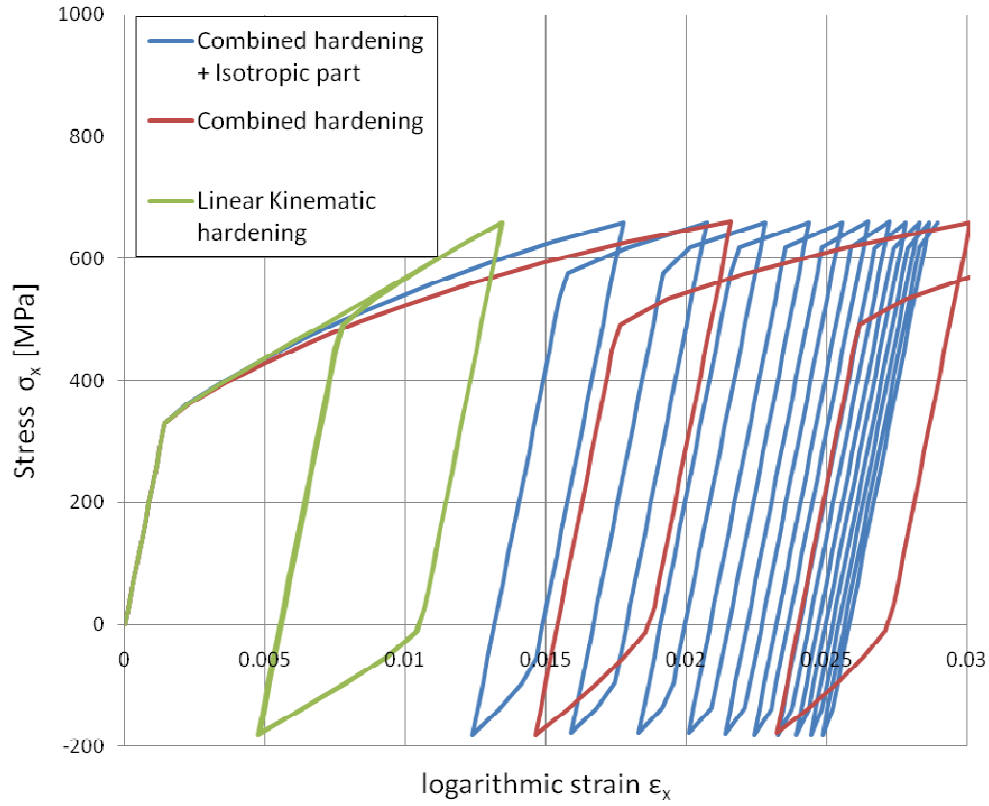

(a)

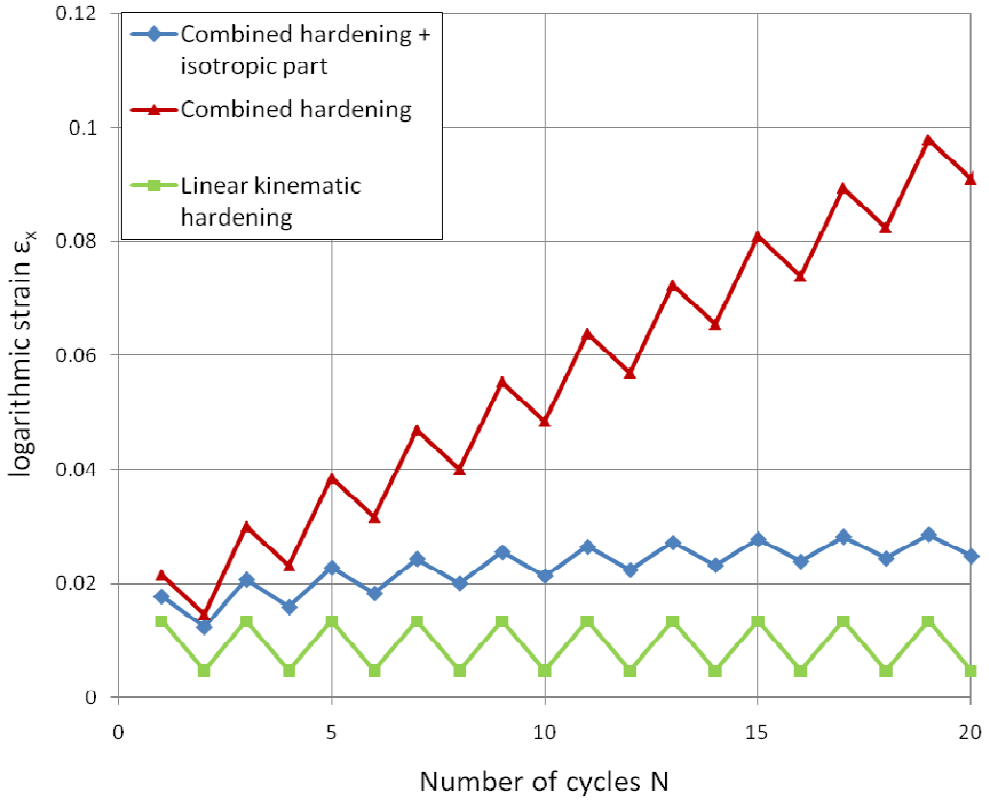

(b)

Fig. (2.4) Ratcheting simulation results: (a) Loading cycles, (b) ratcheting rate

3 Tubular members under cyclic loading

3.1 Introduction

Tubular members or pipes are widely used in structural or mechanical engineering applications. Nowadays they are produced in a wide variety of diameter sizes and wall thicknesses. From the engineering point of view, tubular elements are beneficial as they have the material symmetrically distributed around the cross-section. This fact results to the same inertial characteristics regardless the direction of the bending loading applied. They are also preferred over other typical steel cross sections due to their aesthetics.

In the structural engineering field, tubular members are often used as columns or parts of bracing systems in many important types of structures such as medium or high rise buildings. They are also employed in the construction of off-shore platforms, bridges, latticed (trussed) structures, cranes and towers.

In the mechanical engineering field tubular members are commonly used as onshore or offshore pipes that transfer liquids or gasses. Their shape provides an advanced pressure resistance and therefore they are able to operate in significant pressure levels. They are employed for transmission or distribution pipelines for oil, gas and water, as well as for industrial piping. As a consequence, these pipes are subjected to a combination of bending loading and internal or external pressure.

In most of the cases described above, the applied loading has a cyclic character which stems from variations of the prescribed operational loads of the structure. In addition, accidental actions such as strong earthquakes or intense wind loading generate cyclic actions beyond the elastic range. For the special case of offshore structures and undersea pipes, wave-induced loading constitutes one of the main types of strong cyclic loading which is directly related to low cycle fatigue failures.

Bending behavior of tubular members has some particularities that make this problem more demanding from the bending problem of members from other structural sections (e.g. I-beams). When tubular members or pipe components are subjected to bending loading, the circular cross-section distorts in the form of an oval shape, leading to a reduction of the plastic moment capacity. Furthermore, the development of compressive stresses at the compression zone of the cylinder may cause wrinkling of the cylinder wall, leading to buckling in the form of a localized buckling pattern. The work of Brazier (1927) was the first to relate the bending behavior of a thin-walled cylinder to the ovalization of its cross-section. Brazier, assuming elastic behavior of the cylinder material, obtained closed-formed expressions for the moment-curvature and the ovalization-curvature relations. His results were confirmed by more accurate semi-analytical solutions of the ovalization problem in elastic cylinders (Axelrad (1962), Reissner & Weinitschke (1963)), as well as by more rigorous numerical simulations (Levyakov (2001), Karamanos (2002)).

Nevertheless, tubes used in the vast majority of engineering applications fail in the plastic regime, after exhibiting significant inelastic deformation. Ades (1957) examined the same problem in the inelastic range, using the simplifying assumption that the cylinder ovalizes to an elliptical shape. The problem was revisited by Gellin

(1980), using a numerical formulation. Kyriakides and Shaw (1982), and Corona & Kyriakides (1988) presented extensive experimental results on this problem, supported by simplified numerical analyses. A more rigorous investigation of hollow cylinder ovalization under monotonic bending was presented by Karamanos & Tassoulas (1991), using a nonlinear elasto-plastic finite element procedure.

Figures 3.1 and 3.2 show the response of metal tubular members under monotonic bending loading conditions. Figure 3.1 shows the moment-curvature diagram of the tube, obtained experimentally by Kyriakides & Ju (1992). The equilibrium path is nonlinear, due to the combined effect of plastic deformation and cross-section ovalization. The results indicate that upon reaching a limit (ultimate moment) the moment capacity drops very rapidly. This sudden drop may occur immediately after a maximum moment is reached (in the case of thin-walled cylinders), or after the member exhibits a certain plastic plateau (in the case of relatively-thick-walled cylinders). In both cases, failure is in the form of localized buckling, as shown in Figures 3.2(a) and 3.2(b).

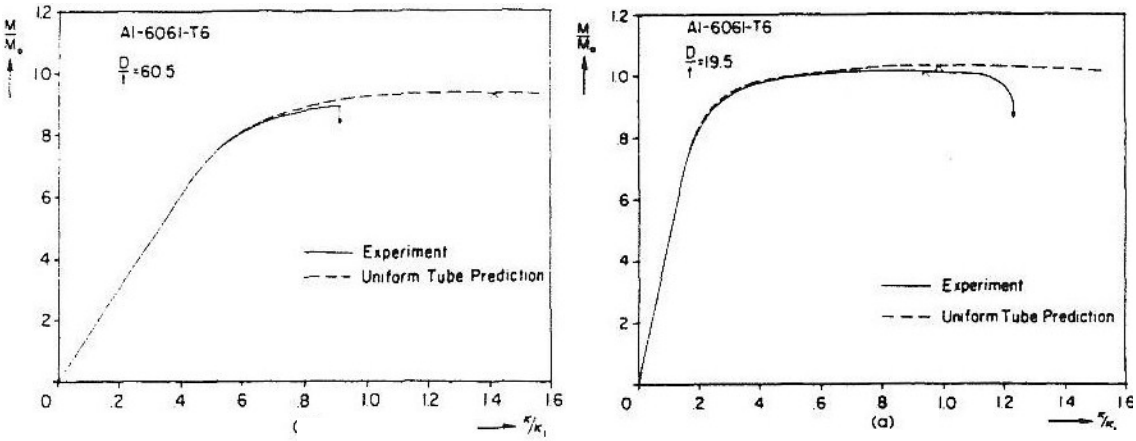

Figure 3.1: Bending response of aluminum shell with D/t=60.5 and D/t=19.5: Moment-curvature (Kyriakides & Ju, 1992)

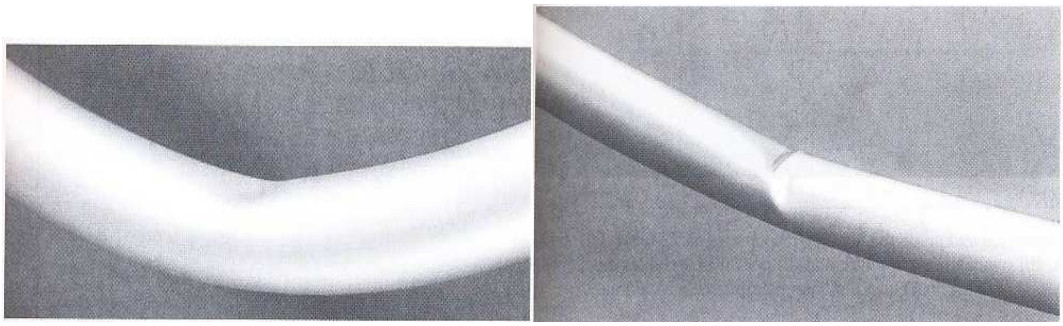

(a) (b)

Figure 3.2: Examples of collapse modes under pure bending: (a) diffuse local collapse characteristic of tubes with low D/t values (b) diamond-mode for tubes with high D/t values [Kyriakides & Corona (2007)]

The response of tubular members under repeated (cyclic) loading has been examined experimentally by Toma & Chen (1982, 1983), Popov et al. (1979) and Zayas et al. (1982), motivated by the necessity of determining failure limits of tubular lattice structures under strong earthquake loading. Furthermore, motivated by the structural response of offshore pipelines and risers, Shaw & Kyriakides (1982, 1985) and Corona & Kyriakides (1991) presented experimental results for cyclic bending of tubular members, demonstrating that in every cycle, plastic strain and ovalization is accumulated, as shown in Figure 3.3, resulting in tube failure. Similar experimental results have been presented by Pan & Lee (2002) and Chang, Pan & Lee (2008) where the effect of the mean curvature and mean moment effects in cyclic inelastic bending are discussed.

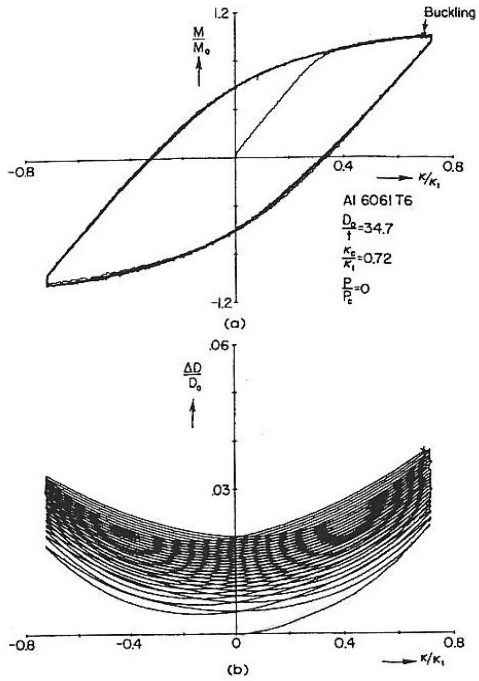

Figure 3.3: Response of an Al-6061-T6 tube to curvature-symmetric cyclic bending.
(a) Moment-curvature, (b) ovalization-curvature [Corona & Kyriakides (1991)]

The simulation accuracy of a tubular element behavior under cyclic bending or under cyclic bending in the presence of internal/external pressure depends highly on the constitutive model used for simulating material behavior. Rahman et al (2008) presented a thorough evaluation of certain cyclic plasticity models capabilities to simulate the ratcheting phenomenon. In this work all the examined models share the same basic characteristics as the nonlinear kinematic/isotropic (combined) hardening model presented in Chapter 2 of the present study. They are all based on the Armstrong – Frederick nonlinear kinematic hardening rule and its enhancements as proposed by Chaboche (1979, 1986), Guionnet (1991), Ohno and Wang (1993) and others. Rahman et al (2008) work will be discussed in detail in a following paragraph. Before proceeding to the examination of the work of Rahman et al (2008), it is considered helpful to examine the behavior of a tube element under pure cyclic bending and under pure cyclic bending combined with axial force.

3.2 Tubular members subjected to cyclic bending and constant internal/external pressure

The effect of the application of cyclic bending in the presence of internal or external pressure is examined in the present paragraph. This loading condition is very common in piping components and pipelines. The accumulation of plastic strain, referred to as ratcheting of the pipe material (as a result of cyclic loading), is investigated in terms of its influence the general bending behavior of the pipe. The cases of internal and external pressure are examined separately in the following paragraphs.

3.2.1 Tubular members subjected to cyclic bending and steady internal pressure.

The ratcheting failure mechanism of pipes subjected to internal pressure and cyclic bending has been investigated by Rahman et al. (2008). In this study, the performance of seven plasticity models has been examined. The plasticity models have been implemented into ANSYS finite element code and their predictions are compared with experimental results provided by a cyclic bending device originally developed by Kyriakides and his coworkers [Kyriakides and Shaw (1987), Corona and Kyriakides (1991)]. The comparison has shown that none of the examined model was robust enough to simulate accurately all the measured parameters.

The prediction capabilities of the Armstrong – Frederick nonlinear kinematic/isotropic hardening rule are examined in the present paragraph. The problem examined by Rahman et al. is simulated in ABAQUS, where the Armstrong – Frederick plasticity model is already implemented. For this purpose, a “slice” finite element model using shell elements has been developed in ABAQUS FE software. The outer diameter of the pipe is 31.85 mm and the wall thickness is 0.911 mm. This implies a diameter-to-thickness ratio (D/t) of 34.96 and it is considered as moderately thick pipe (Fig.3.4). In order to minimize the size of the model and the computational cost, the symmetry of the cross-section was taken into consideration through the appropriate boundary conditions and only the half pipe section was modeled. The length of the created model in the longitudinal direction is equal to 1 mm. The applied bending loading is introduced through a reference point located at the center of the pipe and connected with all the circumferential nodes through a “kinematic coupling” bond.

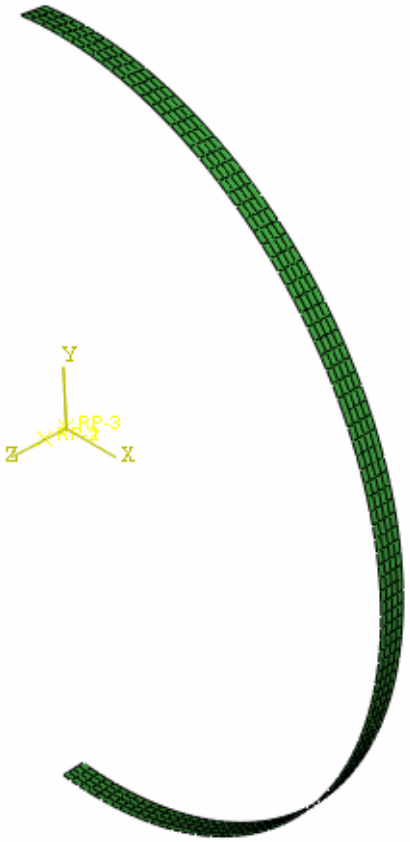

Figure 3.4: FE “slice” model in ABAQUS for ovalization analysis.

Additionally, for the simulation of the experiment conducted by Rahman et al (2008) a 3D shell finite element model was created in ABAQUS general purpose software. Taking advantage of the symmetry of the problem only the one quarter of the pipe cross section was modeled and the appropriate symmetry boundary conditions were applied. The model is presented in Fig. 3.5. A similar model was developed in ANSYS software by Rahman et al (2008). The geometry and mesh of the test specimen is similar to the one considered by Rahman et al. (2008) for direct comparison of the resulting behavior.

At the right end of the model where the symmetry condition is applied, the boundary conditions introduced are similar to those used in the “slice” model. On the contrary, at the left end of the model the adopted conditions are now changed. At the same position of the actual experimental setup the applied end rotation is introduced with the use of a solid end plug as shown in Fig. 3.9. This plug is inserted into the pipe for four inches and it is sealed by welding on the pipe. This interaction is introduced in to the FE model with the use of “cap-type” formulation. This end condition results to an extensive accumulation of plastic strain near the pipe end and consequently leads to failure of the pipe at this area after a number of cycles. Similar failures due to caped pipe ends are also reported in an extensive experimental work conducted by Slagis (1997). Rahman et al. do not report any failure of this kind in their work though.

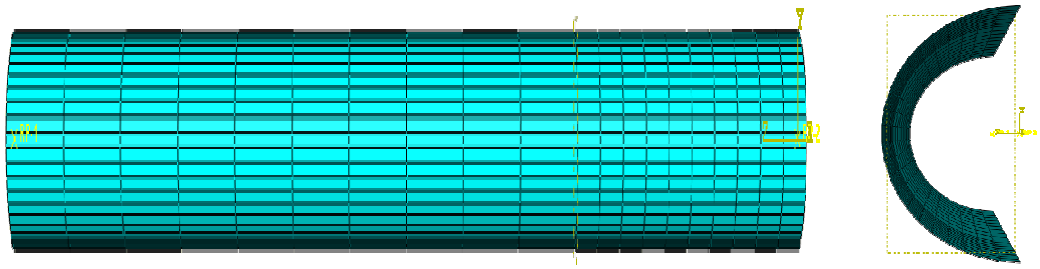

Figure 3.5: The present model in ABAQUS.

The material used for this pipe is steel alloy 4130. The material behavior under cyclic strain-controlled was tested and reported by Rahman et al (2008). The simulation of the material behavior is conducted through one-element test in ABAQUS software using the linear kinematic hardening rule, the nonlinear kinematic hardening rule and the nonlinear kinematic/isotropic hardening rule. The experimental stabilized cyclic stress-strain curve of steel alloy 4130 is shown in Fig. 3.6 along with the predictions of the three kinematic hardening rules.

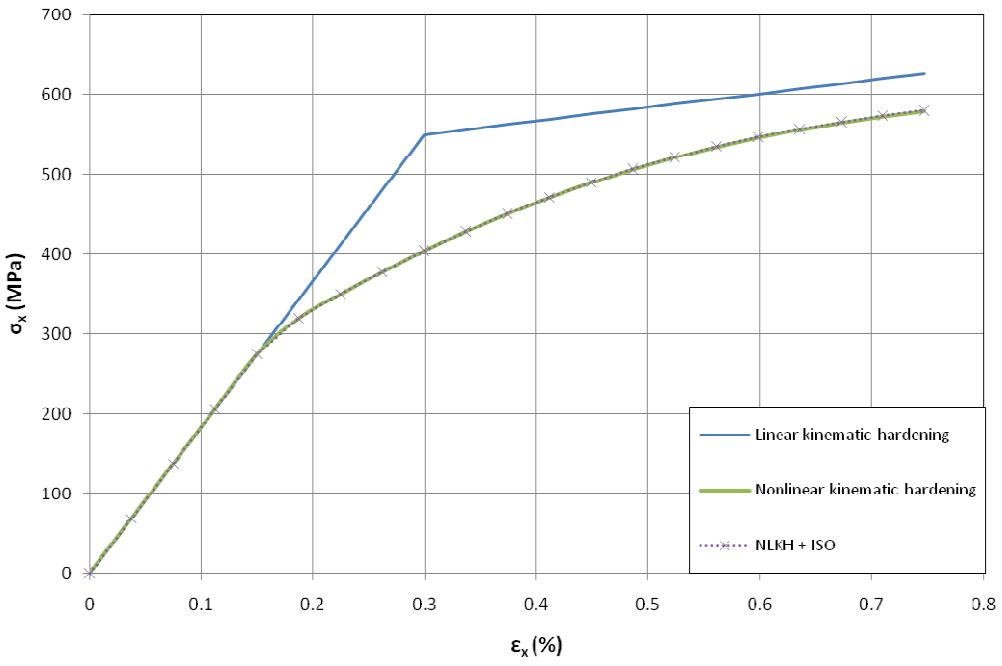

(a)

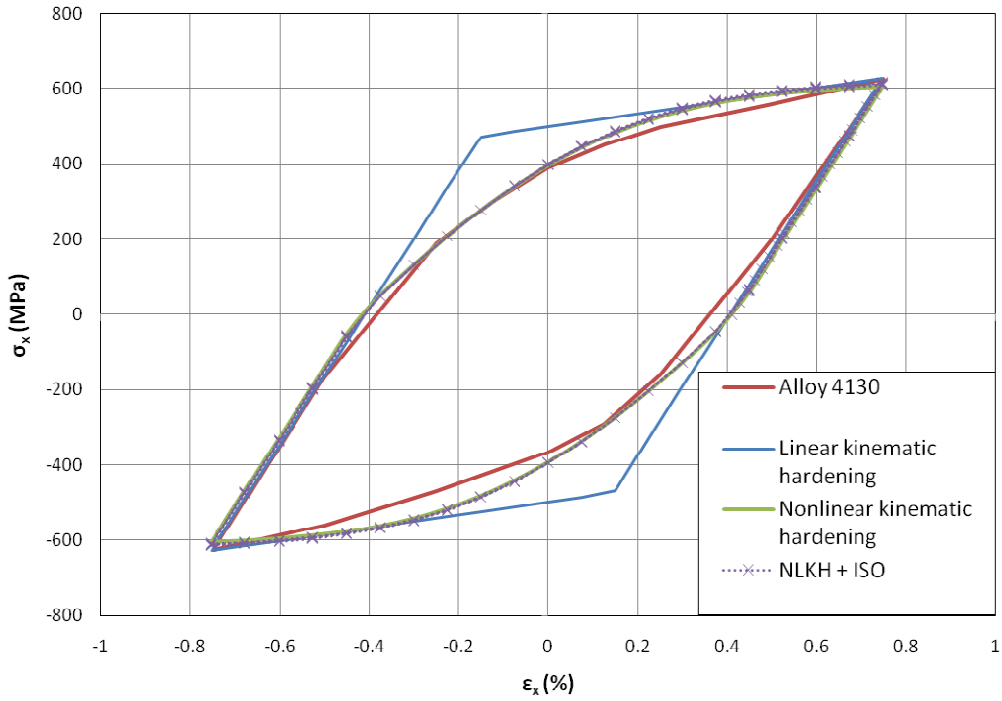

(b)

Figure 3.6: Simulation of the material behavior. (a) Monotonic stress-strain curve (b) Stable cyclic stress-strain hysteresis loop.

The material parameters of the aforementioned hardening rules were properly calibrated to fit the experimental stress-strain curve. The different hardening rules using the parameters reported in Table 3.1 predict different monotonic and cyclic material behavior as shown in Fig.3.6(a) and (b). The resulting material parameters are presented in the following table.

	Linear kinematic	NLKH	NLKH+ISO	NLKH+ISOmod
k (MPa)	550	300	300	280
C (MPa)	18620	160000	160000	47000
γ	0	510	510	1
Q_∞ (MPa)	0	0	20	-20
b	0	0	10	30

Table 3.1. : Material parameters used for the numerical simulation

After the material parameter calibration, the pipe was first subjected to monotonic bending in order to evaluate its ultimate bending capacity using initially the “slice model”. The cross-sectional ovalization is a key parameter for predicting of the bending behavior of the tube. Along with the bending moment-curvature of the pipe, the resulting pipe ovalization was also monitored using three different hardening rules. The resulting ovalization is defined as:

$$\zeta = \frac{D_2 - D_1}{2D} \tag{3.1}$$

where D_1 is the diameter measurement normal to the plane of bending, D_2 is the diameter measurement on the plane of bending and D is the initial diameter of the pipe. The curvature is normalized by the value $k_N = t / D^2$. The results of this analysis are shown in Fig. 3.7. The observed difference in the behavior of the pipe when the nonlinear kinematic hardening rule is adopted are attributed to the different size of the yield surface and the different hardening modulus considered, as described in Table 3.1. When the NLKH/NLKH+ISO parameter sets are adopted, the pipe enters earlier in the plastic range and therefore it exhibits a reduced bending capacity.

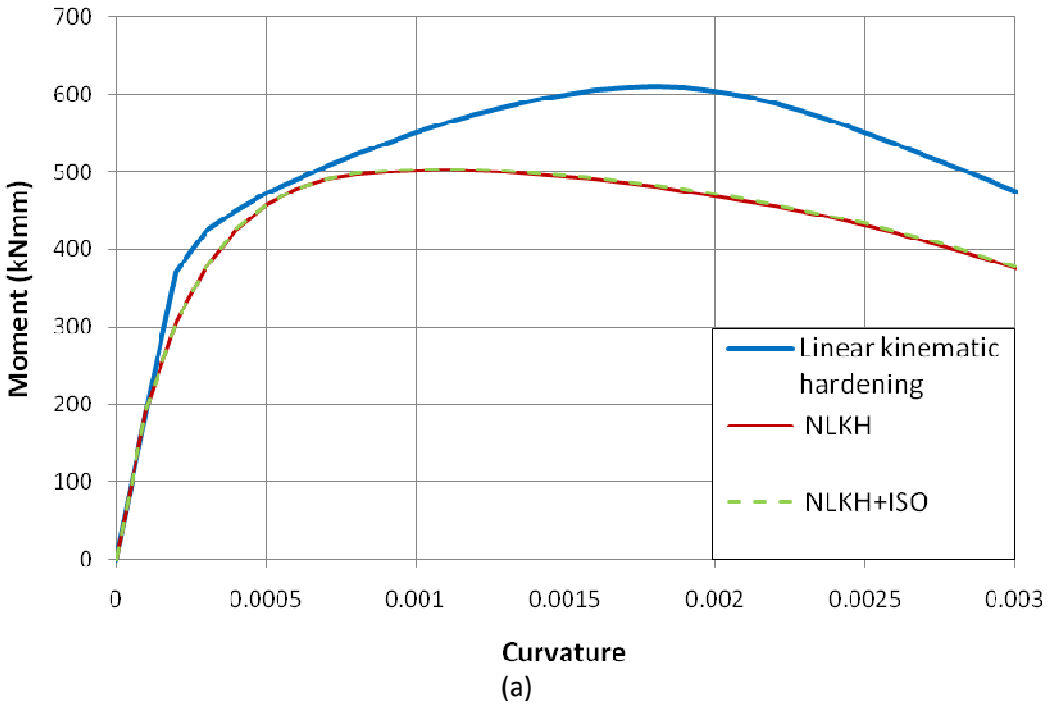

(a)

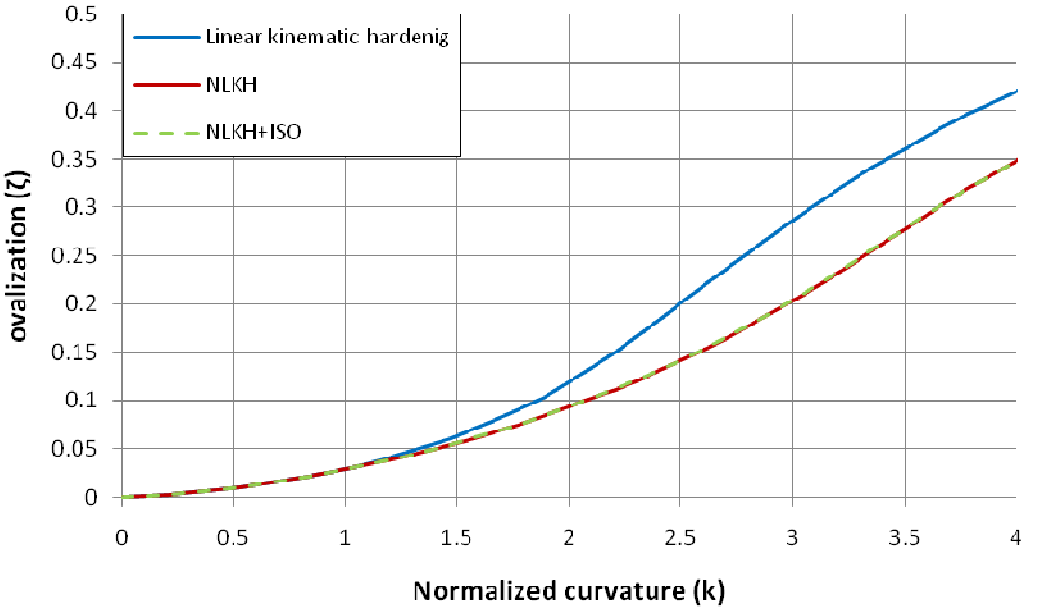

(b)

Figure 3.7: Monotonic pipe bending – "slice" model. (a) Moment-curvature diagram, (b) Ovalization-Normalized curvature diagram.

The same monotonic bending test is also simulated using the 3D model and the same geometry and material parameters. This is done for verification that the two developed models predict the dame pipe behavior. The simulation results of the two models adopted are presented in Fig. 3.8. Both models predict the same moment – curvature curve up to the point where the 3D model predicts a rapid loss of the pipe's bending capacity. This is due to local buckling failure of the pipe, a phenomenon which cannot be predicted with the "slice" model.

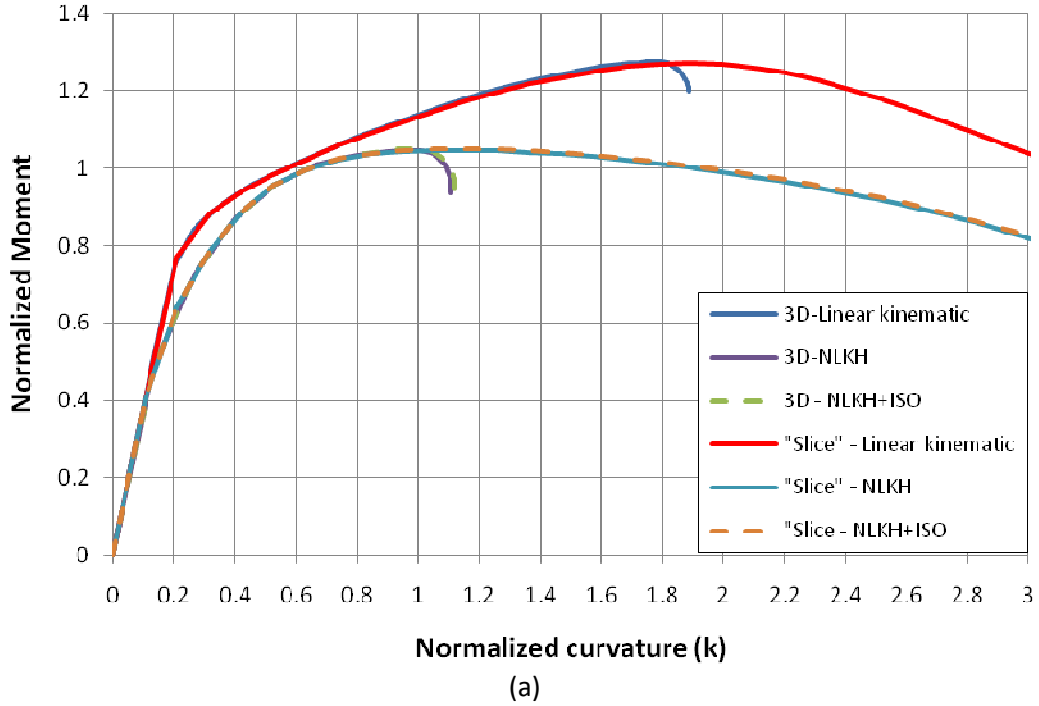

(a)

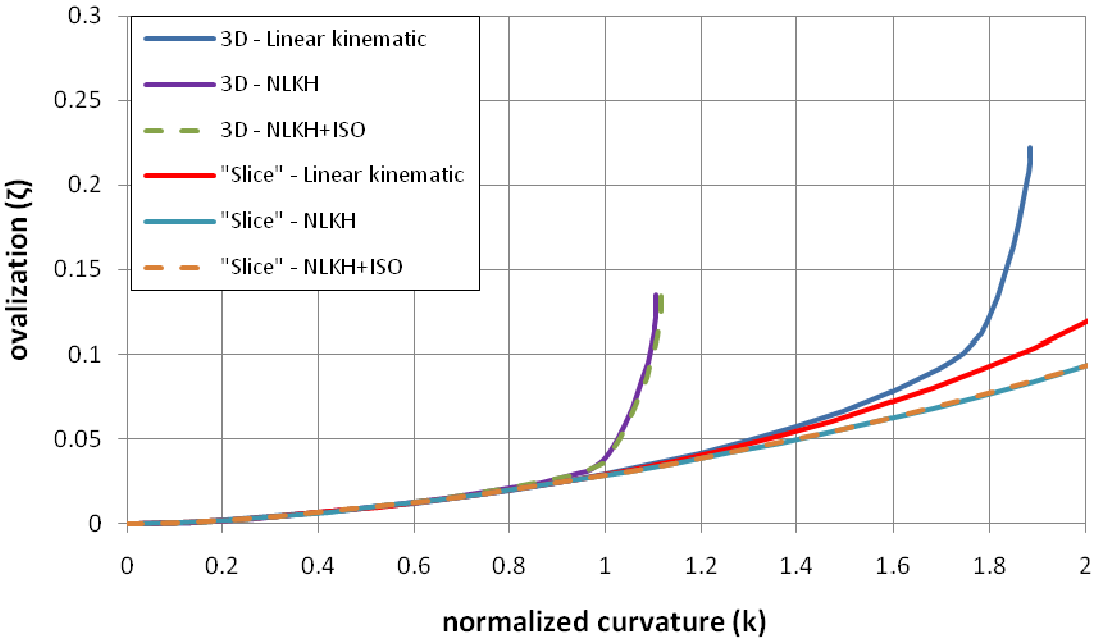

(b)

Figure 3.8: Monotonic pipe bending – 3D and "slice" model.
(a) Moment-curvature diagram, (b) Ovalization-Normalized curvature diagram.

3.2.2 Test setup, specimen geometry and material characteristics

The experiments were carried out on pipe specimens of steel alloy 4130. The test specimen was thin walled pipe with thickness 0.911 mm, outside diameter of 31.85 mm and length of 711 mm, which implies a diameter-to-thickness ratio equal to 34.96. This is the same pipe examined in the previous paragraphs. First, the pipe was subjected to internal pressure. When the desired internal pressure level was achieved, the pipe was subjected to cyclic bending by introducing rotation of its both ends. Two different values of rotation amplitude were tested. The smaller rotation was $\theta_c = 0.0924\ rad$ and the larger rotation value was $\theta_c = \pm 0.1930\ rad$. The internal pressure level in both cases was constant and equal to $P = 11.03\ MPa$.

A schematic representation of the bending device is show in Fig. 3.9. It is basically a four point bending device capable of applying loading and reverse loading through the rotation of the two sprockets. The pipe internal pressure is provided by a pressure intensifier with closed loop control, which allows maintaining a constant pressure in spite of the change of internal volume of the specimen. For more details concerning the test device, the reader is referred to the original work by Kyriakides and his coworkers [Kyriakides and Shaw (1987), Corona and Kyriakides (1991)].

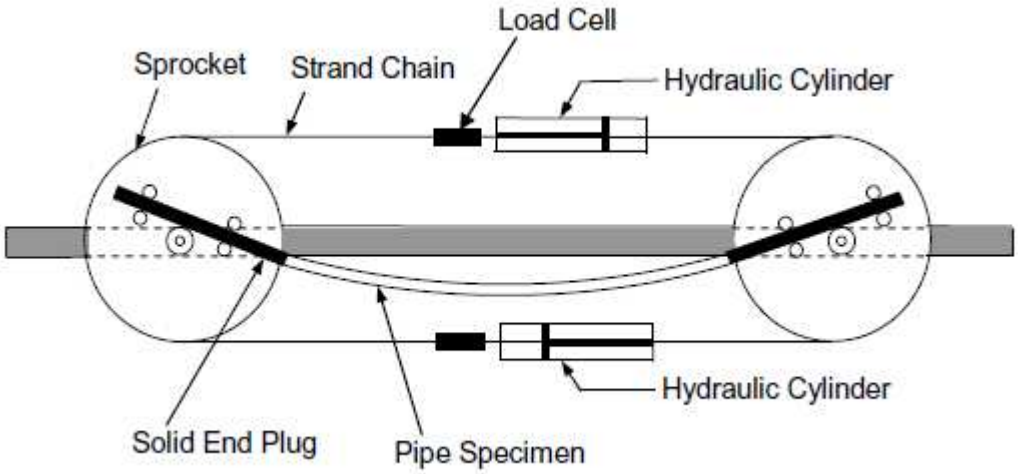

Figure 3.9: Schematic representation of the test setup, Rahman et al. (2008)

All the models examined in the study by Rahman et al. (2008) had to be calibrated through the proper definition of their parameters. Therefore symmetric, axial-strain controlled experiments were conducted on material specimens of the chosen alloy. The strain range was 0.75% and the results of the stable hysteresis loop are shown in Fig. 3.6. Certain models also required uniaxial and biaxial ratcheting test results for the calibration of their parameters. Therefore, two additional ratcheting tests were carried out. The uniaxial ratcheting test load amplitude chosen was $\sigma_{xa} = 540\ MPa$ and the mean stress was $\sigma_{xm} = 64\ MPa$. The biaxial loading conditions for the second test were a constant stress level of $\sigma_{\theta m} = 71\ MPa$ in the circumferential direction and axial strain amplitude of $\varepsilon_{xc} = \pm 0.4\%$. These experimental results are shown in Fig. 3.10 (a) and (b).

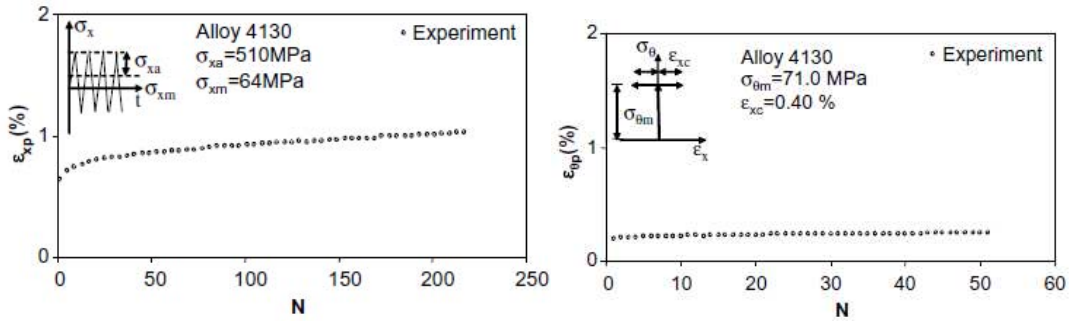

(a) (b)

Figure 3.10: Experimental result of 4130 steel alloy:
(a) uniaxial ratcheting experiment, (b) biaxial ratcheting experiment. [Rahman et al. (2008)]

The uniaxial ratcheting experiment presented in Fig. 3.10(a) was simulated by a one-element test in ABAQUS using the material parameters reported in Table 3.1 for each hardening rule adopted. The linear kinematic hardening rule predicts zero ratcheting as it was expected. The nonlinear kinematic hardening rule as well as the nonlinear kinematic/isotropic hardening rule predict ratcheting rates that are over-estimated and far from the measured behavior of the 4130 steel alloy. Therefore, one additional set of parameters under the name "NLKH ISO mod" is introduced. The corresponding values for each parameter used in this set are reported in the last column of Table 3.1. This new set is aimed at providing better ratcheting predictions. However, the model fails to simulate accurately the cyclic material loading test. All the above simulations are depicted in Fig.3.11 and Fig. 3.12.

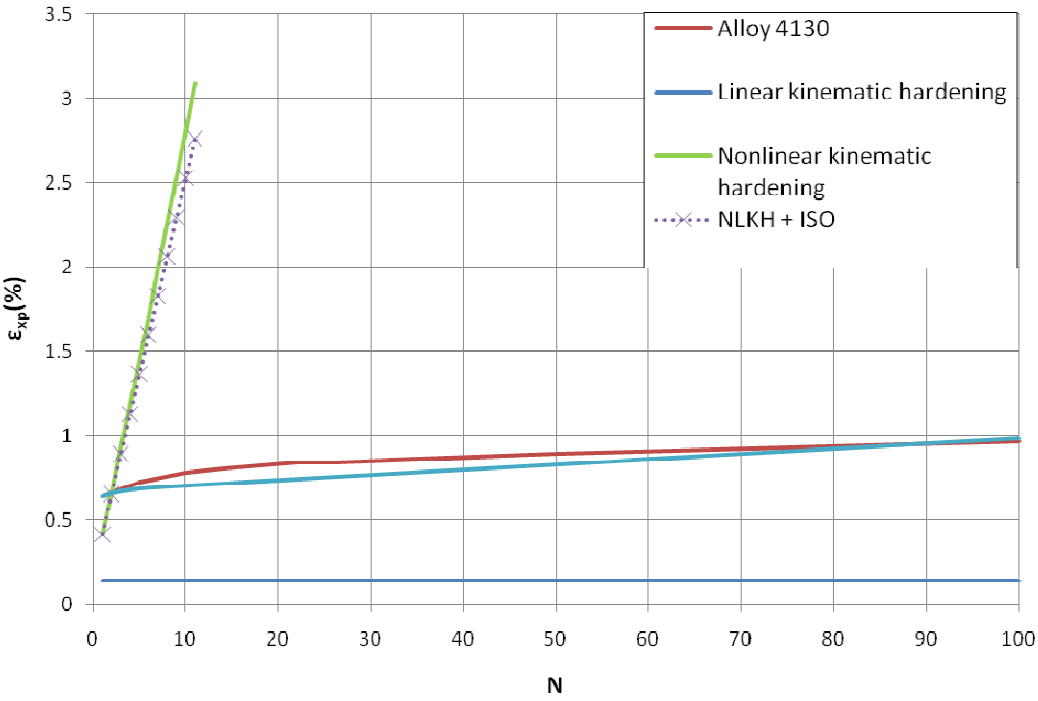

Figure 3.11: Uniaxial ratcheting experiment simulation

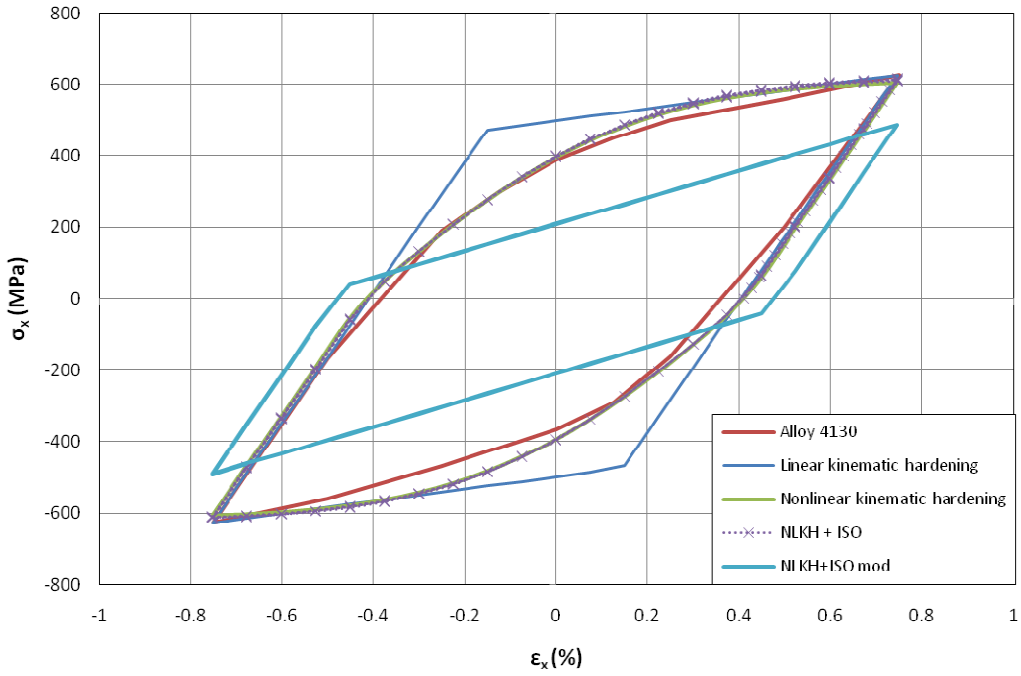

Figure 3.12: Simulation of the stable cyclic stress-strain hysteresis loop.

3.2.3 Experiment simulation – ovalization analysis

The pipe under consideration was subjected to symmetric rotation-controlled cyclic bending in the presence of internal pressure. The developed "slice" model shown in Fig. 3.4 was used to simulate the experimental results. The simulation predictions for cyclic applied rotation $\theta_c = 0.1930\ rad$ in the presence of internal pressure of $P = 11.03\ MPa$ are compared with the measured values in Fig. 3.13.

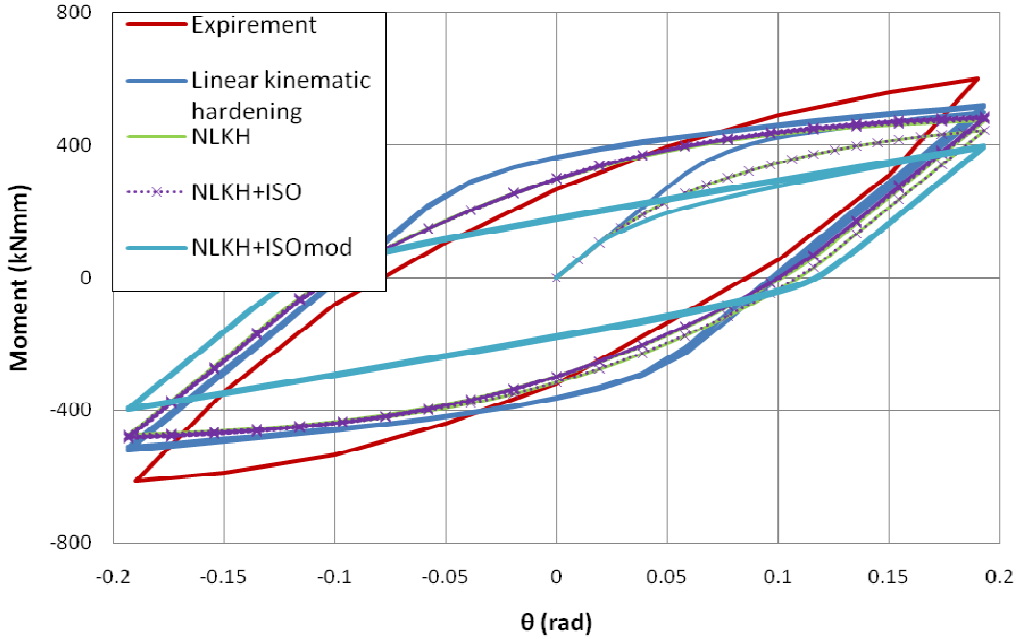

Figure 3.13: Moment rotation diagram for $\theta_c = 0.1930\ rad$.
Experimental results and numerical simulation predictions of the "slice" model.

The predicted cyclic behavior of the pipe resulting from the numerical simulation is close to the measured one on the experimental setup. The possible local buckling failure of the pipe cannot be captured though as discussed above. Therefore the 3D model has been used for the simulation of this experiment and all the following results are derived from it. As it will be discussed there, the influence of the boundary conditions is significant when the similar modeling used by Rahman et al. is adopted.

3.2.4 Experiment simulation - 3D model analysis

The developed 3D model is subjected to cyclic bending with two different applied end rotations equal to $\theta_c = 0.0924\ rad$ and $\theta_c = 0.1930\ rad$ in the presence of internal pressure $P = 11.03\ MPa$, as described in the previous paragraphs. The internal pressure is applied in a first step and it is kept constant for the subsequent steps. The pressure loading is decomposed in two parts; the pressure applied to the pipe wall and the axial pressure load due to the capped ends of the pipe. The results of this simulation are shown in Fig.3.14.

In the case of the smaller value of applied end rotation $\theta_c = 0.0924\ rad$ (Fig. 3.14(a)), all the predictions are very close to each other and close to the experimental measurements too. In the case of the applied rotation $\theta_c = 0.1930\ rad$, the predicted behavior of each hardening rule differs significantly. It is rather interesting that the linear kinematic hardening rule is capable of predicting a bending behavior very close to the one measured in the experiment. The predictions of the nonlinear kinematic hardening rule and the nonlinear kinematic/isotropic hardening rule coincide after a few cycles and are in fairly good agreement with the measured behavior. Finally, the modified nonlinear kinematic/isotropic hardening rule predictions are also not satisfactory as far as the shape of the hysteresis loop is concerned, but are closer to the maximum moment value predicted compared to the other nonlinear hardening rules.

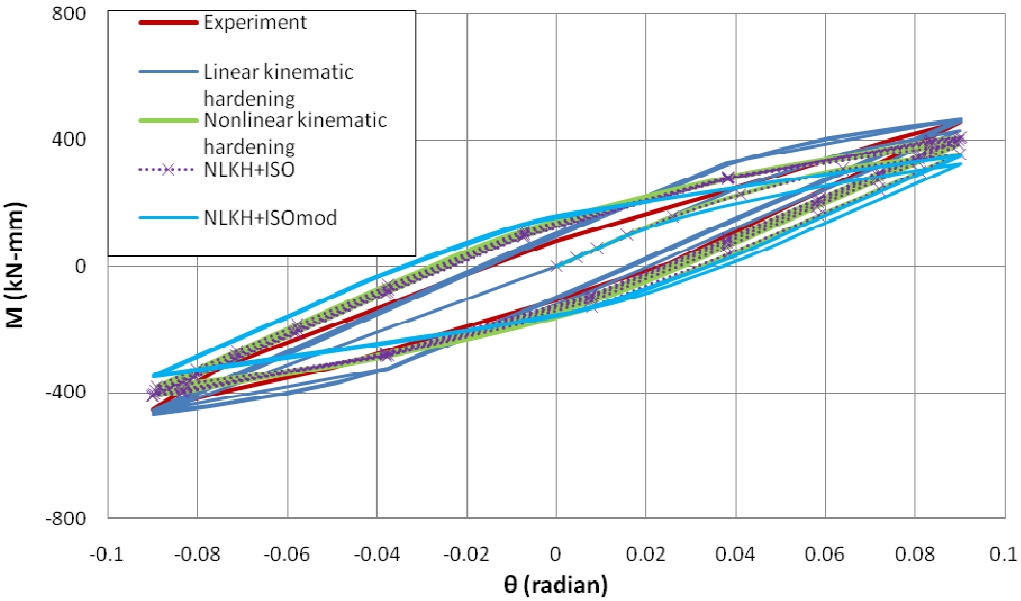

(a)

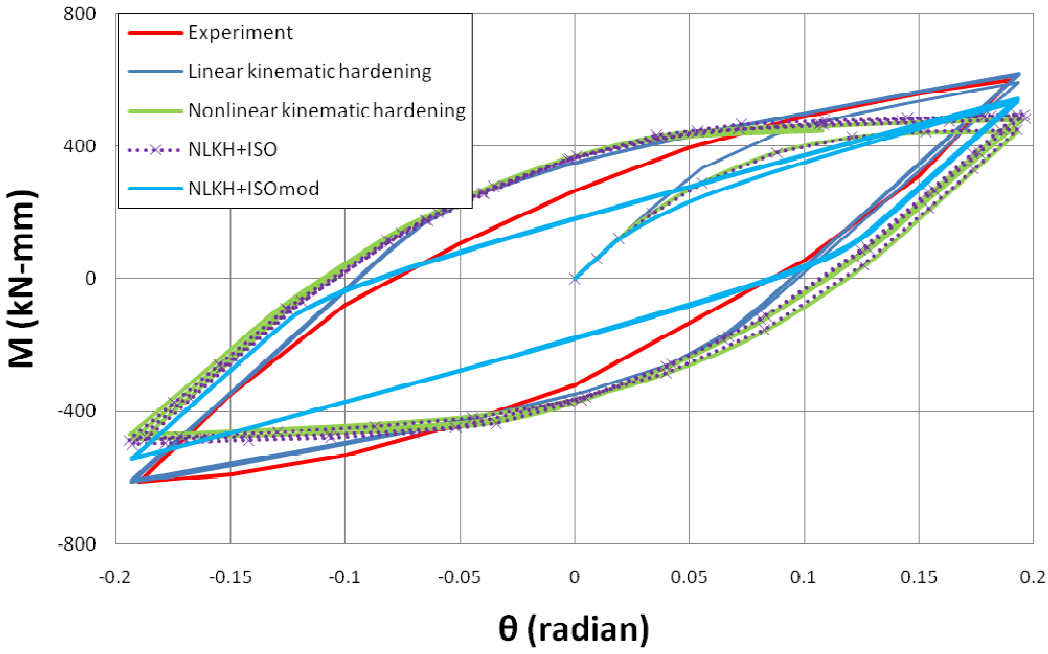

(b)

Figure 3.14: Moment rotation diagrams. (a) Applied rotation $\theta_c = 0.0924\ rad$ (b) Applied rotation $\theta_c = 0.1930\ rad$

In this simulation, the local stresses near the pipe ends due to the ovalization prevention imposed by the cap that develop during the internal pressure application step are quite higher than the stresses caused by the bending of the pipe. When nonlinear kinematic hardening rules (with or without the isotropic part) are employed, the stresses at the end of the internal pressure application step are very close to the yield stress of the material. As a consequence, the material exhibits local plastic deformations when the cyclic bending is applied. The drawback of the linear

kinematic hardening rule is that it cannot predict the localization of plastic deformations near the member end that lead to failure as shown in Fig.3.15. The reason behind this difference is the much higher yield stress that is used when the linear kinematic hardening rule is adopted.

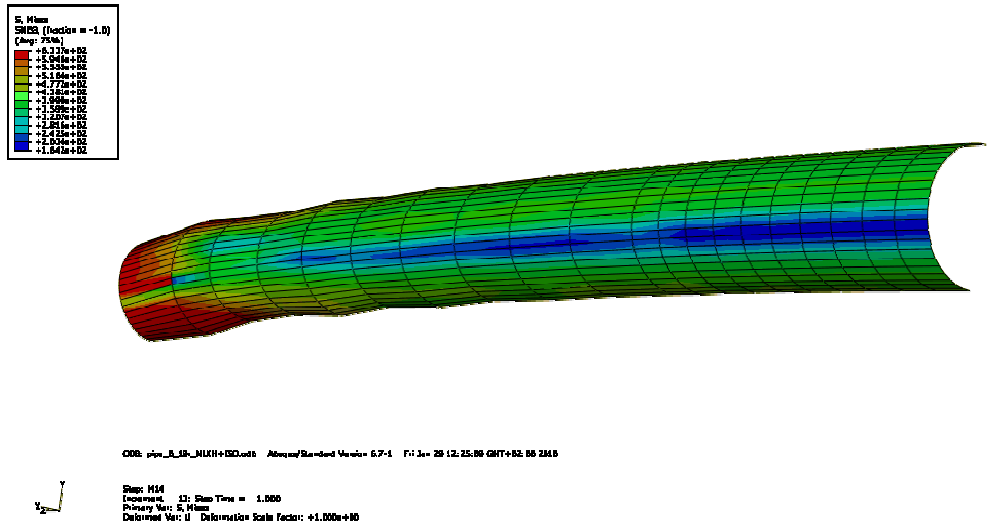

Figure 3.15: Localization of plastic deformations on the deformed geometry of the pipe after a few loading cycles.

Apart from the bending behavior of the pipe, the in-plane and out-of-plane diameter change is also monitored throughout the simulation. The deviation from the perfect round shape of the pipe cross-section is measured in the experimental setup with two strain gages at the middle of the pipe length as shown in Fig.3.16(a) and (b) . This point corresponds to the right end of the developed FE model (Fig.3.5) where the symmetry conditions are applied. The evaluation of the mean in-plane and out-of-plane diameter change peaks in each cycle is depicted in Fig.3.17.

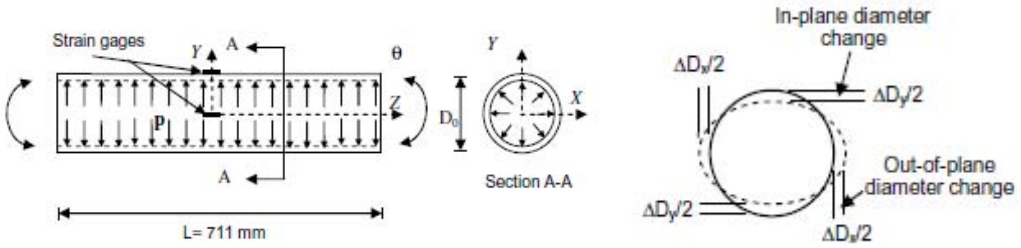

Figure 3.16: (a) Schematic representation of the pipe specimen, (b)Diameter change of the pipe cross-section.[Rahman et al (2008)]

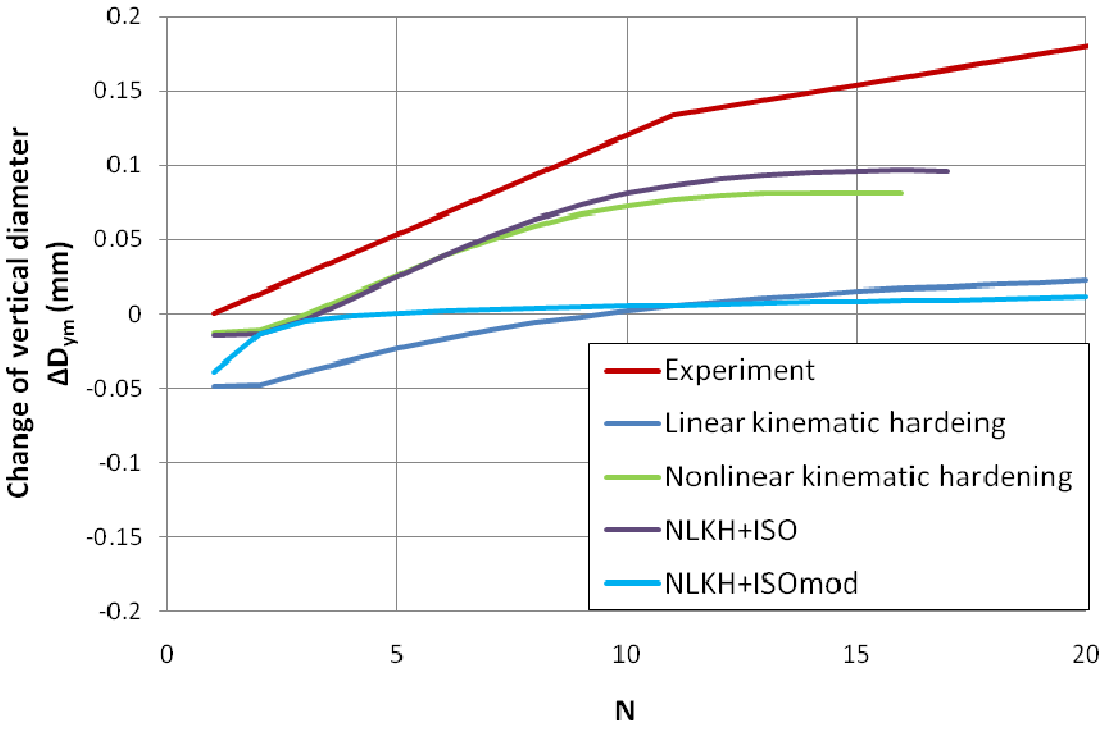

(a)

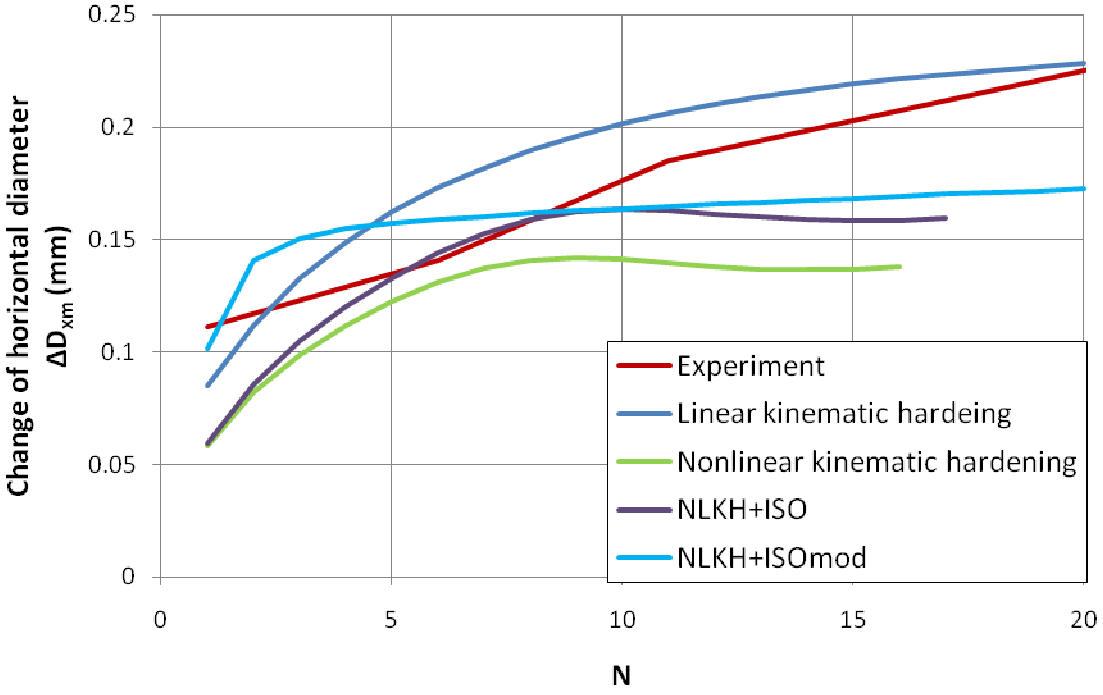

(b)

Figure 3.17: (a) Mean in-plane diameter change peaks versus the number of cycles N, (b) Mean out-of-plane diameter change peaks versus the number of cycles N.

The predictions of the in-plane and out-of-plane diameter change of all the adopted hardening rules are not satisfactory compared to the experimental measurements. Nevertheless, the nonlinear kinematic hardening rule and the nonlinear kinematic/isotropic hardening rule provide almost the same predictions

which are generally closer to the measured values. It should be noted that due to the fact that the local plastisfication phenomenon near the pipe end can be predicted by both these hardening rules, the analysis stops in less than 20 cycles due to local failure phenomena (Fig. 3.17(a) and (b)). The predictions of the linear kinematic hardening rule and the modified nonlinear kinematic/isotropic hardening rule are far from the measured values, especially in the out-of-plane diameter change measurements (Fig.3.17(b)). Finally, all the adopted hardening rules predict a constant ovalization after about 12 cycles. This observation contradicts the measured values, especially for a number of cycles greater than 50, not plotted in Fig.3.17.

3.2.5 Tubular members subjected to cyclic bending and constant external pressure

The effect of the external pressure on pipes has been of interest for many years, motivated by applications in deepwater tubular towers and pipelines, where external pressure is critical for the structural integrity of the pipe. External pressure actions are often combined with cyclic bending actions, as for example in the case of underwater pipeline installation procedure or due to wave actions on submerged parts of offshore structures. The effect of the external pressure combined with cyclic bending will be examined in the following paragraphs through illustrative examples, with curvature-controlled and moment-controlled cyclic bending simulations.

3.2.5.1 Curvature-controlled cyclic bending and constant external pressure.

To examine curvature-controlled cyclic bending problem in the presence of steady external pressure the “slice” model presented in Paragraph 3.2 is used. The external pressure is applied in a first step and then it is kept constant as the subsequent cyclic bending steps take place. The three different types of hardening rules examined so far will be employed here as well, keeping the parameters used for each hardening rule the same with those reported in Table 3.1.

In Fig.3.18 the results of a symmetric cyclic bending ($R=-1$) simulation with steady external pressure applied of the specific pipe geometry are presented. The applied external pressure is 19.5% of the critical pressure described by the following equation:

$$p_{cr}=\frac{Et^3}{4r^3(1-\nu^2)} \tag{3.2}$$

where ν is the Poisson ratio equal to 0.302.

The linear kinematic hardening rule predictions present a slight cyclic softening phenomenon which stabilizes after a few bending cycles. On the contrary, the nonlinear kinematic hardening rule and the nonlinear kinematic/isotropic hardening rule predictions present an intense cyclic softening phenomenon which

stabilizes when almost 70% of the pipe's bending capacity is lost (Fig.3.18(a)). The ovalization predictions of the three hardening rules adopted differ significantly as well. The linear kinematic hardening rule predicts in general smaller ovalization values. The initial rate at which the ovalization of the pipe cross-section propagates is small and tends to zero after some cycles. The nonlinear kinematic hardening rule and the nonlinear kinematic/isotropic hardening rule ovalization predictions are remarkably different than the predictions of the linear kinematic hardening rule. These two hardening rules predict an ovalization value about 4 times higher after 10 cycles compared to the linear kinematic hardening predictions. Moreover, the initial rate of ovalization evolution increases and then decreases rapidly when stabilization takes place (Fig. 3.18(b) and (c)).

The predicted behavior is not in good agreement with similar experimental data (Corona & Kyriakides (1991)) where the ovalization propagation rate increases monotonically. It should be noted that the linear kinematic hardening rule predictions are closer to the actual expected behavior. Generally, none of the examined hardening rules can provide accurate and safe predictions about the bending behavior and ovalization propagation of the pipe.

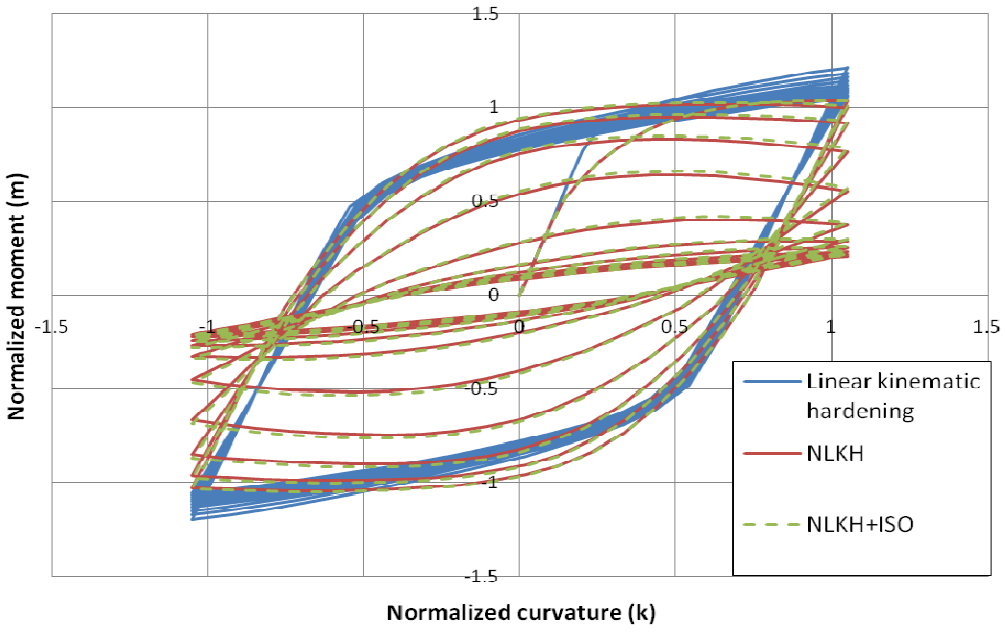

(a)

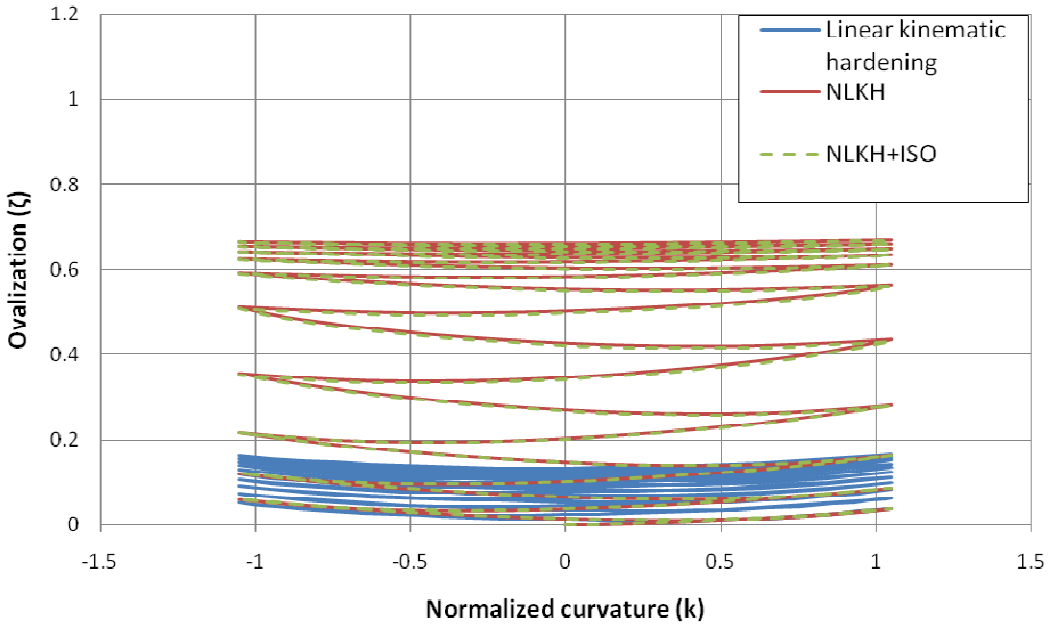

(b)

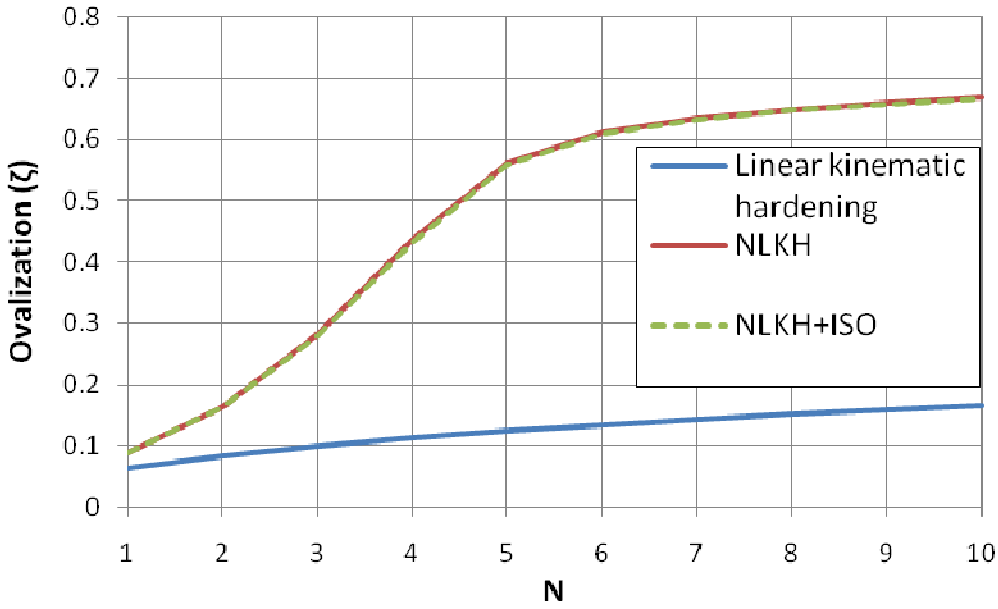

(c)

Figure 3.18: Cyclic pipe bending ($R = -1$) in the presence of steady external pressure. (a) normalized moment- curvature diagram, (b) Ovalization- curvature diagram, (c) Ovalization versus the number of cycles.

3.2.5.2 Moment-controlled cyclic bending and constant external pressure.

The two-dimensional "slice" model is used to simulate a moment-controlled cyclic bending experiment in the presence of steady external pressure. As in the case described in the previous paragraph, external pressure is applied in a first step and it is kept constant for the subsequent cyclic bending steps. The value of the applied

pressure as well as the parameter sets of the hardening rules are the same for all analyses considered.

The predictions from the three hardening rules are different. The linear kinematic hardening rule predicts a closed and stable hysteresis loop. The nonlinear kinematic hardening rule and the nonlinear kinematic/isotropic hardening rule predictions are significantly different compared to the linear kinematic hardening rule. The predicted maximum curvature is about 2 times the one predicted by the linear kinematic hardening rule and it increases with repeated loading. The ovalization increases at each cycle as presented in Fig.3.19(a) and (b), but the nonlinear kinematic hardening rule and the nonlinear kinematic/isotropic hardening rule predict different ovalization values after the first cycles. This is clearly attributed to the external pressure applied. Finally, the linear kinematic hardening rule is the only hardening rule that predicts stabilization of the ovalization evolution, while the other two nonlinear hardening rules predict a rapid increase of the ovalization indicating that failure will follow in the subsequent cycles (Fig. 3.19(c)).

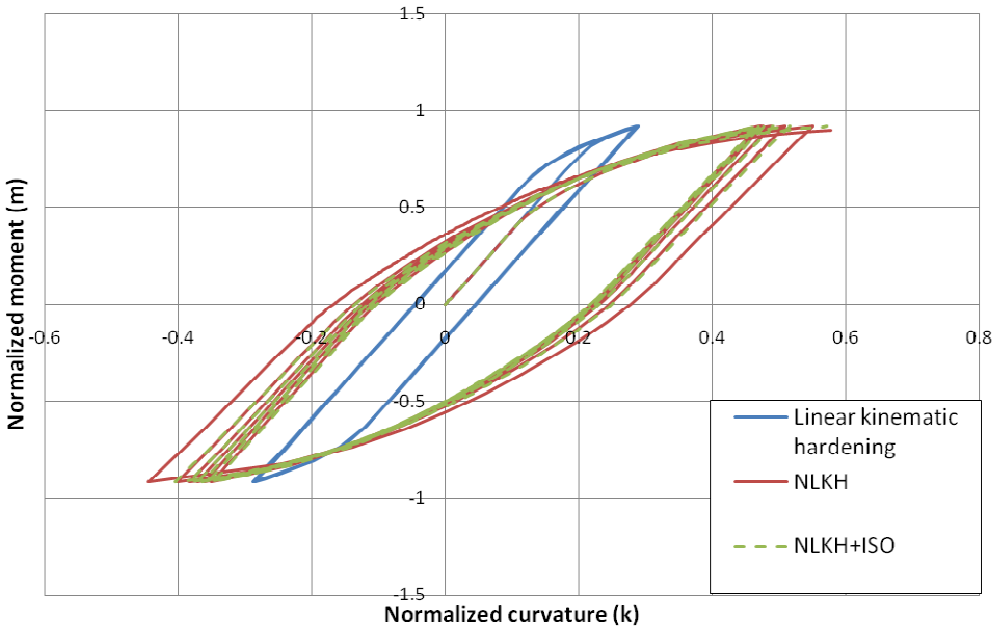

(a)

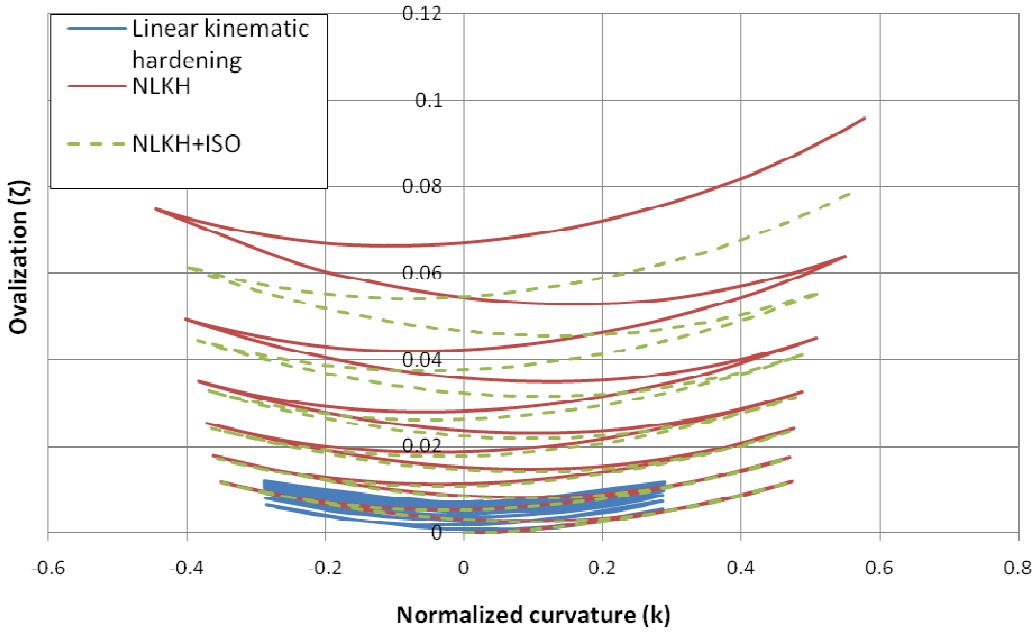

(b)

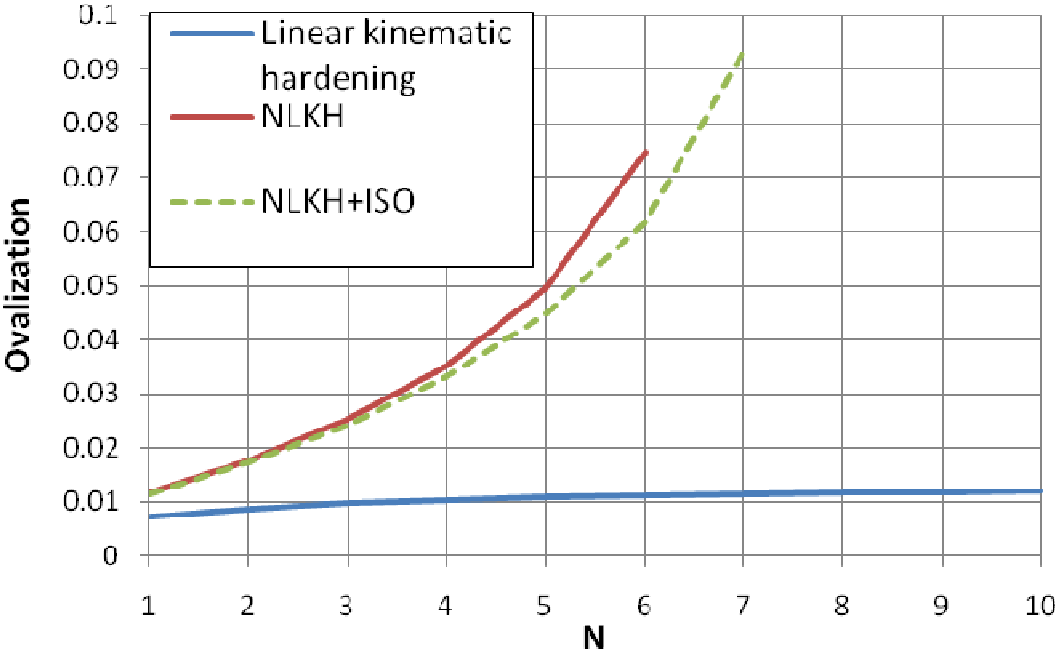

(c)

Figure 3.19: Cyclic pipe bending ($R = -1$) in the presence of steady external pressure. (a) Normalized moment- curvature diagram, (b) Ovalization- curvature diagram, (c) Ovalization evolution in terms of the number of cycles.

3.3 Tubular members subjected to cyclic bending

The behavior of tubular members subjected to monotonic and cyclic bending is investigated in the present paragraph through an appropriate selected example

case. In all the following simulations the developed “slice” model is used. The effect of the Armstrong – Frederick hardening rule on the accurate prediction of the total pipe behavior is illustrated.

3.3.1 Curvature-controlled cyclic bending.

Following the simulation of monotonic bending of the pipe and keeping the same geometry and material parameters, the pipe is subjected to 10 cycles of curvature-controlled bending. The chosen normalized curvature limits are equal to $k/k_N = -0.5254$ and $k/k_N = 1.0507$, which results to a loading ratio $R = k_{\min}/k_{\max}$ equal to -0.5. The normalized curvature limits are as shown in Fig. 3.20(a). The resulting moments are normalized by $M_N = \sigma_y D^2 t$, where for the values of D, t are kept the same as in the monotonic case, while the yield stress σ_y value is chosen equal to 550 MPa; in all cases, the yield stress assumed when the linear kinematic hardening rule is adopted. The ovalization propagation is also plotted in Fig. 3.20(b).

The observed differences in these the normalized moment – curvature are attributed to the different size of the yield surface assumed when the different hardening rules are adopted as described in Table 3.1. The linear kinematic hardening rule predicts almost stable hysteresis loops (Fig. 3.20(a)). The corresponding curvature propagates during the first cycles but stabilizes after the first five cycles until the end of the loading (10th cycle). On the contrary, when the nonlinear kinematic hardening rule or the nonlinear kinematic/isotropic hardening rule is adopted, cyclic softening is observed. The corresponding curvature propagates with almost constant rate (Fig. 3.20(b)).

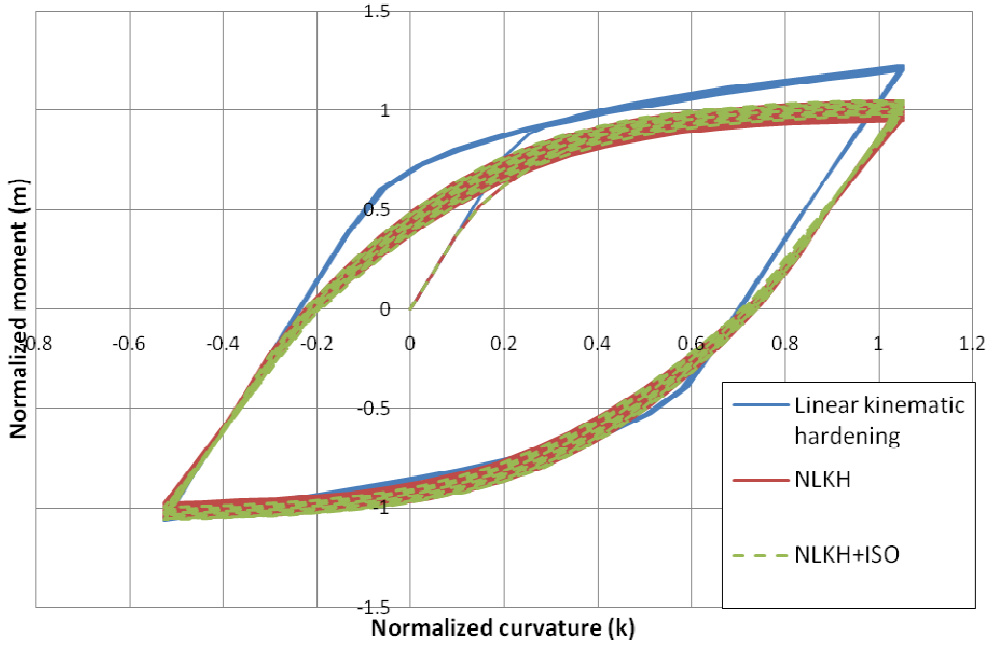

(a)

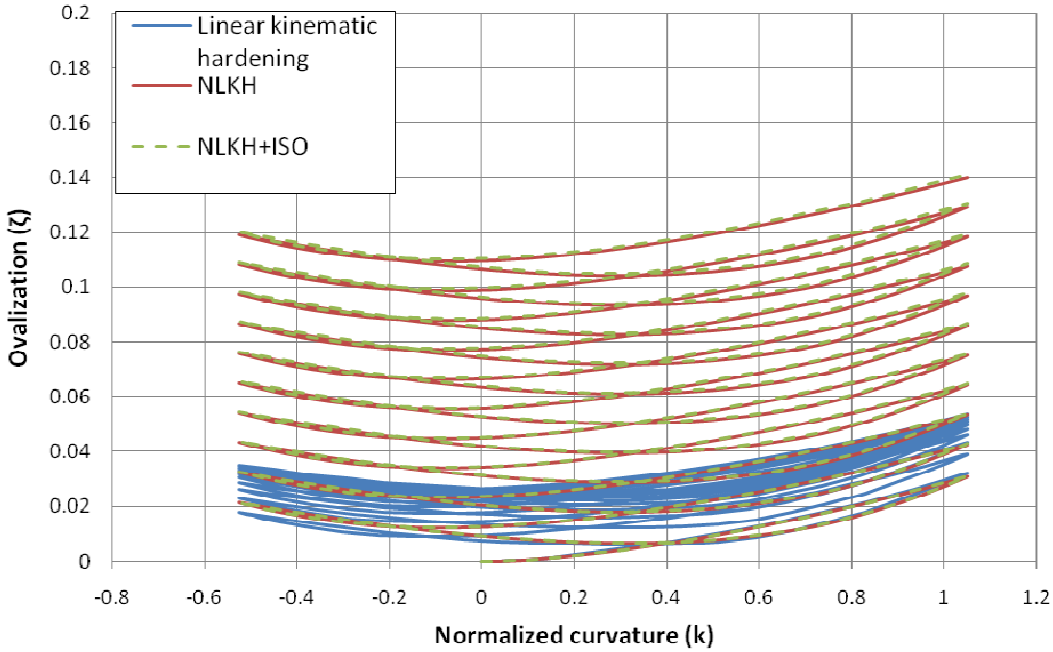

(b)

Figure 3.20: Cyclic pipe bending ($R=-0.5$). (a) Normalized moment- Normalized curvature diagram, (b) Ovalization-Normalized curvature diagram.

In order to examine the effect of the unsymmetrical bending of a tube on the hysteresis loops and the corresponding curvature evolution for the three hardening rules examined, two sets of curvature-controlled cyclic bending simulations are conducted. In these simulations the maximum applied curvature is kept constant and equal to $k/k_N=1.0507$. The minimum limit of the applied curvature is now fixed to $k/k_N=0$ to and $k/k_N=0.5254$ respectively. This results to minimum to maximum curvature ratios $R=k_{\min}/k_{\max}$ equal to 0 and 0.5 respectively.

Both loading schemes limit the applied curvature to zero and positive values. The results in Fig.3.21 and Fig.3.22 show that the consequence of the loading scheme is important on both the cyclic softening phenomenon predictions and the predicted rate of the ovalization propagation. As far as cyclic softening of the tube is concerned, increasing the ratio of minimum to maximum curvature, the phenomenon is more intense in the first one or two cycles but stabilizes faster after these cycles. The corresponding ovalization predictions are also very interesting. For $R=0$, the rate of the ovalization development is significantly lower (about half) compared to the rate of development when $R=-0.5$. Moreover, when $R=0.5$, the ovalization of the tube section initially decreases due to the reverse loading. But since the reverse loading does not imply normalized curvature less than 0.4 (Fig.3.21 and Fig.3.22), the ovalization stabilizes in this part of the graph.

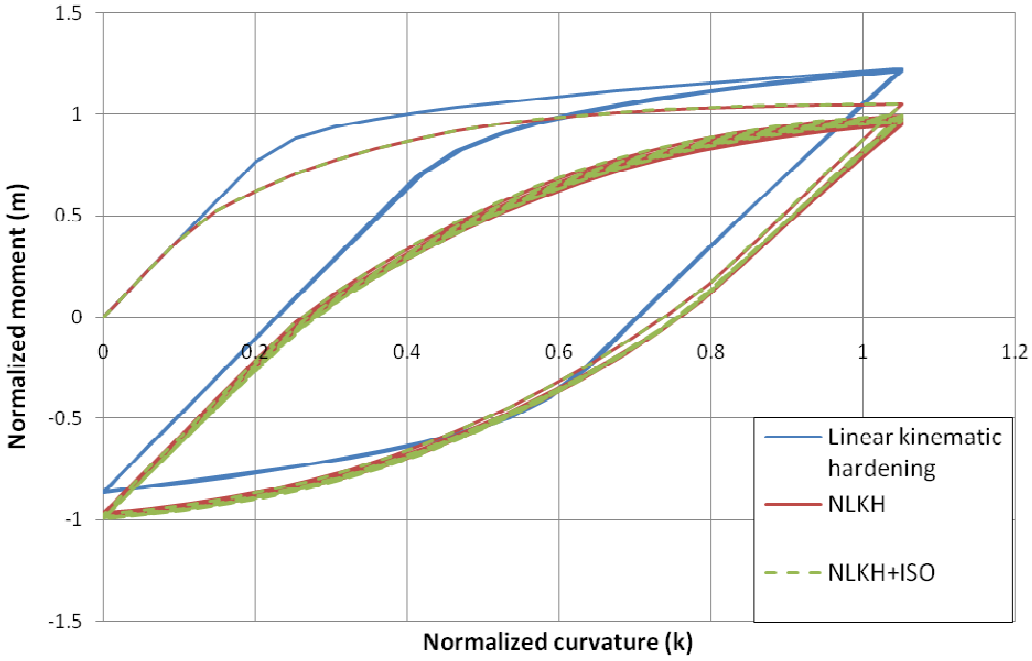

(a)

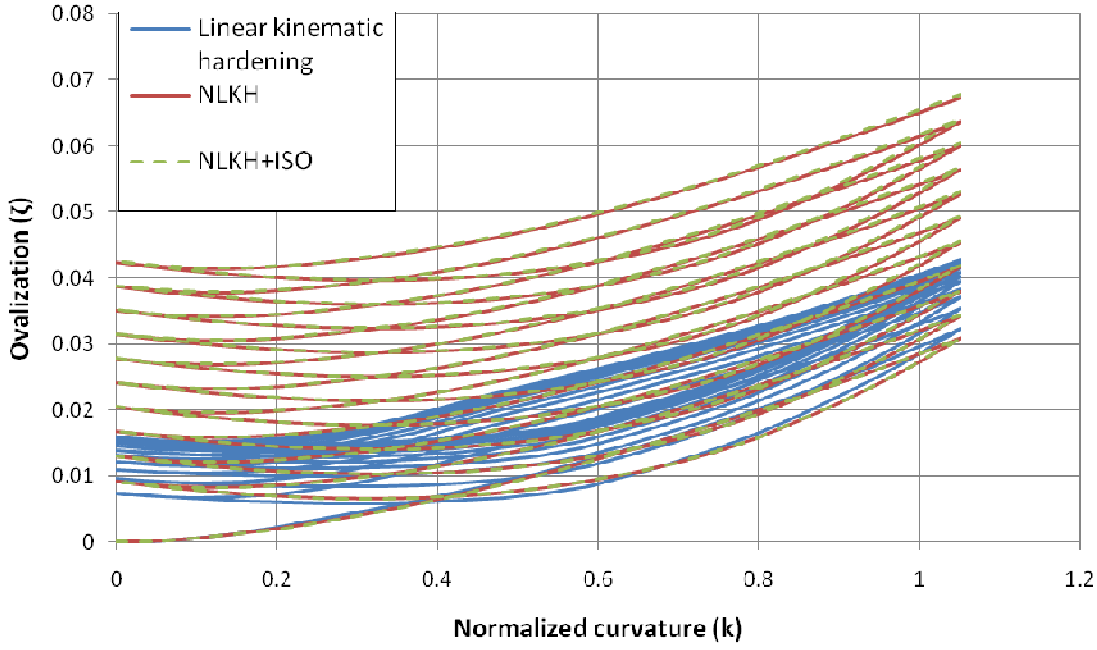

(b)

Figure 3.21: Cyclic pipe bending under rotation-controlled conditions ($R = 0$). (a) Normalized moment- curvature diagram, (b) Ovalization- curvature diagram.

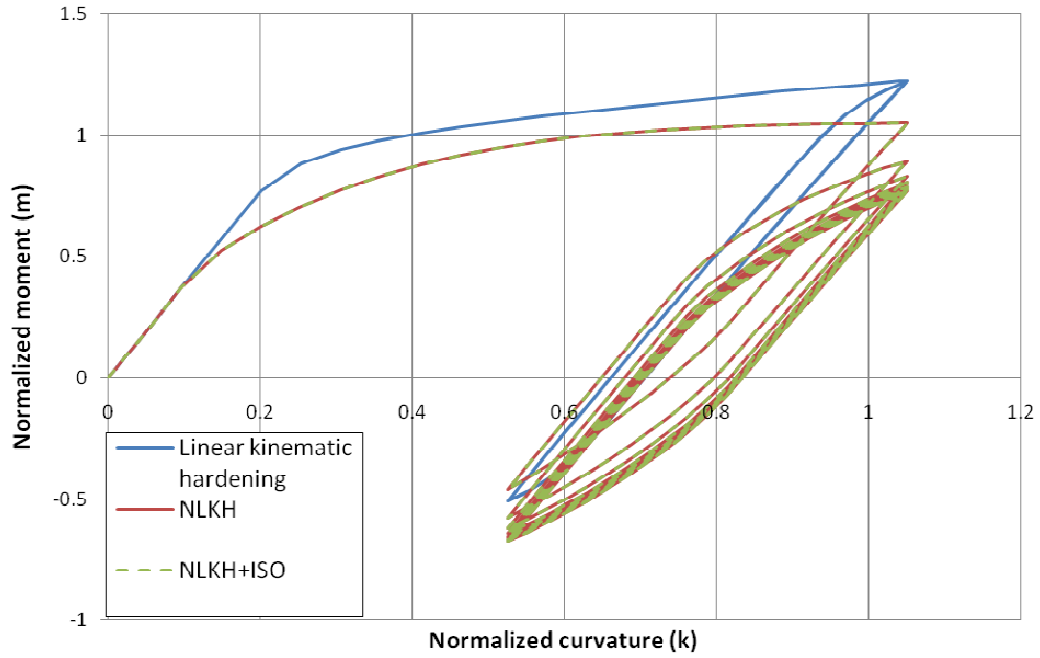

(a)

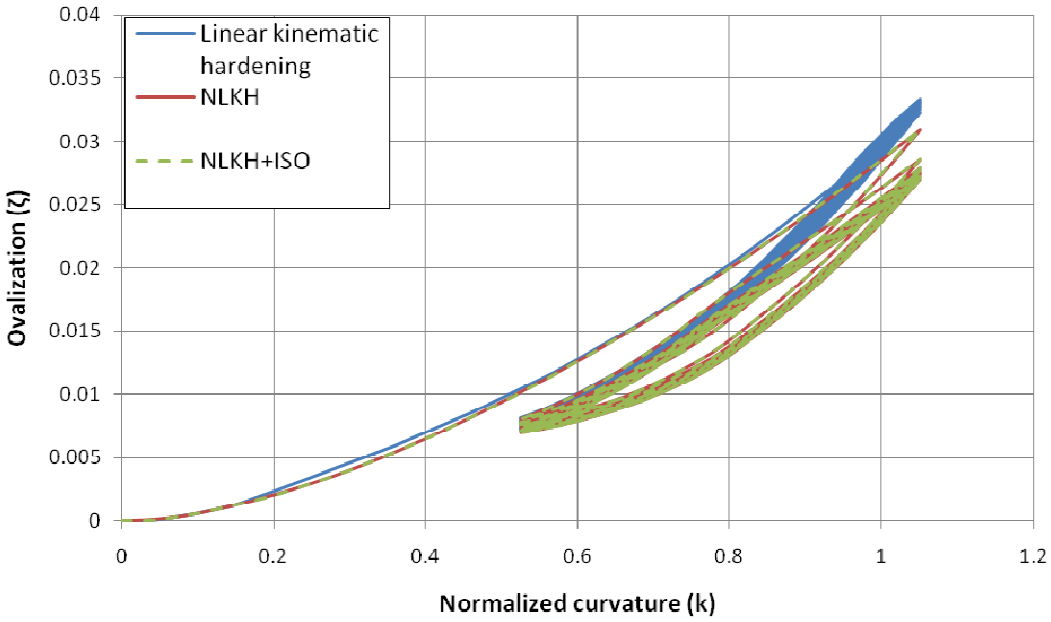

(b)

Figure 3.22: Cyclic pipe bending under rotation-controlled conditions ($R = 0.5$).
(a) Normalized moment - curvature diagram, (b) Ovalization- curvature diagram.

3.3.2 Moment-controlled cyclic bending

Starting from symmetric loading, as the one described in Fig. 3.23 with $R = M_{\min} / M_{\max}$ ratio equal to -1, and using the same material parameter sets

described in Table 3.1, the hardening rule adopted can influence the predicted behavior significantly. The linear kinematic hardening rule predicts a closed hysteresis loop as in the case of curvature controlled cyclic bending. The nonlinear kinematic hardening rule and the nonlinear kinematic/isotropic hardening rule predict a slight cyclic degradation behavior of the pipe which is stabilized after a few loading cycles. The observed difference in size of the predicted hysteresis loops is shown in Fig. 3.23(a). Moreover, the corresponding curvature to the maximum applied moment differs significantly as it is clearly shown in Fig. 3.23(b) as well. Finally, after a few loading cycles, the curvature predictions of the nonlinear kinematic hardening rule and the nonlinear kinematic/isotropic hardening rule start not to coincide due to the cyclic hardening of the material assumed in the second hardening rule (Fig. 3.23(b)).

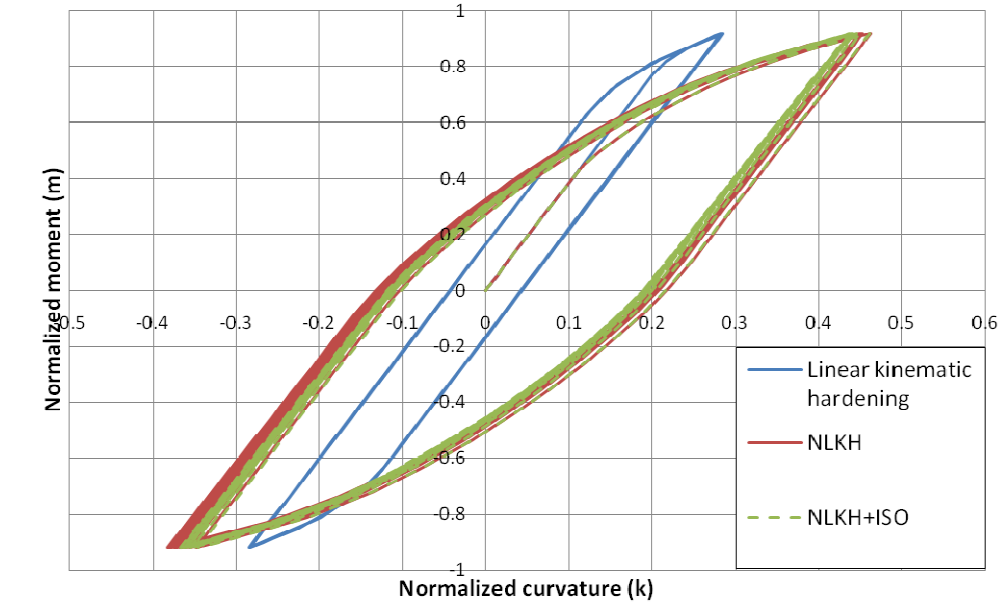

(a)

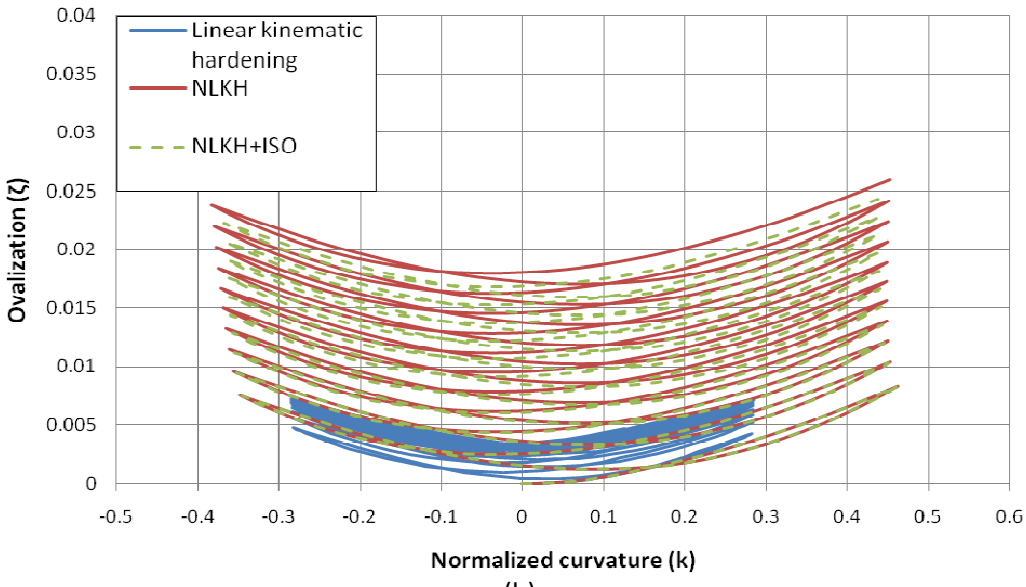

(b)

Figure 3.23: Cyclic pipe bending under moment-controlled conditions ($R = -1$). (a) Normalized moment- curvature diagram, (b) Ovalization- curvature diagram.

In the case of unsymmetric bending loading, the predicted behavior of the FE model depending on the hardening rule is more significant. In Fig.3.24, the simulation of such cyclic loading sequence with $R = M_{\min}/M_{\max}$ equal to -0.41 is depicted. It is observed that the hysteresis loops translate in the direction of the mean curvature; that is, after each loading cycle there is accumulation of curvature resulting to the horizontal shift of the center of each hysteresis loop. The reader is referred to the works of Chang, Pan and Lee (2008) among other researchers, where the aforementioned phenomenon is verified by experimental measurements.

The linear kinematic hardening rule prediction may not simulate this phenomenon in a precise and robust way. According to this hardening rule, there is nonlinear behavior of the pipe only during the first quarter of the first loading cycle and then during all the subsequent cycles the tube performs elastically (Fig. 3.24(a)). This has also a consequence on the predicted curvature (Fig. 3.24(b)). A significantly better description of this phenomenon in terms of experimental observations is given by both the nonlinear kinematic hardening rule and the nonlinear kinematic/isotropic hardening rule. The horizontal shifting of the subsequent hysteresis loop centers is captured in a consistent manner. The isotropic part of the nonlinear kinematic/isotropic hardening rule is responsible for the observed differences in Fig. 3.24(a) and (b). The initial shifting rate predicted by both these hardening rules is the same. As the equivalent plastic strain increases though, the size of the yield surface increases as well, which results to a reduction of the shifting rate (Fig.3.25).

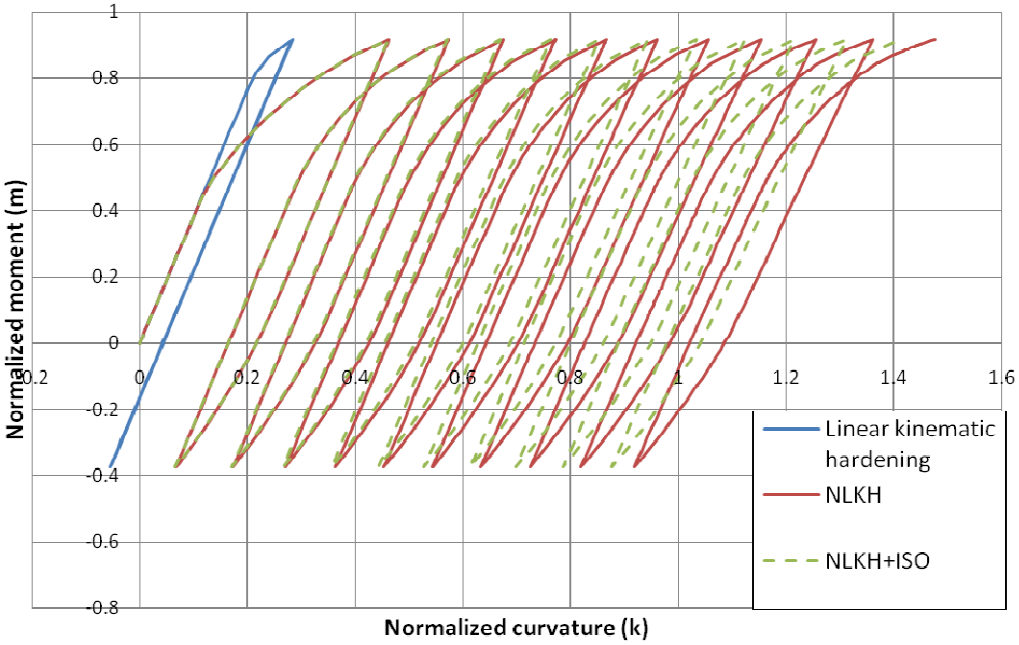

(a)

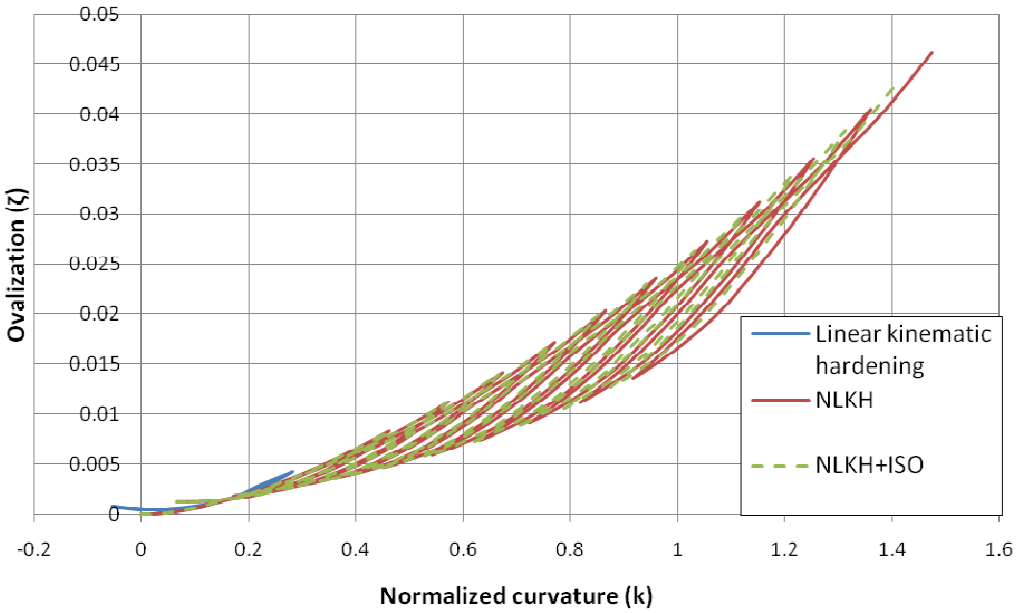

(b)

Figure 3.24: Cyclic pipe bending under moment-controlled conditions ($R = -0.41$). (a) Normalized moment- curvature diagram, (b) Ovalization - curvature diagram.

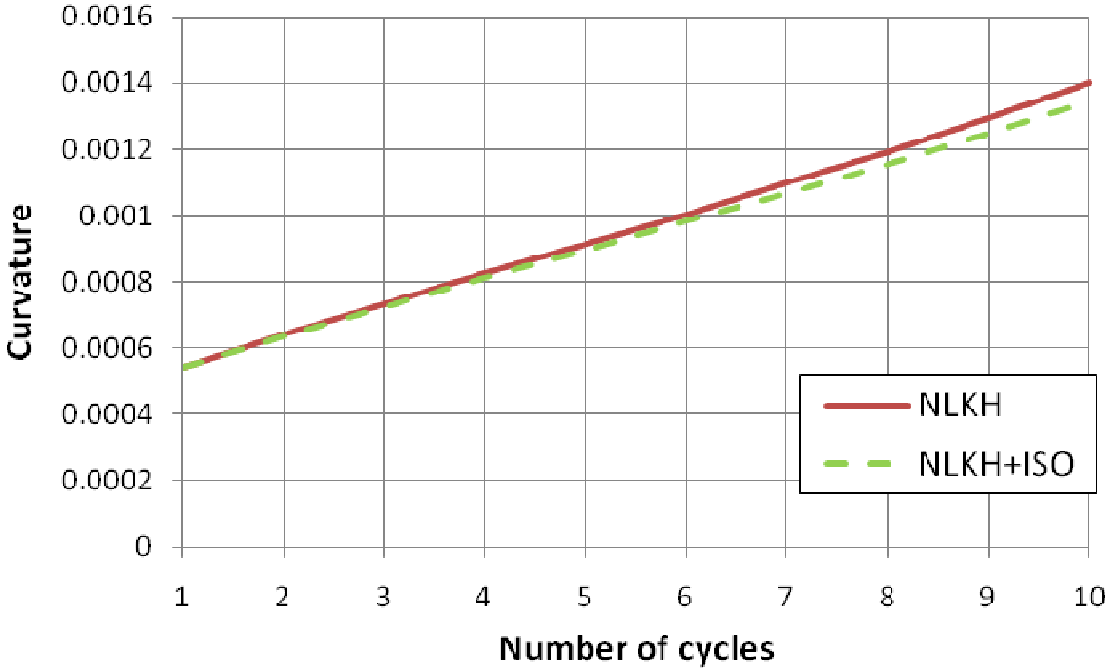

Figure 3.25: The evolution of curvature.

4. Simulation of the UOE pipe manufacturing and structural behavior

4.1 Introduction

Oil and gas pipelines are widely used in transporting hydrocarbon energy resources in the most effective and safe way. Pipelines usually require a significant initial investment cost for their manufacturing, but during their service life (30-40 years) they have relatively low maintenance and operation costs. In the recent years a considerable number of pipelines has been constructed or are in the design stage. In addition several important pipeline projects are in the planning stage, which quite often connect different countries or different continents (e.g. Europe – Asia, Europe – Africa). In some cases, a long segment of the pipeline is underwater. The current technological know-how allows for the installation of such pipes in water depths exceeding 2000 m, as for example the Blue Stream gas pipeline that connects Russia and Turkey through the Black Sea (DeGeer et al. (2005).

The mechanical design of offshore pipelines, according to the modern design concept, is based on the limit-state design approach, where pipeline design should consider all possible failure modes. Buckling under external pressure constitutes a fundamental limit state for the design of offshore pipelines. The external pressure is due to the significant water depth, the corresponding failure is commonly mentioned as “collapse” (Langner (1984), Karamanos and Tassoulas (1991), Yeh and Kyriakides (1986)), associated with a flattened “dog-bone” shape of the pipe cross-section.

To resist high levels of external pressure, deep-water pipelines are thick-walled with a value of diameter-to-thickness ratio D/t that is usually less than 25. The external pressure capacity of thick-walled pipelines has been studied in numerous publications as for example in the work of Yeh and Kyriakides (1986), Gresnigt et al. (2000) and Kyriakides and Corona (2007) among others. In those publications, it was recognized that those pipelines fail at a pressure level which is close to the nominal yield pressure of the pipe cross-section ($p_y = 2\sigma_y t/D$). In addition, it was found that the value of the ultimate pressure is sensitive to the presence of initial imperfections and residual stresses.

The manufacturing process has a significant effect on the level of imperfections and residual stresses in a line pipe, and therefore, it should be taken into consideration for the prediction of the ultimate external pressure. In the present paper, the UOE cold-forming manufacturing process is examined in terms of its effects on the mechanical behavior of offshore pipelines under external pressure. An initial study on the effects of the UOE process has been reported by Kyriakides et al. (1992) using a simple analytical model. Recent studies (Herynk et al. (2007), Toscano et al. (2008)) that employed finite element analysis have highlighted the influence of this manufacturing process on the value of maximum external pressure. In the present study, the UOE forming process for a 24-inch pipeline, candidate for deep-water pipeline applications, is simulated using nonlinear finite element models, so that initial imperfections and residual stresses at the end of the manufacturing process are predicted. Subsequently, using the finite element simulation, the pipe is

subjected to external pressure loading for the calculation of the ultimate external pressure. The present simulation may be employed as a useful tool for predicting the ultimate capacity of the pipeline, and optimizing the UOE manufacturing process.

4.2 Description of the UOE manufacturing

A popular manufacturing method for large diameter pipes used in subsea applications consists of cold-forming long plates through the UOE process. The name UOE stems from the initials of the last three of these mechanical steps (**U**-ing, **O**-ing, **E**-xpansion). The UOE steel pipe forming process was originally proposed for buried onshore pipes and was extended to subsea pipes in the recent years.
The process is realized in four sequential mechanical steps:

(a) Crimping the plate edges
(b) U-ing phase where the pipe is formed into a U-shape
(c) O-ing phase where the pipe is pressed into a quasi-circular shape and both ends of the plate are welded
(d) Expansion phase through the application of internal pressure for improving the “circularity” of the pipe

All the above steps will be described in detail in the following.

4.2.1 Crimping phase

The first forming step involves crimping of the plate edges at both sides into circular arcs of about one radius width. This is achieved by pressing the ends between two shaped dies as shown in Fig. 4.1. Because of the large forces required in this step, the forming is executed in steps.

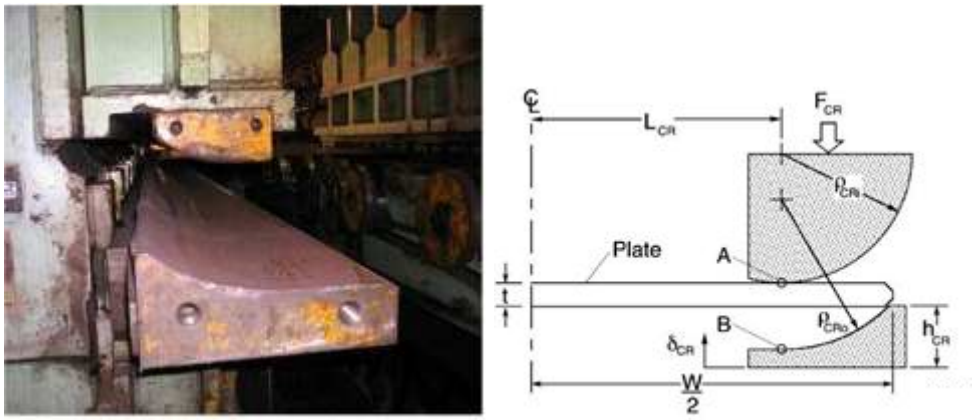

(a) (b)

Figure 4.1: The crimping phase, where the lower die moves upwards; (a) Representative phase of the forming process (b) Schematic representation of crimping press.

[Herynk et al. (2007)]

The length of the plate in the longitudinal direction varies between one and four times the pipe diameter, depending on the pipe thickness. Each production factory is

equipped with several sets of dies in order to adjust the forming process to the desired thickness and diameter of the pipes required. In particular, for a given pipe the dies with the most appropriate inner and outer radii (ρ_{CRi} and ρ_{CRo}) are selected, as depicted in Fig. 4.1(b). The relative horizontal positions of the dies can be adjusted as desired. The width of the steel plate to be crimped is defined from the horizontal position of the dies (L_{CR}) and depends on the plate thickness and the maximum load capacity F_{CR} of the press (Fig. 4.1(b)).

4.2.2 U-ing phase

Upon completion of the crimping step, the steel plate proceeds to the U-ing phase described in Fig. 4.2. The U-ing step is performed in two stages. During the first stage, the U-punch moves downwards and bends the entire plate through a three-point bending process. The U-punch radius is selected so that the lower half of the steel plate acquires a radius close to the desired pipe radius at the end of the step. The U-punch stops moving when the plate touches the anvil. The U-punch is then held in place, and the side rollers move inwards approaching one another. The horizontal position (h_r) where the side rollers are placed and the distance (δ_r) they cover are selected so that the final form of the plate to be close to a "U" shape and the two branches of the plate are nearly vertically positioned.

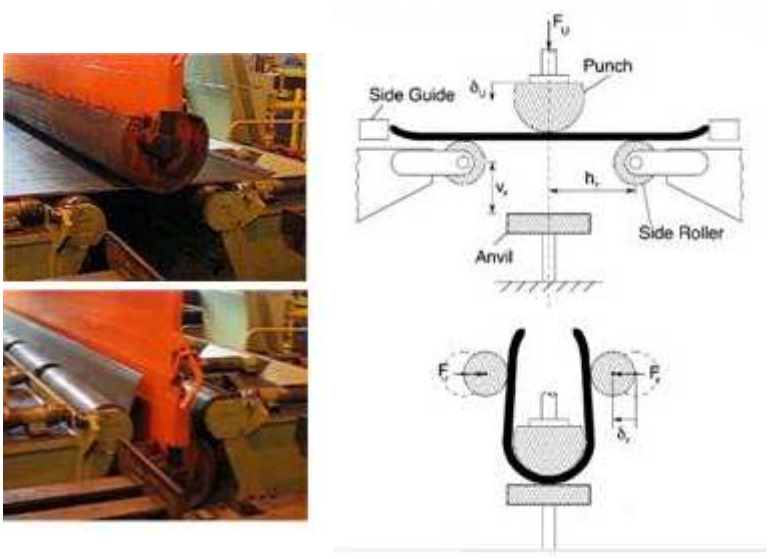

(a) (b)

Figure 4.2: The U-ing phase is realized with the displacement of the U-punch, the displacement of the side rollers and the unloading of the steel; (a) Representative picture of U-ing [Toscano et al. (2008)] (b) Schematic representation of U-ing process.

[Herynk et al. (2007)]

4.2.3 O-ing phase

Subsequently the plate is conveyed in the O-ing phase, which is realized by the approach of two semi-circular rigid dies with radius ρ_0. The upper die is pushed

downwards, forcing the plate to acquire a circular form (Fig. 4.3). The forming ends when the O-die covers the predefined displacement. After the O-ing phase the two edges of the pipe already beveled from the initial phase are welded together with SAW (Submerged Arc Welding), first on the inside and then on the outside (Fig. 4.4). At this stage, extensive ultrasonic checks are also performed to detect any weld defects prior to the pipe expansion.

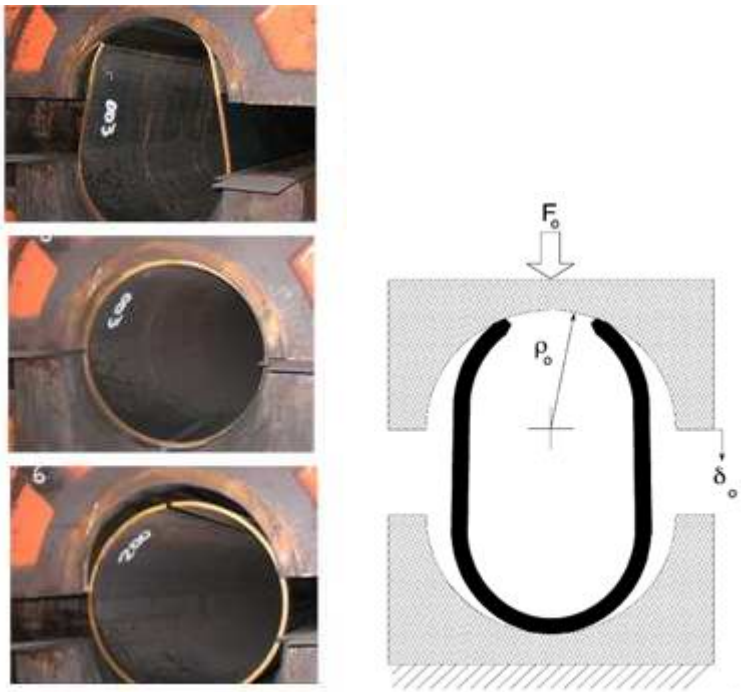

(a) (b)

Figure 4.3: The O-ing phase where the semi-circular die moves downwards until it touches the other die to facilitate the welding of the two beveled edges; (a) Representative picture of this phase [Toscano et al. (2008)] (b) Schematic representation of O-press.

[Herynk et al. (2007)]

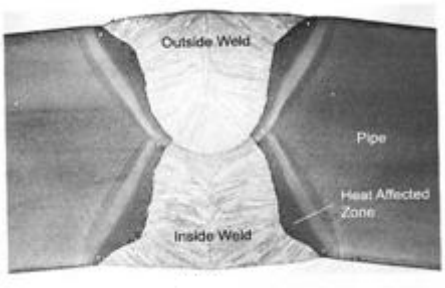

Figure 4.4: Welding metallography at the top edge of the plate.

[Kyriakides and Corona (2007)].

4.2.4 Expansion phase

The final step of the forming process consists of the pipe expansion. This step is necessary to control the shape of the pipe cross-section so that welding (girth welds) between adjacent pipe segments is performed without significant misalignment. Furthermore the expansion improves the roundness of the pipe giving, and provides its final size, improving its structural performance in terms of ultimate buckling pressure. The step is realized using a mandrel which is inserted in the pipe (Fig. 4.5). The mandrel usually consists of 8, 10 or 12 segments. In the model 8 segments were assumed in the circumference of the pipe. These segments are selected so that their radii (ρ_E) to be almost equal to the internal radius of the pipe. The mandrel is hydraulically actuated and all the segments move outwards radially. The distance covered by the segments depends on the plate thickness and constitutes a basic parameter of the manufacturing process.

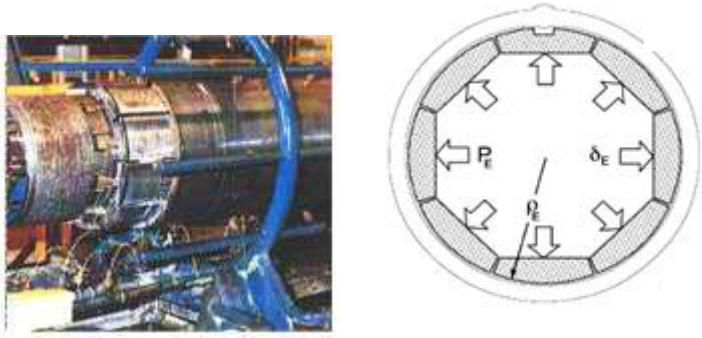

(a) (b)

Figure 4.5: Pipe expansion

(a) Representative picture of the expansion phase [Toscano et al. (2008)],

(b) Schematic representation of expansion. [Herynk et al. (2007)].

4.3 Numerical modeling of the UOE process and external pressure behavior

The simulation of the UOE forming process is conducted with finite element simulation aimed primarily at computing the stress (residual stresses) and strain (initial imperfections, initial ovalization) field at the end of the forming process. The second purpose of this numerical simulation is the examination of the pipe performance and ultimate strength under external pressure.

For this numerical simulation, a two-dimensional model is used and plane strain conditions are assumed. Taking advantage of the symmetry of the problem, only the half cross-section of the pipe is examined. The simulation is realized through the ABAQUS finite element software. For the discretization of the deformable plate, linear reduced-integration plane-strain continuum finite elements are used (CPE4R). A displacement-controlled algorithm is used for simulating the forming process, while the Riks algorithm is employed for applying external pressure.

The material behavior under reverse or cyclic loading is of major importance for the accurate simulation of the UOE process, as well as for the reliable prediction of

the buckling strength under external pressure. The reverse loading of the base metal in the plastic range is characterized by a “rounded” stress-strain curve due to the Bauschinger effect. In the present study a von Mises plasticity model is employed and the isotropic and linear kinematic hardening rules are considered first. These are the most commonly used hardening rules and in the present study their results are used as reference. The stress-strain material curves of those two simple models together with test data are shown in Fig.4.6. The two hardening rules considered are expected to provide an upper and a lower bound for the maximum pressure capacity of the pipe cross-section. However, it should be noted that both hardening rules are not accurate in predicting the onset of yielding in reverse loading. To improve the ability of the present model to predict the structural performance of the UOE pipe, the Armstrong – Frederick model that uses the non-linear Kinematic hardening rule is also considered and its predictions are compared with the predictions of other models.

Three different parameter sets are introduced for the Armstrong – Frederick model. In the first set (denoted as NLKH1) no isotropic hardening of the model is assumed. In the other two sets, the non linear Kinematic hardening parameters C and γ are combined with data pairs of the size of the yield surface k with respect to the equivalent plastic strain ε_q. These pairs define the isotropic hardening part of the model. Finally, the initial size of the yield surface k is assumed higher in the parameter set NLKH3. All the set parameters are reported in Table 4.1 and they are inserted as input in the so called “Non linear Kinematic/Isotropic hardening model”, of the general-purpose finite element software ABAQUS.

	NLKH1	**NLKH2**	**NLKH3**
k (MPa)	350	450	450
C (MPa)	3000	3500	900
γ	150	50	10
$\left(k(\varepsilon_{qi}),\ \varepsilon_{qi}\right)$	-	(450, 0)	(450, 0)
	-	(474, 0.07)	(500, 0.07)
	-	-	(550, 0.1)

Table 4.1. : Material parameter sets used for the numerical simulation

For better comparison with the experimental stress-strain curve, a more elaborate plasticity model, possibly based on the bounding surface theory, would be more suitable for the purpose of the present simulations. Such a model was employed by Herynk et al. (2007) through an in-house user subroutine in ABAQUS. The experimental uniaxial stress strain curve reported by Herynk et al. (2007) is compared with the predictions provided by the isotropic hardening model and the kinematic hardening model in Fig.4.6, while in Fig. 4.7the predictions of the Armstrong – Frederick model for the three different parameter sets are shown.

In Fig. 4.7 the Armstrong – Frederick model predictions are slightly different in the first loading part of the curve, but seem to be closer to the ones by Herynk et al. (2007) when reverse loading takes place. In this part of the curve, parameter sets

NLKH1 and NLKH2 provide a smooth transition from the elastic to the plastic region but after extended plastic deformation they predict an almost zero hardening modulus shown as a horizontal plateau in the curve. On the contrary, the parameter set NLKH3 is not as accurate as the other two when predicting the smooth transition, but it provides a constant hardening modulus when extended plastic deformation takes place. The effect of these differences on the UOE process simulation and the structural performance of the pipe will be discussed in the following sections.

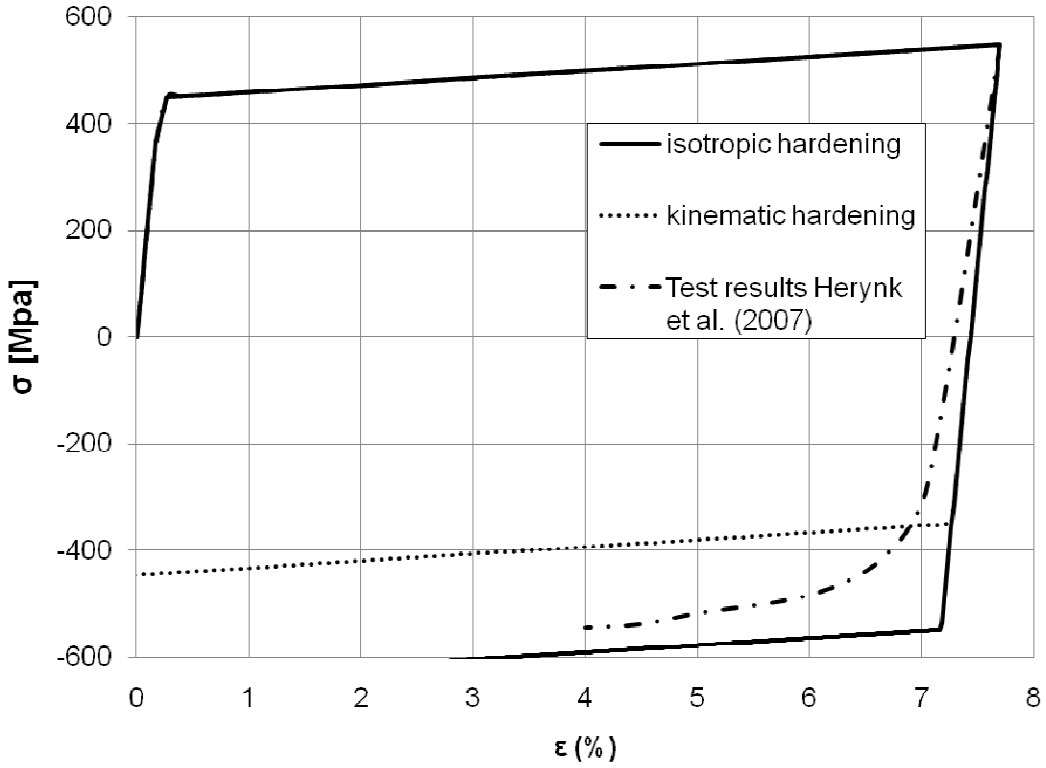

Figure 4.6: Material modeling, uniaxial stress – strain curve. The Isotropic and Kinematic hardening rule.

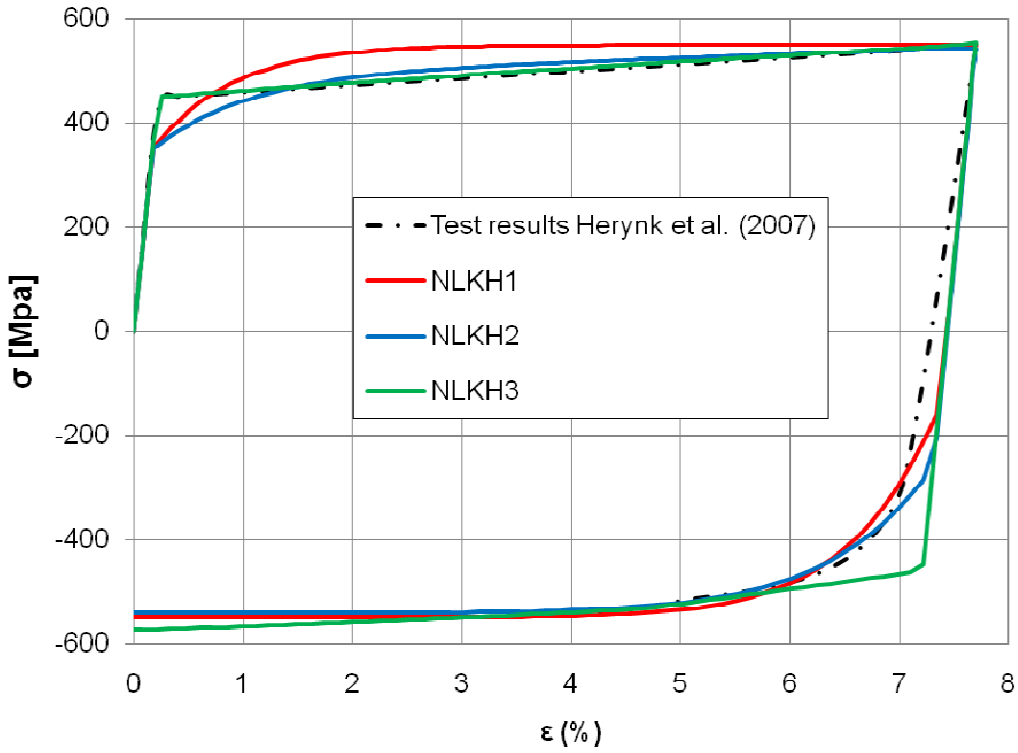

Figure 4.7: Material modeling, uniaxial stress – strain curve. The Armstrong – Frederick model.

An interesting aspect of the numerical simulation is the modeling of the forming dies. Herein, the dies are modeled as analytical rigid surfaces, as opposed to the deformable steel plate. For the interaction between the surfaces a "master-slave" type algorithm is adopted, where the rigid surfaces are the "master" surfaces and the deformable surfaces of the steel plate are the "slave" surfaces in a contact pair. These contact pairs are allowed to slide without friction. An exception to that is the contact pair between the U-punch and the upper part of the steel plate located in the lowest cross-section. For this contact pair a "no-separation" ("hard" contact) type is used to prevent the relative displacement between the two surfaces. In such a way, the steel plate is prevented from sliding from the U-punch as it moves downwards. In every step, all the "active" and "inactive" bodies are defined using the appropriate commands. This is necessary because in each step of the forming process certain bodies are used/acted (active) while others are neglected (inactive).

For simulating the welding procedure and in order to avoid adding new elements to the model, an additional material in the bevel of the welding is assumed in the initial geometry. This material is considered to have a low Young's modulus (equal to about 0.5% of the Young's modulus assumed in the rest part of the steel plate) and does not affect the UOE process until the O phase (Fig. 4.4). At the welding stage, the properties of this material are replaced with the same material properties of the rest steel plate. The welding part is discretized using CPE3 linear, three-node finite elements.

4.3.1 Numerical parametric study

The developed numerical model described in the previous paragraph is utilized to study a pipe of 609.6 mm external nominal diameter (24 in) and 32.3 mm wall thickness (1.273 in). The material of the plate was assumed to have a Young modulus E=210 GPa, a yield stress σ_y =448.5 MPa (65 ksi) (API X65 steel grade) and a Poisson ratio ν =0.3. The material model adopted for this analysis is von Mises plasticity with hardening laws. The hardening laws examined here is the isotropic, Kinematic and non linear kinematic/Isotropic hardening law (Armstrong – Frederick model). All the forming parameters considered are reported in Table 4.2, which are similar to the ones considered in the work of Herynk et al. (2007).

	Symbol	Description	Value
Plate	t	Plate thickness (mm)	32.33
	W	Plate width (mm)	1803
	X	Steel grade (Mpa)	448.5
Crimping	ρ_{CRi}	Internal crimping radius (mm)	265.4
	ρ_{CRo}	External crimping radius (mm)	298.5
	δ_{CR}	Final distance of the 2 dies (mm)	0.5
	L_{CR}	Horizontal distance of the dies (mm)	676.7
	h_{CR}	Height of the external crimping die (mm)	150
U-ing	ρ_U	U-Punch radius (mm)	246.4
	δ_U	Distance covered by the U-Punch (mm)	724
	δ_r	Distance covered by the Roller (mm)	102
	h_r	Horizontal Roller position (mm)	457
	υ_r	Vertical position of the Anvil (mm)	724
O-ing	ρ_O	Radius of the semi-circular dies (mm)	303.8
	δ_O	Distance covered by the O-die (mm)	218.55
Expansion	ρ_E	Mandrel radius (mm)	260
	δ_E	Expansion value (mm)	11
	N_E	Mandrel segments	8

Table 4.2: Characteristics of the UOE numerical simulation. Herynk et al. (2007).

In the numerical simulation, expansion takes place in three stages. During the initial stage the mandrels move outwards radially until there is a first contact with the plate's interior edge. This distance is denoted as δ_0 . Then the mandrels continue to move radially for an additional displacement δ_1 until they are all in contact with the pipe. During the second stage mainly bending of the steel plate takes place so that the plate accommodate itself around the mandrels, so that not much permanent strain is induced. The Expansion phase is completed with the application of an additional radial displacement $u_{Expansion}$ of the mandrels. At that stage, the force on the mandrels required for further displacement increases fast. The basic

parameter examined in our analysis is the additional expansion value $u_{Expansion}$ at the final (third) stage of the forming process. Particularly, in the present case different expansion values $u_{Expansion}$ are examined ranging from zero to 15 mm, beyond which severe plastic deformations of the pipe takes place. Therefore the following expression is valid for the total mandrel displacement u_{Tot} :

$$u_{Tot} = \delta_0 + \delta_1 + u_{Expansion} \tag{4.1}$$

The ovalization parameter Δ_0 is defined at the end of the expansion stage as a measure of the initial pipe geometric imperfection:

$$\Delta_0 = \frac{|D_1 - D_2|}{D_1 + D_2} \tag{4.2}$$

where D_1 and D_2 are values for the horizontal and vertical outer diameters correspondingly, measured at the end of the O-phase right after the unloading of the pipe. These two diameters are different since the pipe is not in a perfect cyclic shape.

In addition, the mean thickness of the pipe t_m is defined using the finite element results at three different characteristic locations:

$$t_m = \frac{t_1 + t_2 + t_3}{3} \tag{4.3}$$

In the above expression t_1 is the pipe thickness on the top part of the pipe cross-section (near the weld), t_2 is the pipe thickness on the middle height of the pipe cross-section and t_3 is the pipe thickness on its lower part, as shown in Fig. 4.8. To quantify variations of thickness around the pipe cross-section, a non dimensional imperfection parameter ΔT is introduced, which expresses the mean variation of the circumferential pipe- wall thickness:

$$\Delta T = \frac{t_{\max} - t_{\min}}{t_m} \tag{4.4}$$

where $t_{\max}$ refers to the maximum value and $t_{\min}$ refers to the minimum value of the pipe- wall thickness derived from t_1, t_2, t_3. Finally the UOE process induced permanent strain ε_E is defined as follows:

$$\varepsilon_E = \frac{C_E - C_O}{C_O} \tag{4.6}$$

where C_E and C_O are respectively the mid surface circumference after the Expansion and after the O-ing phase respectively.

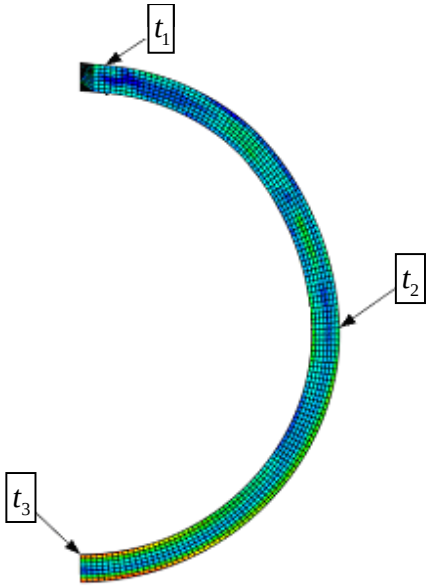

Figure 4.8: Part of the pipe ring where t_1, t_2 and t_3 are defined.

The UOE process simulation is examined using both the isotropic and kinematic (linear and nonlinear) hardening rules. The two hardening rules are associated with different values for the parameters introduced and their variation. For the isotropic hardening rule the parameters δ_0 and δ_1 are equal to 2.05 mm and 6 mm respectively, while for the linear kinematic hardening rule the parameters are equal to 0 mm and 5.86 mm respectively. When the nonlinear kinematic hardening rule is adopted the corresponding values are close to 2.5 mm and 6 mm respectively for all the parameter sets used.

In Fig. 4.9 the effect of the additional expansion $u_{Expansion}$ to the final circular cross-section is presented. It is observed that as the value of $u_{Expansion}$ grows, the final pipes have less ovalization initial imperfections. The results presented in Fig. 4.10 show the influence of the expansion phase on the circumferential pipe-wall thickness variation ΔT. In Fig. 4.11 the relation between the $u_{Expansion}$ value and the permanent induced strain is depicted. In those three figures the predictions of the nonlinear kinematic hardening rule adopting the NLKH2 parameter set are presented along with the predictions of the isotropic and linear kinematic hardening rule. In general, all the hardening rules show the same trend of the predicted behavior but they predict different values for each parameter examined.

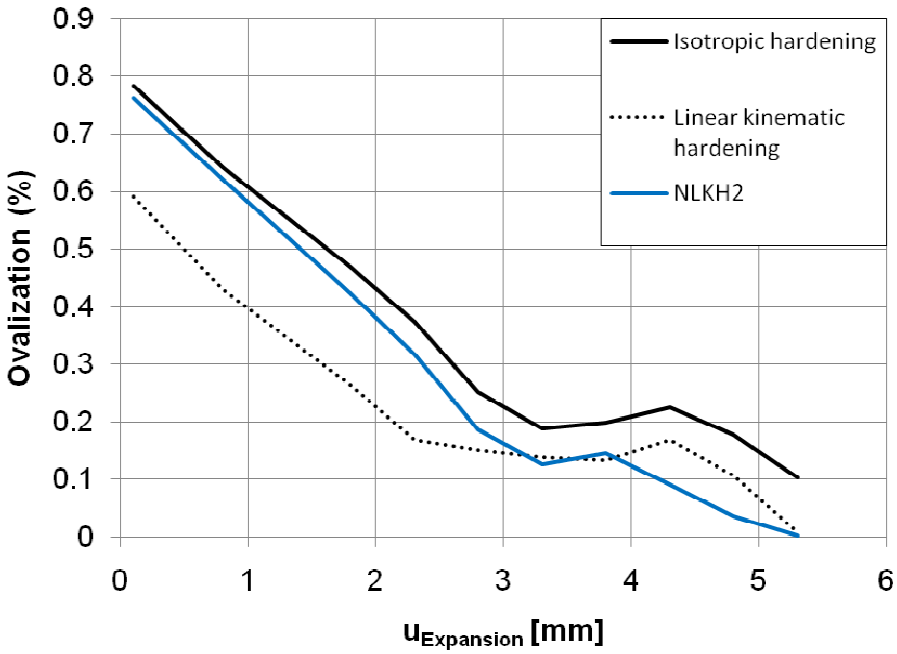

Figure 4.9: Effect of the expansion value $u_{Expansion}$ to the value of the initial ovalization imperfection of the formed pipe.

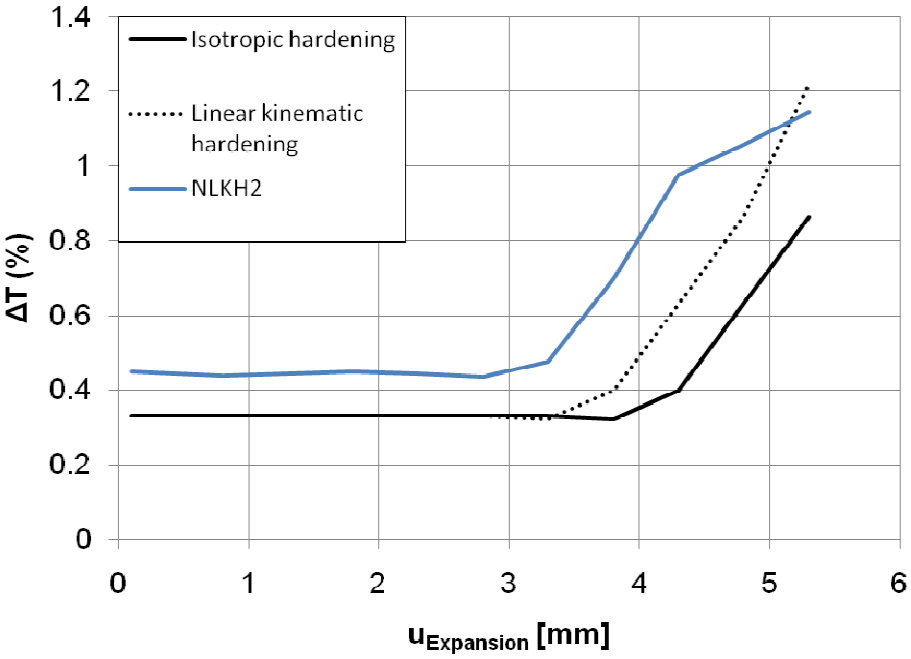

Figure 4.10: Effect of the expansion value $u_{Expansion}$ to the thickness imperfection of the formed pipe.

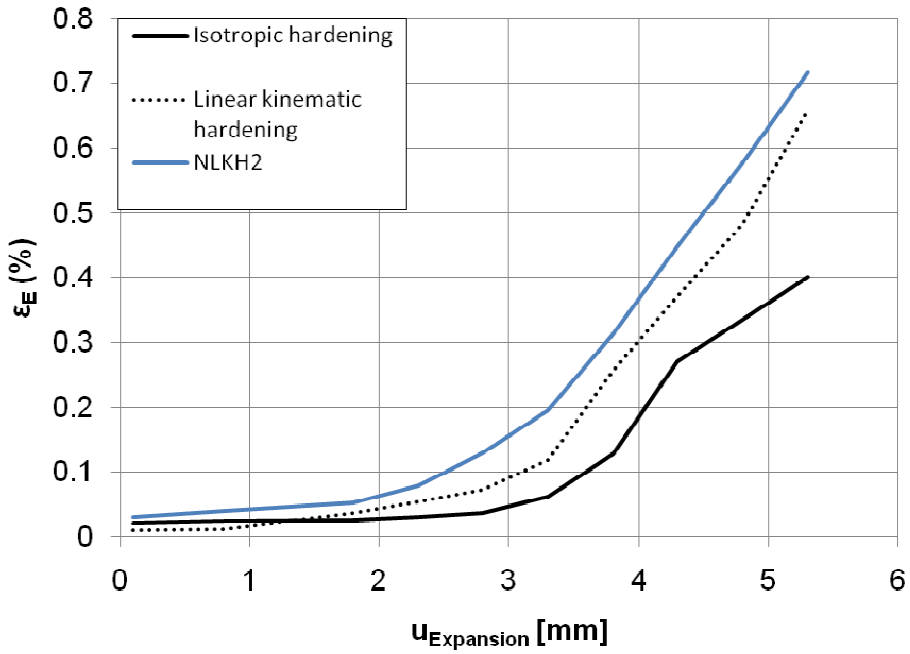

Figure 4.11: The relation between the expansion value $u_{Expansion}$ and the induced permanent strain ε_E of the formed pipe.

Fig. 4.10 shows that there is a significant change in the ΔT thickness parameter after the expansion value of 4 mm. This is due to the decrease of the pipe wall thickness near the welding area (C.P.1). From the three graphs above it is concluded that there is an optimum value for the expansion value during the last step of the forming process, for which there is an optimum combination of minimum ovalization of the cross-section and minimum variation of the pipe-wall thickness. For the specific geometry under examination for both the isotropic hardening rule and the kinematic hardening rule, this $u_{Expansion}$ value is approximately in the range of 3.5-4 mm. For the nonlinear kinematic hardening rule, the corresponding optimum $u_{Expansion}$ value is slightly less in the range of 3-3.5 mm.

Finally, it is also noted that by using numerical simulation it is possible to determine the residual stresses after the end of the process in each point of the pipe with significant precision. The stress distribution is dependent on the hardening rule used as well.

4.3.2 Mechanical behavior during the UOE process and external pressure application

During the forming process the material experiences deformations far in the plastic range. The magnitudes of plastic deformations as well as the resulting stresses are the key feature for the collapse pressure resistance of the pipe. In the following paragraphs the UOE process resulting stress – strain path will be discussed in detail for each forming step. Three check points (C.P.) are introduced in the areas where the maximum stresses are expected to occur (Fig. 4.12). At each C.P. both the internal and external side of the plate is examined. The numerical simulation of the UOE process is presented in Fig. 4.14.

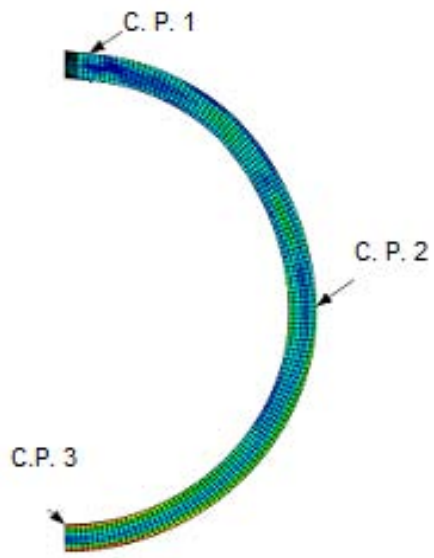

Figure 4.12: The Check Points on the half pipe section

During the Crimping phase of the UOE process, all the plastic deformation is located near the edges as expected (C.P.1). The material undergoes plastic deformations until the desired curvature of the plate is achieved. The rest part of the plate remains in a low stress state (Fig. 4.14(a)).

The U-ing phase stresses the areas located near C.P.2 and C.P.3. In particular, near the C.P.3 the material is highly stressed beyond the elastic limit when the U-punch moves downwards at the beginning of the phase. The area near the C.P.2 also experiences stresses in a lower degree. The parts of the plate away from C.P.2, C.P.3 remain nearly unaffected. The U-ing phase is completed with the horizontal movement of the rollers. This step actuates the areas near the C.P.2, while the areas near the C.P.1 and C. P.3 remain in the same stress state as before (Fig.4.14(b)).

The O-ing phase results in a major change of the plate shape. The locus of the maximum stresses that develop in the plate moves gradually from the vicinity of the C.P.3 towards the C.P.2 and near the C.P.1 at the end of the phase. This phase is crucial for the stress state of the material located near C.P.1 and C.P.2 (Fig. 4.14(c)).

The final phase of the UOE process is the Expansion phase. Up to this point, the most stressed areas of the pipe are near the C.P.1 and C.P.3. Due to the expansion, all the compressive stresses that have developed in the inner part of the pipe throughout the forming history are relieved while in the exterior part of the pipe, which is already in tension, additional tensile stresses are developed. Depending on the $u_{Expansion}$ value, the influence of this phase on the residual stress field of the pipe at the end of the UOE process can be the determining parameter for the pipe resistance against external pressure (Fig. 4.14(d). This issue will be discussed in the following.

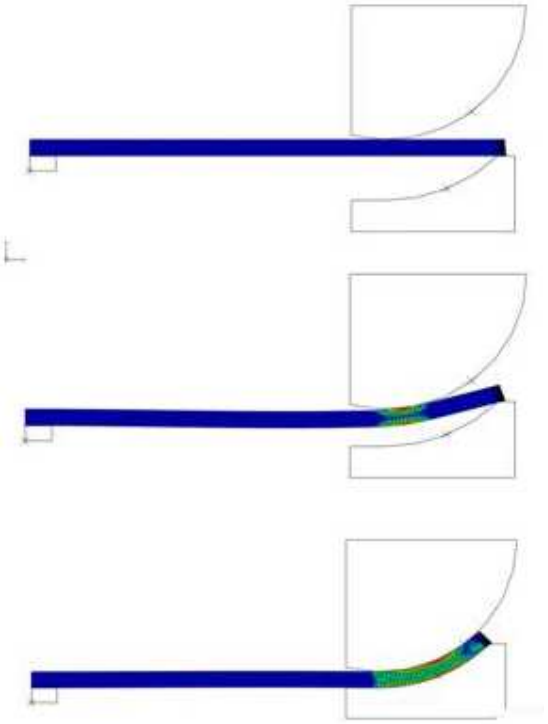

(a)

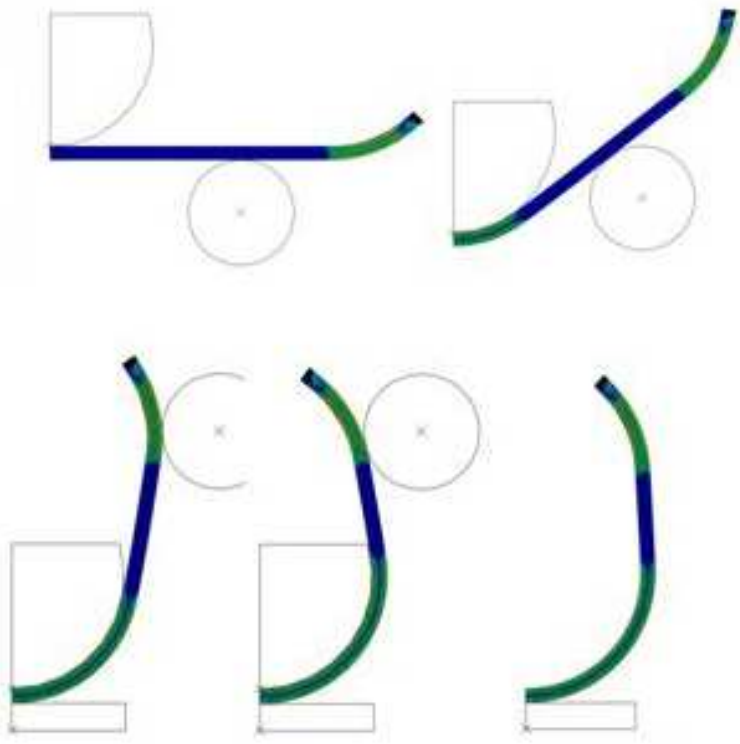

(b)

Figure 4.13: The numerical simulation of the UOE process.
(a) Crimping phase, (b) U-ing phase

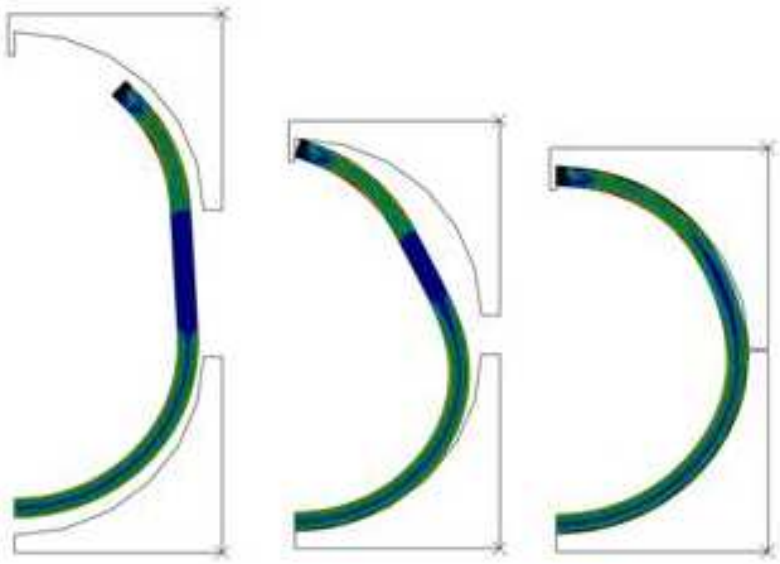

(c)

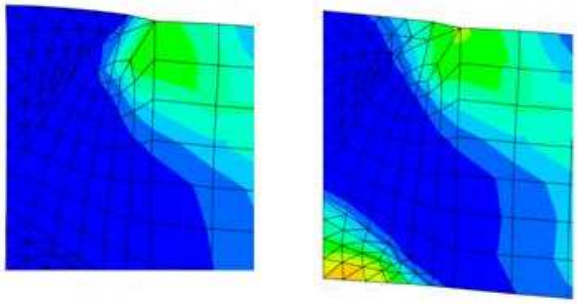

(d)

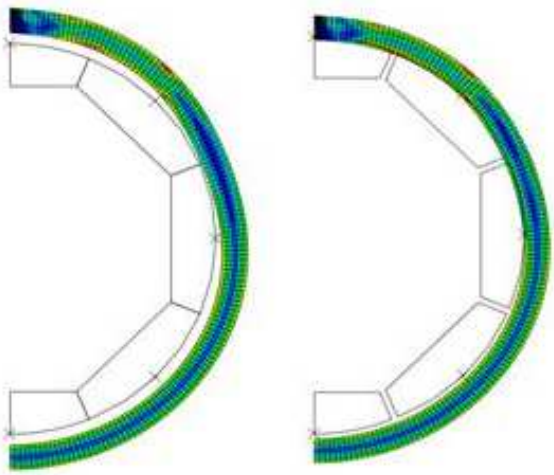

(e)

Figure 4.14 (continued): The numerical simulation of the UOE process.

(c) O-ing phase, (d) Welding, (e) Expansion phase

The residual stress/ residual strain field at the end of the UOE process is the starting point for the stress – strain field that will result from the application of the

external pressure. At the end of the pipe manufacturing process the material in the C.P.1 area is more plastified from the initial crimping phase. In the other parts of the pipe, the distribution of the plasticity is almost uniform and it is located at the interior and exterior part of the pipe as expected. The application of the external pressure results in the simultaneous increment of the stresses in all three check points as the pipe transforms from its circular shape to a (O) shape. In Figures 4.15, 4.16, 4.17 the total stress – strain path prediction resulting from the Isotropic and the Kinematic hardening model is presented. In these graphs both the exterior and the interior part of the plate at each check point are examined. All graphs refer to an expansion value $u_{Expansion}$ of 0.1 mm ($u_{Tot} = 8.3\,\text{mm}$). In Fig. 4.16 and Fig. 4.17 the corresponding part of the stress – strain curve for the C.P.2 and C.P.3 for each UOE phase is presented.

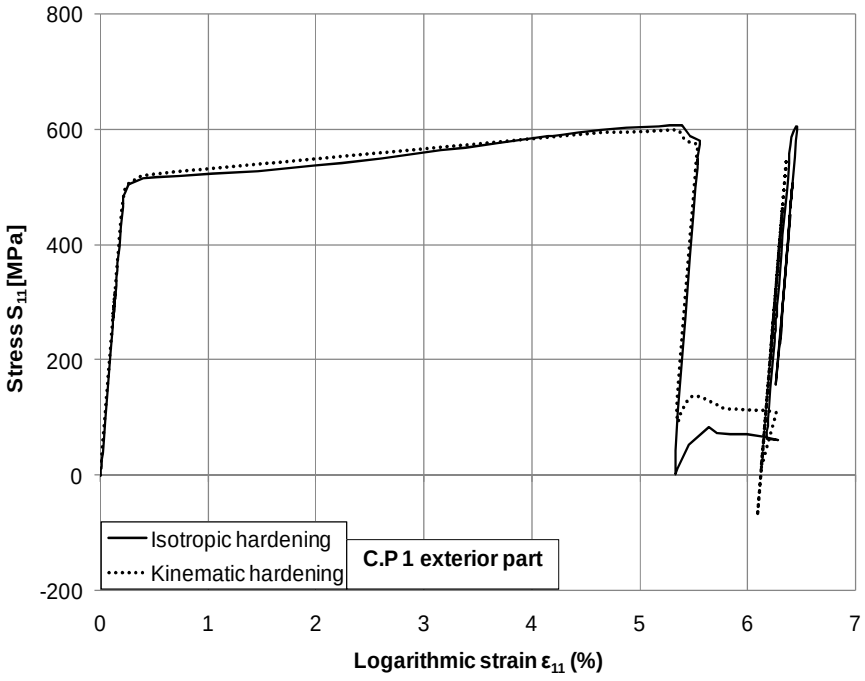

(a)

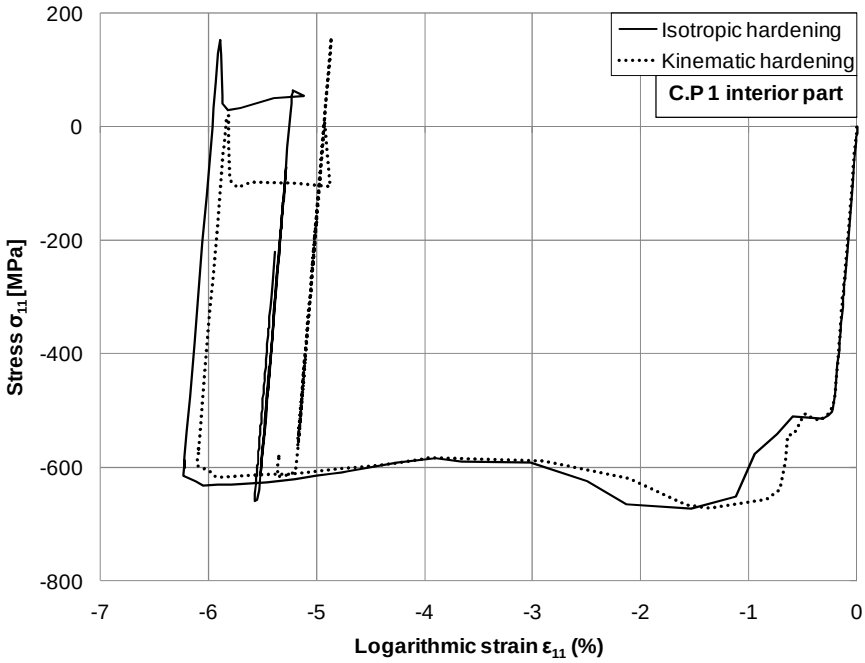

(b)

Figure 4.15: The stress strain path for the C.P.1: (a) outer surface, (b) inner surface.

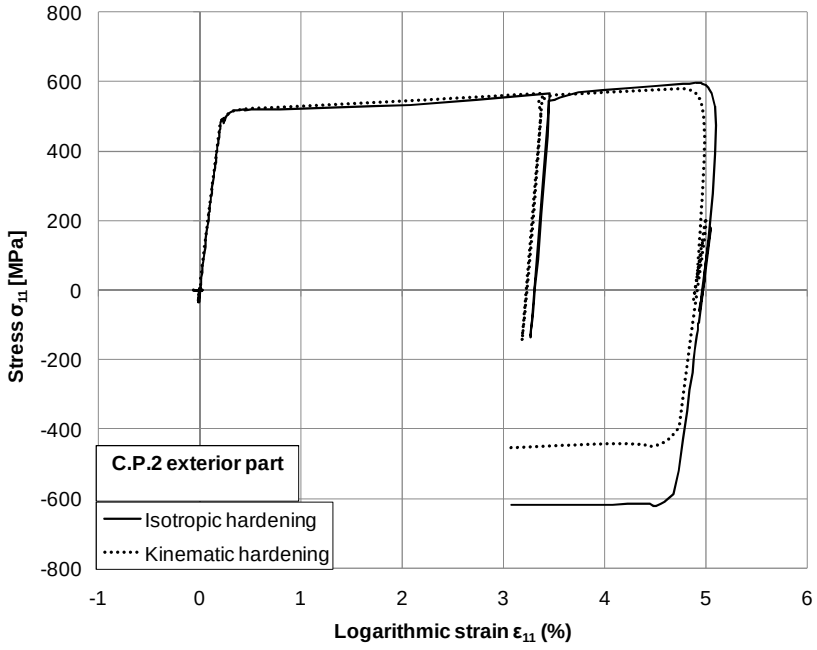

(a)

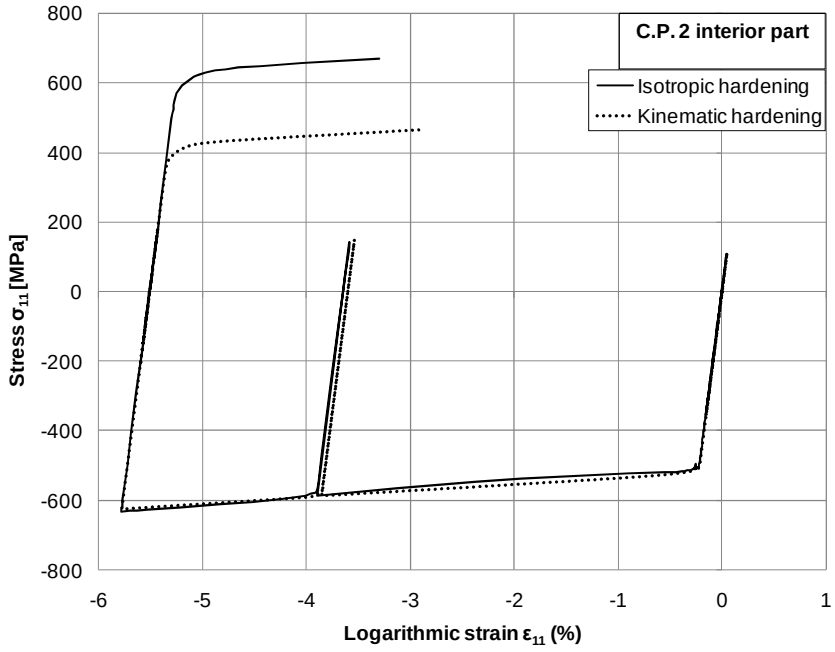

(b)

Figure 4.16: The stress strain path for the C.P.2: (a) outer surface, (b) inner surface.

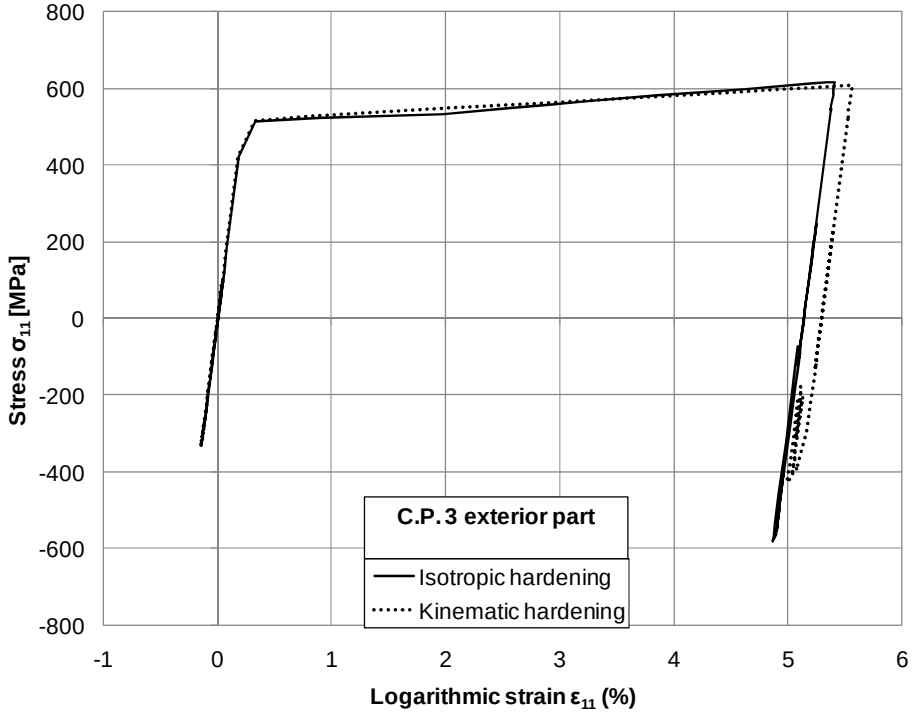

(a)

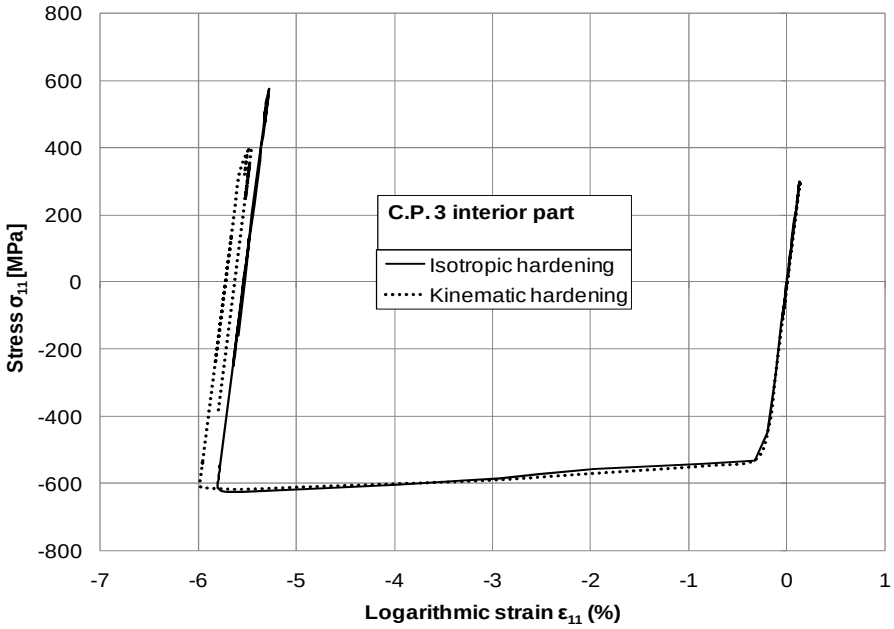

(b)

Figure 4.17: The stress strain path for the C.P.3: (a) outer surface, (b) inner surface.

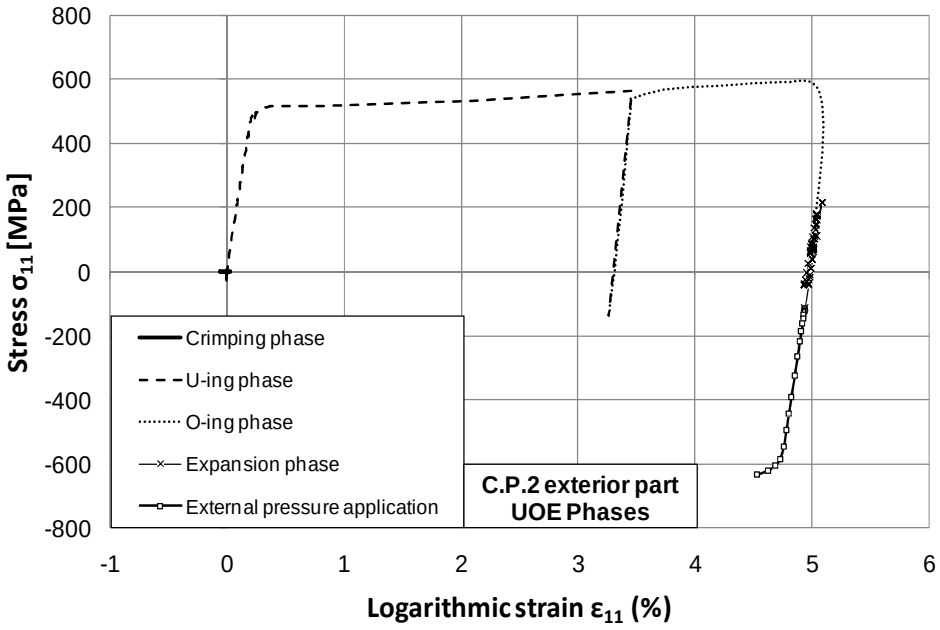

(a)

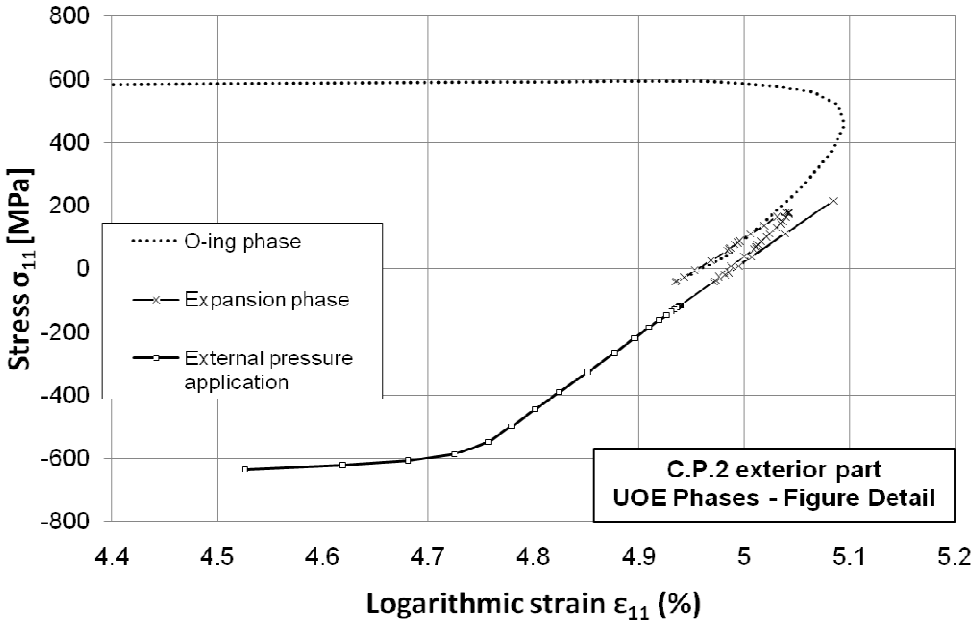

(b)

Figure 4.18: (a) The UOE phases stress – strain curve for the C.P.2 (Isotropic hardening),

(b) Graph Detail

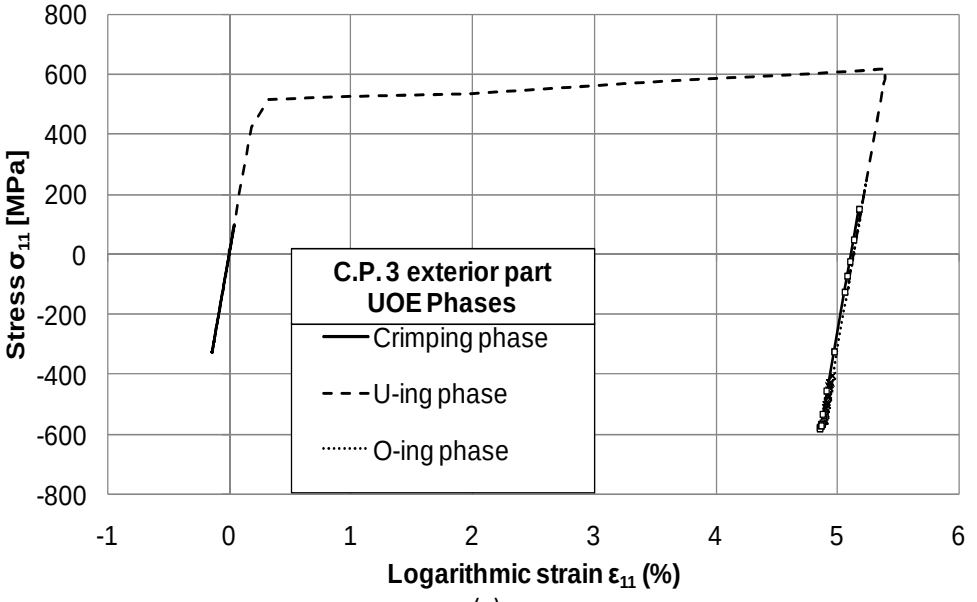

(a)

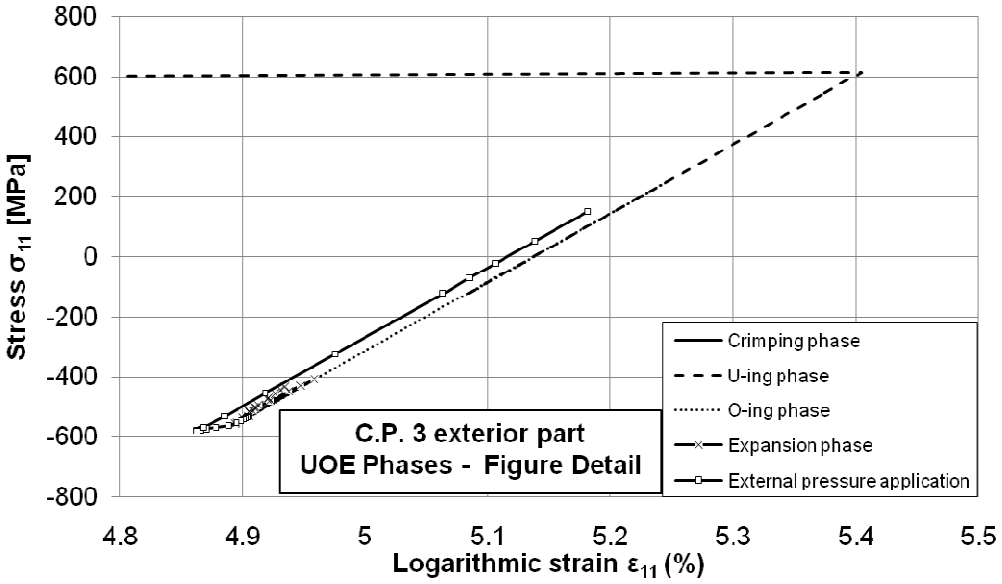

(b)

Figure 4.19: (a) The UOE phases stress – strain curve for the C.P.3 (Isotropic hardening), (b) Graph Detail

For comparison reasons, in Fig. 4.15, 4.16, 4.17 the results of the same problem with the adoption of the Kinematic hardening rule are also depicted along the results of the Isotropic hardening rule. The two different hardening rules predict different stress-strain paths especially when reverse loading takes place. In such cases, the Isotropic hardening rule over-predicts the yield initiation. The point predicted has the same stress value as the corresponding point having the maximum stress value in the monotonic branch of the curve. On the contrary, the residual stresses and strains affect the predictions of the Kinematic hardening rule. Therefore, according to this rule in the case of reverse loading the yielding starts earlier. The most vulnerable area of the steel pipe seem to be the area in the vicinity of the C.P.2 where reverse loading appears and the loading continues far towards the opposite direction during the external pressure application phase.

4.3.3 The effect of the UOE process on the collapse pressure

The first main effect of the UOE process on the collapse pressure of the pipe is the resulting ovalization of the pipe cross – section. The geometry imperfection of the finished pipe is the governing parameter for a wide range of expansion values. As it has been already discussed, the UOE process also introduces residual stresses and plastic strains distributed along the circumference in a non uniform way. It has been demonstrated that during the U-ing and O-ing steps of the UOE process, the maximum stresses appear. Depending on the expansion value, the Expansion step reliefs a part of the induced stresses. The residual stress distribution after this step is the second major parameter affecting the collapse of the pipe under external pressure. In Fig. 4.20 and Fig. 4.21 the maximum collapse pressure (P_{max}) and the resulting ovalization parameter versus the average circumferential permanent stain

(ε_E) are depicted respectively. In Fig. 4.22 the shape change of the pipe under external pressure is presented.

The P_{max} - ε_E curves presented in Fig. 4.20 can be separated in three parts. The first part extends to values of ε_E up to 0.1 %. In this part, the maximum collapse pressure is very sensitive to the variation of the expansion value. The initial ovality of the pipe resulting from the manufacturing process acquires its highest values in this part as well (Fig. 4.21) and governs the behavior of the pipe. As the total mandrel displacement value increases from 0 mm (UO case) to 11.5 mm, the initial ovality is recovered quickly and this results to the ascending branch of the curve. The hardening rules used in the process simulation predict similar P_{max} values for a given expansion value but different induced permanent strains on the pipe. It is obvious though that the parameter sets NLKH1 and NLKH2 give very conservative predictions far from the range of the predicted P_{max} values given by the rest hardening rules. On the contrary, parameter set NLKH3 of the Armstrong – Frederick model predicts P_{max} values close to the values predicted by the Kinematic hardening rule.

The second part of the curve extends to values of ε_E up to 0.4 %. This part of the curve is characterized by an almost constant value of P_{max} regardless the expansion value and the induced strain. In addition, at this part of the curve the ovality variation is minimized (Fig. 4.20, 4.21). This observation leads to the conclusion that the geometric ovalization parameter is mainly affecting the final behavior of the pipe. The hardening rules adopted for the analysis capture this constant behavior providing though different P_{max} values. Moreover, the Isotropic hardening rule results to an ascending branch after the value of ε_E = 0.27 %, which contradicts the predictions of the Kinematic hardening rule as well as the predictions given by Herynk et al. (2007). The parameter sets NLKH1 and NLKH2 of the Armstrong – Frederick model predict almost constant but very conservative P_{max} values, while the set NLKH3 predictions are very close to the predictions given by Herynk et al. (2007). At this range of induced strains, it can be stated that the hardening rules adopted define the accuracy of the P_{max} value prediction.

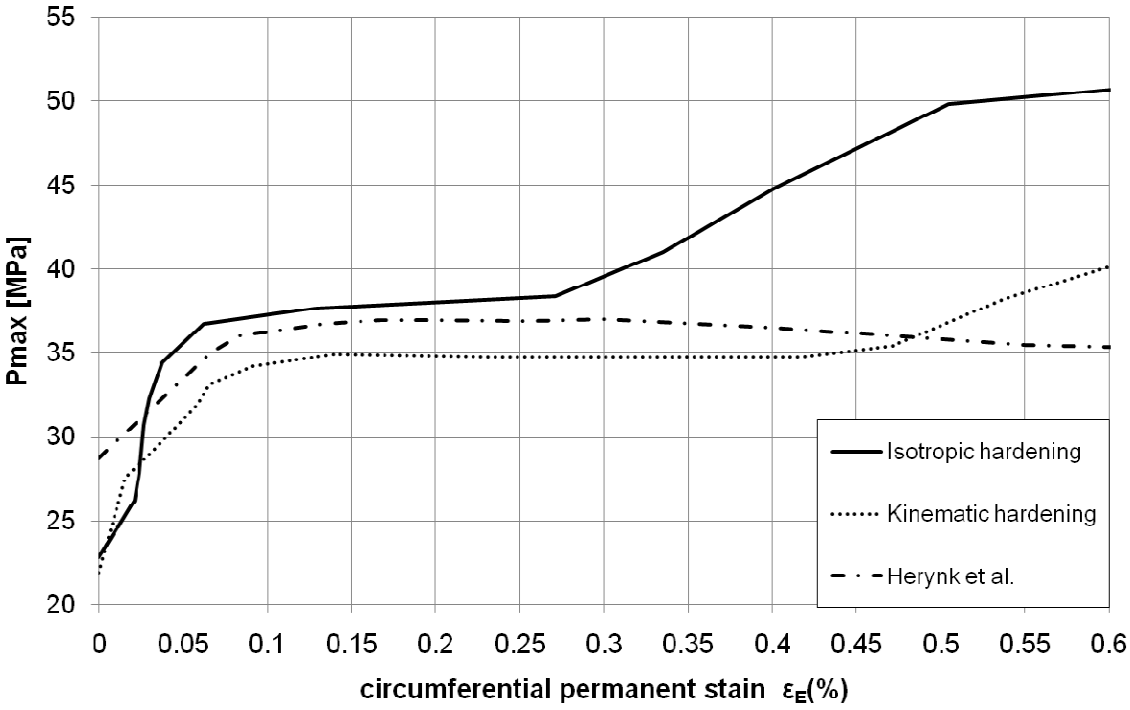

(a)

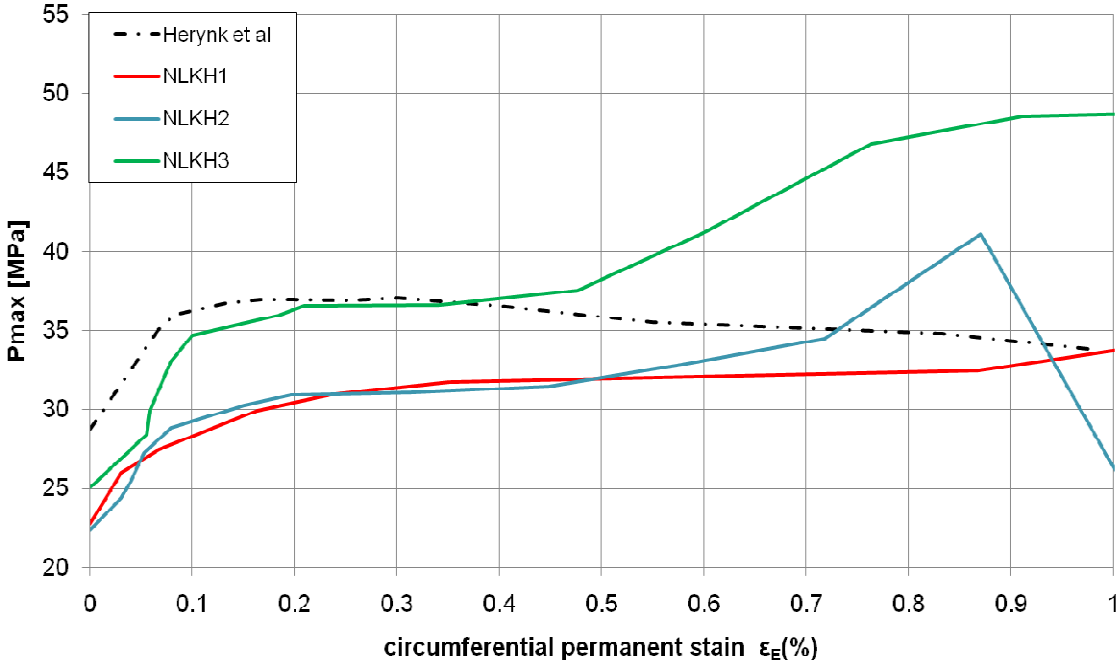

(b)

Figure 4.20: Collapse pressure – permanent strain curve: (a) The predictions of the Isotropic and Kinematic hardening rules, (b) The predictions of the Armstrong – Frederick model

The importance of the accurate description of the material behavior results also from the third part of the graph. There, the ovalization parameter is reaching its minimum value and therefore the hardening rule adopted should be the only parameter affecting the total behavior. After the value of ε_E equals to 0.3% a

descending branch starts according to Herynk et al. (2007). According to this analysis, a further increase of the induced strain has as a consequence the degradation of the compressive material properties affecting also the P_{max} value. Moreover, it was observed by Herynk et al. (2007) that the material acquires a reduced elastic modulus during the reverse loading (Fig. 4.6). None of the hardening rules used for the present study can predict such a behavior. The parameter set NLKH 1 of the Armstrong – Frederick model predictions are still at the same level, while the predictions of the parameter set NLKH2 show some instability. This is due to the different collapse modes it predicts. Finally, the predictions of the parameter set NLKH3 follow the predictions of the Kinematic hardening rule resulting in an ascending branch as well.

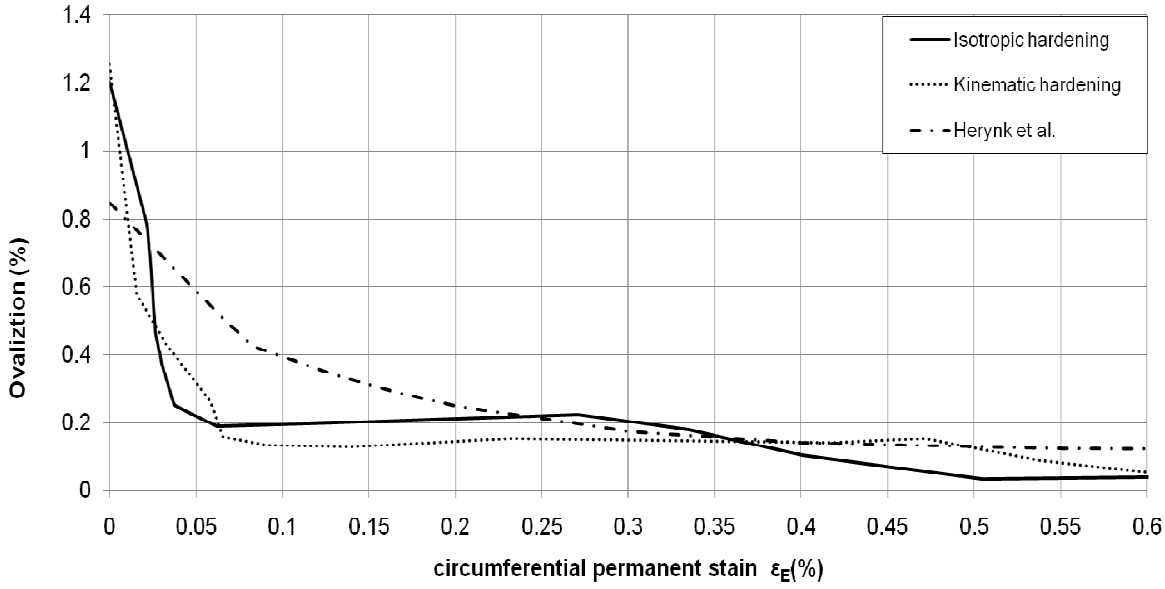

(a)

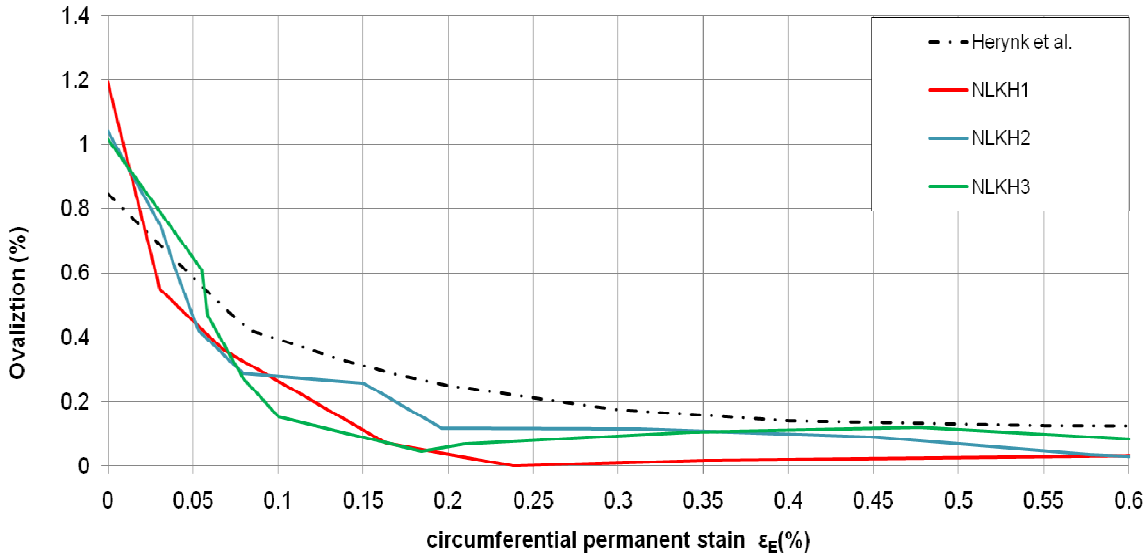

(b)

Figure 4.21: Ovalization parameter – permanent strain curve. (a) The predictions of the Isotropic and Kinematic hardening rules, (b) The predictions of the Armstrong – Frederick model

The reason for this difference in the predicted behavior is the incapability of the described hardening rules to take into account the Bauschinger effect and estimate the exact size of the yield surface at the same time. The Kinematic hardening rule provides safer estimations of the P_{max} value due to constant size of the yield surface adoption it is based on, while the model with the Isotropic hardening rule overestimates the P_{max} values by over predicting the size of the yield surface. The Armstrong – Frederick model exhibits different behavior depending on the parameter set it is based on. Nevertheless, the parameter set NLKH 3 seems suitable for good predictions of the collapse pressure for permanent induced strains up to 0.4 %.

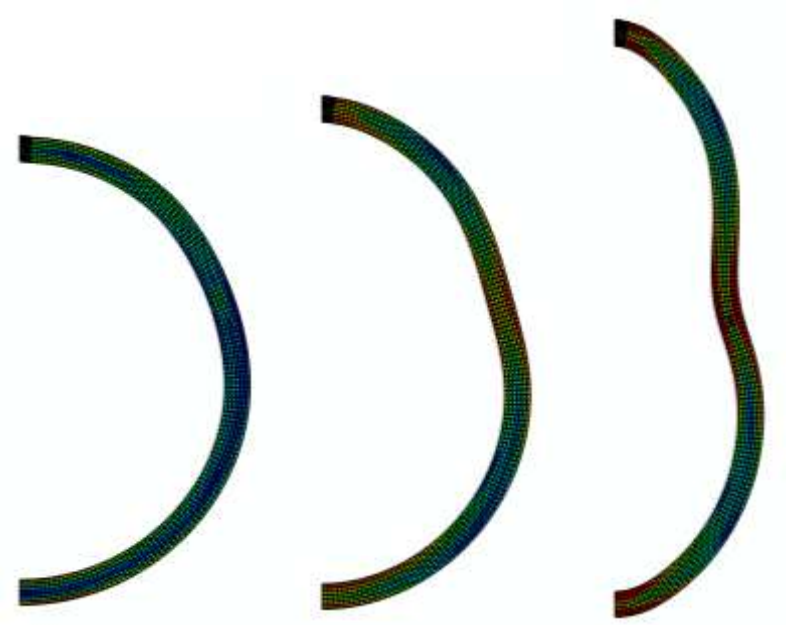

Figure 4.22: The shape change of the pipe under external pressure.

5. Summary - Conclusions

In the present work the Armstrong – Frederick (A-F) cyclic plasticity model is examined. The presentation of the model starts with a discussion of cyclic plasticity fundamentals in Chapter 1. The main characteristics of each plasticity model are presented. The hardening modulus and the way it is defined is the feature that leads to the categorization of the presented plasticity models to “coupled” and “uncoupled”. In “coupled” models the hardening modulus is defined through the consistency conditions, while in “uncoupled” models the hardening modulus is defined by a separate expression.

Before discussing the formulation of the A-F mode in Chapter 2, the plasticity model that adopts the von Mises description of the yield surface and the linear kinematic hardening rule is presented. The basic assumptions of the model and the model numerical implementation are discussed in detail. The introduction of the nonlinear kinematic hardening rule to the aforementioned plasticity model differentiates the equation formulation and constitutes the basis of the A-F model. The constitutive equations of the general formulation of the A-F model and their numerical implementation for plane-strain and plane-stress conditions are presented.

The model prediction capabilities are examined through cyclic loading examples. A thorough examination of the effect each model parameter has is presented. The A-F model provides better predictions compared to the linear kinematic hardening rule as far as the Bauschinger effect is concerned. Moreover, the cyclic hardening/softening of the material can be simulated through the isotropic hardening part of the model. Finally, the ratcheting phenomenon with varying evolution rate can be described effectively.

In Chapter 3 the behavior of pipes subjected to cyclic bending is examined. Cyclic bending is also combined with internal/external pressure. Generally, it is proved that the cyclic bending behavior of a pipe can be simulated with an acceptable accuracy using the A-F model.

The cyclic bending of internally pressurized pipes is examined through verification of the experimental results reported by Rahman et a. (2008). Two different finite element models (“slice” model, 3D model) are developed to simulate the described experiment. It is shown that the A-F model predictions are quite close to experimental measurements regardless the model adopted for the simulation. Additionally, when the 3D model is used, local instability effects can be also captured.

The pipe is made of the steel alloy 4130, whose material properties are derived through one-element cyclic material testing. This test is simulated using the linear kinematic hardening model and variations of the A-F model. When the A-F model is used, the steel alloy 4130 stable cyclic stress-strain curve is simulated with an increased accuracy compared to experimental measurements. Moreover, in the same chapter, uniaxial ratcheting experimental results are compared with numerical

simulations where the A-F model is used. It is shown that the isotropic hardening part of the model can improve the ratcheting predictions.

The cyclic bending of externally pressurized pipes is also discussed in Chapter 3. The simulations are conducted as curvature-controlled and moment-controlled problems using the "slice" model with the material parameters of steel alloy 4130. In the curvature-controlled simulations the "slice" finite element model adopting the A-F model predicts a rapid degradation of the pipe's bending capacity, which is not compatible with similar experimental observations.

Finally, the pure cyclic bending of pipes is also examined through curvature-controlled and moment-controlled simulations. The "slice" finite element model adopting the A-F model is employed and different loading ratios are examined. The degradation of the pipe's bending capacity as well as the ovalization evolution as the number of cycles increases can be captured by the A-F model. Moreover, in the case of unsymmetric moment-controlled simulations, the curvature evolution can be also predicted verifying in a qualitative way similar experimental measurements.

In Chapter 4 of the present study the UOE pipe forming process has been modeled with the use of robust computational tools. The study is aimed at the computation of the residual stresses and the initial imperfections of the formed pipe and afterwards the pipe's capacity against external pressure application. The geometrical characteristics of the pipe examined are reported in the work of Herynk et al. (2007). The material characteristics necessary for the numerical simulation are derived by simulating a uniaxial stress-strain curve reported in the same study. The von Mises plasticity model adopting the isotropic and linear kinematic hardening rule is employed along with the A-F model. The simulation with the A-F model can capture the Bauschinger effect significantly better compared to the simulation results of the rest plasticity models examined. At the end of the manufacturing process the residual stresses and initial imperfections of the pipe have been computed.

After the simulation of the manufacturing process, the pipe's external pressure capacity was calculated. It was observed that expansion of the pipe's cross-section leads to minimization of pipe out-of-roundness and improves the pressure capacity of the pipe; yet, large expansion values though lead to undesired pipe-wall thickness variations. The isotropic and kinematic hardening models can capture the general trend of pipe's behavior. Even if they provide different pressure capacity values, they are in good accordance with the predictions of the more elaborate model used by Herynk et al. (2007). The A-F model behavior is highly affected by the material parameters. Generally, it captures accurately enough the Bauschinger effect and predicts reasonable collapse pressure values.

It is believed that a more sophisticated material modeling possibly based on the "Bounding Surface" concept is necessary in order to make more accurate predictions of the maximum collapse pressure P_{max}. This model should be able to describe the actual material behavior under cyclic loading in the plastic range in an effective and robust way. Moreover, the Bauschinger effect as well as the exact size of the yield surface should be effectively predicted. Finally, a carefully designed set of experiments on material level as well as on full pipe scale level would help the calibration of all the adopted plasticity models and will provide essential information

about the actual behavior of such pipes. Nevertheless, the present simulation offers a powerful yet inexpensive tool for the UOE-manufactured pipe pressure capacity prediction which can be used for optimizing UOE manufacturing process.

References

ABAQUS v6.7 Documentation - Analysis User's Manual.

Ades, C.S., 1957. "Bending strength of tubing in the plastic range. J. Aeronaut. Sci. 24, 605-610.

Aravas, N., 1987. "On the numerical integration of a class of pressure-dependent plasticity models", International Journal for numerical methods in engineering 24, 1395-1416

Armstrong, P.J., Frederick, C.O., 1966. "A mathematical representation of the multiaxial Bauschinger effect", CEGB Report No. RD/B/N 731.

Axelrad, E.L., 1962. "Flexure and instability of thin-walled pressurized tubes". Izvestiya Akademii Nauk SSSR, Otdelenie Tekhnicheskikh Nauk, Mekhanika i Mashinostroenie 1, 98–114, in Russian.

Bari, S., Hassan, T., 2000. "Anatomy of coupled constitutive models for ratcheting simulation", International Journal o Plasticity 16, 381-409.

Bari, S., Hassan, T., 2001. "Kinematic hardening rules in uncoupled modeling for multiaxial ratcheting simulation", International Journal o Plasticity 17, 885-905.

Bauschinger, J. 1881. "Ueber die veraenderung der elasticitaetgenze und des elasticitaetmodulus verschiedener metalle", Civilingeneur 27, 289–348.

Besseling, J.F., 1958. "A theory of elastic, plastic and creep deformations of an initially isotropic material", Journal of Applied Mechanics 25, 529-536.

Chaboche, J.L., Dang-Van, K., Cordier, G.,1979. "Modelization of the strain memory effect on the cyclic hardening of 316 stainless steel", Proceedings of the 5th International Conference on SMiRT, Div. L, Berlin, Germany.

Chaboche, J.L., 1986. "Time-independent constitutive theories for cyclic plasticity", International Journal of Plasticity 2, 149-188.

Chang, K.H., Pan, W.F., Lee, K.L., 2008. "Mean moment effect on circular thin-walled tubes under cyclic bending". Structural Engineering and Mechanics, Vol. 28, No. 5, 495-514.

Chen, W.F. and Ross, D.A., 1977. "Tests on the fabricated tubular columns", *Journal of the Structural Division,* ASCE, Vol. 103 (3), pp. 619-634 19

Corona, E., Kyriakides, S., 1988. "On the collapse of inelastic tubes under combined bending and pressure". International Journal of Solids and Structures 24, 505–535.

Corona, E., Kyriakides, S., 1991. "An experimental investigation of the degradation and buckling of circular tubes under cyclic bending and external pressure". *Thin-Walled Structures*, *Volume 12, Issue 3*, *Pages 229-263*

Corona, E., Hassan, T., Kyriakides, S., 1996. “On the Performance of Kinematic Hardening Rules in Predicting a Class of Biaxial Ratcheting Histories”. International Journal of Plasticity, Vol. 12, pp. 117-145

Dafalias, Y.F., Popov, E.P., 1976. “Plastic internal variables formalism of cyclic plasticity”, Journal of Applied Mechanics 43, 645-650.

DeGeer, D., Timms, C., Lobanov, V., 2005. “Blue Stream Collapse Test Program”, *Proceedings of 24th International Conference on Offshore Mechanics and Arctic Engineering*, OMAE2005-67260, Halkidiki, Greece.

Drucker, D.C., Palgen, L., 1981. “On stress-strain relations suitable for cyclic and other loadings”, Journal of Applied Mechanics 48, 479-485.

Gellin, S., 1980. “The plastic buckling of long cylindrical shells under pure bending”. International Journal of Solids and Structures 10, 397–407.

Gresnigt, A.M., van Foeken, R.J., Chen, S., 2000, “Collapse of UOE Manufactured Steel Pipes”, Proceedings of the Teenth Intrnational Offshore and Polar Engineering Conference.

Guionnet, C., 1992. “Modeling of ratcheting in biaxial experiments”, Journal of Engineering Materials and Technology 114, 56-62.

Hassan, T., Kyriakides, S., 1992. “Ratcheting in cyclic plasticity, Part I:Uniaxial behavior”, International Journal of Plasticity, Vol.8, pp.91-116.

Herynk, M.D., Kyriakides, S., Onoufriou, A., Yun, H.D. , 2007. “Effects of the UOE /UOC pipe manufacturing processes on pipe collapse pressure”, *International Journal of Mechanical Sciences*, vol. 49, pp. 533–553.

Karamanos, S.A., 2002. “Bending instabilities of elastic tubes”. International Journal of Solids and Structures 39, 2059-2085.

Karamanos, S.A. and Tassoulas, J.L., 1991. ‘‘Stability of Inelastic Tubes Under External Pressure and Bending’’, *J. Engineering Mechanics*, ASCE, vol. 117, no. 12, pp. 2845-2861.

Karamanos, S. A., and Tassoulas, J.L., 1996, "Tubular Members I: Stability Analysis and Preliminary Results.", *Journal of Engineering Mechanics*, ASCE, Vol. 122, No. 1, pp.64-71.

Kyriakides, S., Shaw, P.K., 1982. “Response and stability of elastoplastic circular pipes under combined bending and external pressure”. International Journal of Solids and Structures 18 (11), 957–973.

Kyriakides, S., Corona, E., Fisher, F.J., 1992, “On the effect of the UOE manufacturing process on the collapse pressure of long tubes”, Offshore Technology Conference, OTC 6758

Kyriakides, S., and Ju, T. 1992. “Bifurcation and localization instabilities in cylindrical shells under bending – I. Experiments”. Int. J. Solids Structures, vol. 29, No. 9. pp. 1117-1142.

Kyriakides, S. and Corona, E., *Mechanics of offshore pipelines*, *Vol. I Buckling and Collapse*. Elsevier, 2007.

Langner, C.G., 1984. “Design of Deepwater Pipelines”, *30th Anniversary Symposium on Underwater Technology*, TNO-IWECO, Kurhaus, The Hague, The Netherlands.

Levyakov, S.V., 2001. “Equations of finite bending of thin-walled curvilinear tubes”, J. Appl. Mech. Tech. Phys. 52 (5) 898–901.

Mroz, Z., 1967. “On the description of anisotropic work hardening”, Journal of the Mechanics and Physics of Solids 15, 163-175.

Ohno, N., Wang, J.-D., 1993. “Kinematic hardening rules with critical state of dynamic recovery, part I: formulations and basic features for ratcheting behavior”, International Journal of plasticity 9, 375-390.

Pan, W.F., and Lee, K.L, 2002. “The Effect of Mean Curvature on the Response and Collapse of Thin-Walled Tubes under Cyclic Bending”. JSME International Journal, Series A, Vol. 45, No. 2.

Popov, E.P., Zayas, V.A., and Stephen, M.A., 1979. “Cyclic Inelastic Buckling of Thin Tubular Columns”. Journal of the Structural Division. ASCE

Prager, W., 1956. “A new method of analyzing stresses and strains in work hardening plastic solids”, Journal of Applied Mechanics 23, 493-496.

Reissner, E., Weinitschke, H.J., 1963. “Finite pure bending of circular cylindrical tubes”. Quarterly of Applied Mathematics XX (4),305–319.

Shaw, P.K., Kyriakides, S., 1985. “Inelastic analysis of thin-walled tubes under cyclic bending”. International Journal of Solids and Structures 21 (11), 1073–1100.

Slagis, G.C, 1997. “Evaluation of Seismic Response Data for Piping”. Welding Research Council, Bulettin 423.

Toma, S., Chen, W.F., 1983. “Cyclic inelastic analysis of tubular column sections”. *Computers & Structures*, *Volume 16, Issue 6*, *Pages 707-716*

Toscano, R.G., Raffo, J., Fritz, M., Silva, R.C., Hines, J., Timms, C., 2008. “Modeling the UOE Pipe Manufacturing Process”, *Proceedings of 27th International Conference on Offshore Mechanics and Arctic Engineering*, OMAE2008-57605, Estoril, Portugal

Tseng, N.T., Lee, G.C., 1983. Simple plasticity model of the two-surface type. ASCE Journal of Engineering Mechanics 109, 795-810.

Yeh, M.K. and Kyriakides, S., 1986. “On the collapse of inelastic thick-walled tubes under external pressure”, *Journal of Energy Resources Technology,* Transaction of the ASME*,* Vol. 108 (1), pp. 35-47. MAR

Ziegler, H., 1959. “A modification of Prager’s hardening rule”. Quart. Appl. Mech. 17. p.p. 55-65.